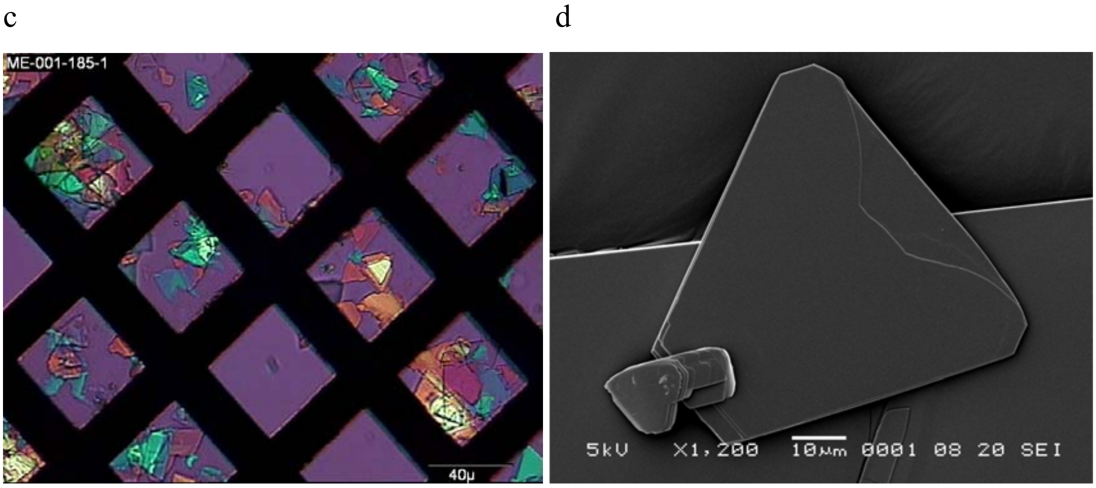

Figure 5.13 TEM analysis of Form II of theophylline. (a) TEM image of overlapping triangular crystals of Form II of theophylline. The dark lines running across the crystals are bend contours. (b) Selected area electron diffraction pattern from the region circled in image 1a. (c) Polarized light microscopy image of theophylline crystals prepared on a copper TEM grid. (d) Scanning electron microscopy image of triangular theophylline crystals.

PLM and SEM images of the same sample of theophylline are shown for comparative purposes in Figure 5.13c and d. The triangular morphology of the theophylline crystals is discernible in the PLM image, but there is little detail, highlighting the advantages in magnification and resolution that TEM has over optical microscopy. The complementary nature of SEM and TEM images is apparent. Surface features of the theophylline crystals can be seen by SEM, whereas the TEM image displays the entire volume of the crystals. There is no indication from the SEM image that the crystals contain defects, and this is a clear advantage of TEM over SEM, as is the ability to obtain structural or compositional information using electron diffraction.

5.3.4 Extracting Information from Electron Diffraction Patterns

When interpreting electron diffraction patterns, the aim was to relate the reflections in the pattern to the crystal planes that gave rise to them. This process is called indexing.

An example of the indexing process is given here for diffraction patterns from a sample of Form I of amitriptyline hydrochloride, an antidepressant.

The distance of each reflection from the central (undiffracted) spot is inversely proportional to the interplanar spacing (d-spacing) of the corresponding crystal planes. The d-spacings were calculated using Equation 5.1, where λ is the wavelength of electrons, L is the camera length (a value which can be changed by altering the strength of lenses in the TEM instrument) and r is the distance on the diffraction pattern between the reflection and the central spot.

$$\mathbf{d = \lambda L/r} \qquad \text{(Equation 5.1)}$$

The d-spacing for the reflection could then be compared with the interplanar spacings of every different set of planes in the crystal structure appropriate to the sample, which were calculated with Equation 5.2 (using the unit cell parameters of the appropriate crystal structure). This is the most general formula for calculating d-spacings and can be applied to crystals of any lattice system, including triclinic.

$$\frac{1}{{d_{hkl}}^2} = \frac{1}{V^2}\begin{bmatrix} h^2b^2c^2\sin^2\alpha + k^2a^2c^2\sin^2\beta + l^2a^2b^2\sin^2\gamma + 2hkabc^2(\cos\alpha\cos\beta - \cos\gamma) \\ +2kla^2bc(\cos\beta\cos\gamma - \cos\alpha) + 2hlab^2c(\cos\alpha\cos\gamma - \cos\beta) \end{bmatrix}$$

(Equation 5.2)

It was not usually possible to unambiguously determine which crystal planes individual reflections, and single rows of reflections corresponded to as due the low symmetry of pharmaceutical crystals there were often several planes which had d-spacings that were within the error range of the observed value. It was found to be important to obtain zone axis diffraction patterns, where the electron beam is aligned with a crystallographic axis. These patterns have a regular array of reflections, one from each of the crystal planes perpendicular to the zone axis, allowing linked sets of interplanar spacings and interplanar angles to be measured. The difference between a diffraction pattern at a randomly selected orientation between crystal and electron beam, and one from a zone axis is shown in Figure 5.14.

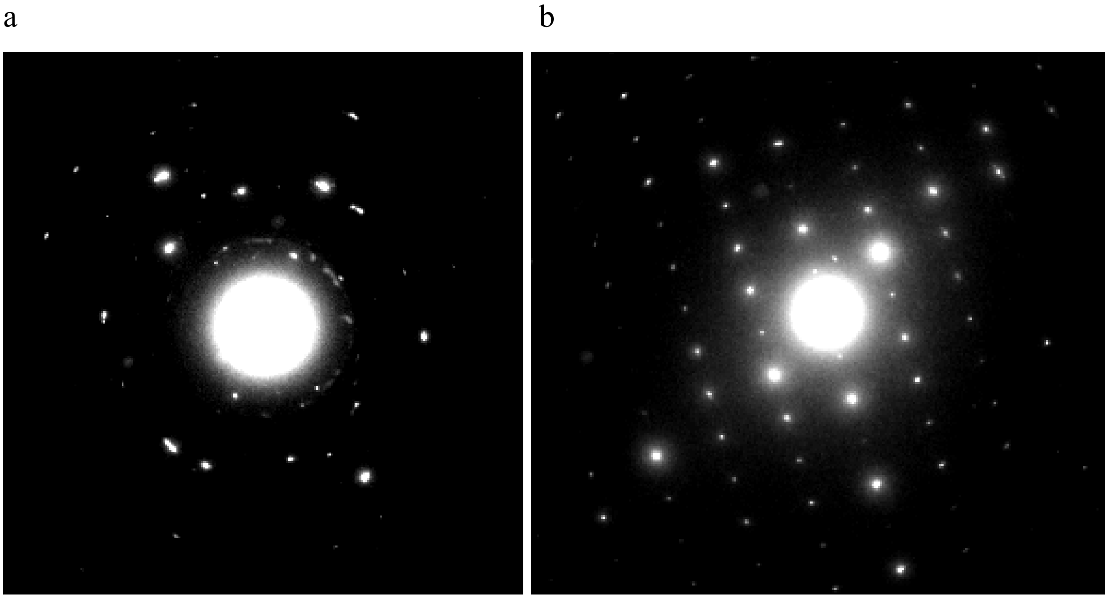

Figure 5.14 Electron diffraction patterns of amitriptyline hydrochloride. (a) Orientation selected at random. (b) Electron beam aligned with the <001> zone axis. This zone axis diffraction pattern has a repeating array of reflections.

When obtaining diffraction patterns from samples during TEM analysis, crystals were tilted with respect to the electron beam until a regular array of diffraction spots was observed, indicating that the electron beam was aligned with a zone axis. The imaging mode of TEM could be used to aid alignment of the electron beam with zone axes through identification of regions of crystals where bend contours cross (zone axis poles).

For indexing purposes, it was then necessary to determine to which zone axes these arrays corresponded. The patterns were reduced to two average d-spacings and an interplanar angle (as shown for an amitriptyline hydrochloride diffraction pattern in Figure 5.15a). These three values were compared with d-spacings and interplanar angles calculated for each of the crystal planes (with h, k and l Miller indices between –9 and 9) of the crystal structure appropriate to the sample (here amitriptyline hydrochloride Form 1, $a = 13.812$ Å, $b = 9.140$ Å, $c = 14.345$ Å, $\alpha = \gamma = 90$ °, $\beta = 96.82$ °).[10] The formula that was used for determining interplanar angles was Equation 5.3.[11]

For the amitriptyline hydrochloride diffraction pattern in Figure 5.15a, d_1, d_2 and θ were measured to be 13.98 Å, 9.02 Å and 89.9 ° respectively. The <001> zone axis was calculated to be a good match, with d_1 and d_2 corresponding to the (100) and (010) crystal planes, $d_{(100)} = 13.714$ Å, $d_{(010)} = 9.140$ Å and $\theta_{(100/010)} = 90.0$ °. Each reflection in the diffraction pattern could then be indexed (Figure 5.15b).

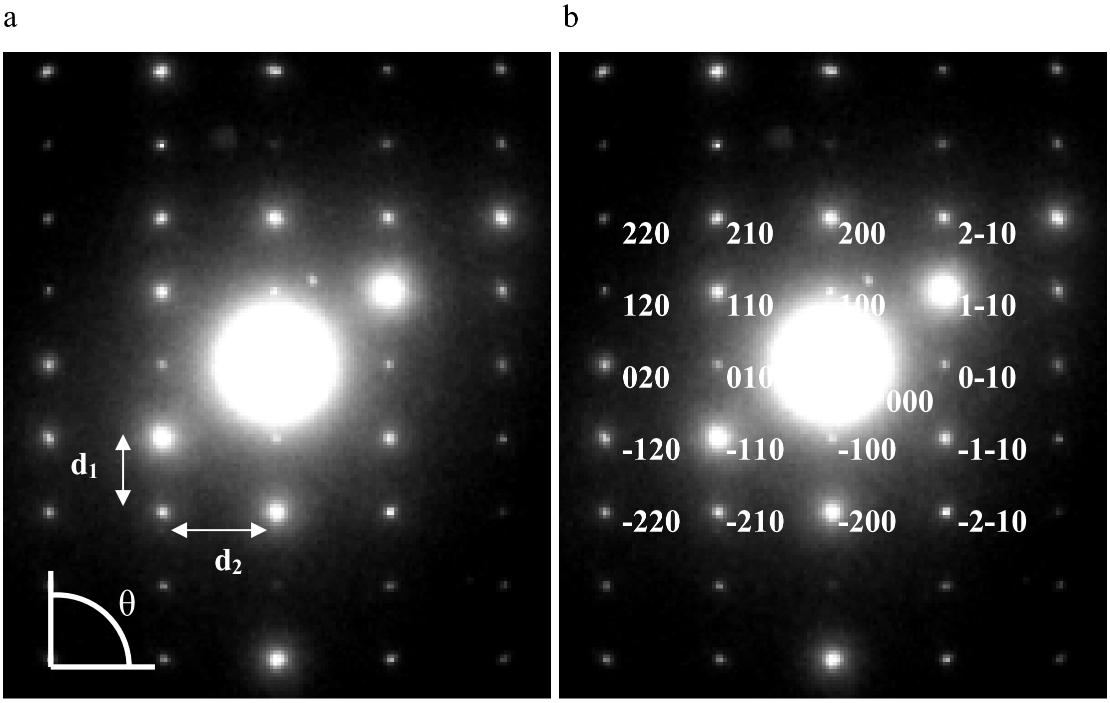

Figure 5.15 Indexing of a zone axis diffraction pattern of Form I of amitriptyline hydrochloride. (a) The pattern was reduced to two average d-spacings and an interplanar angle. (b) The zone axis was calculated to be <001>, allowing the individual reflections to be indexed.

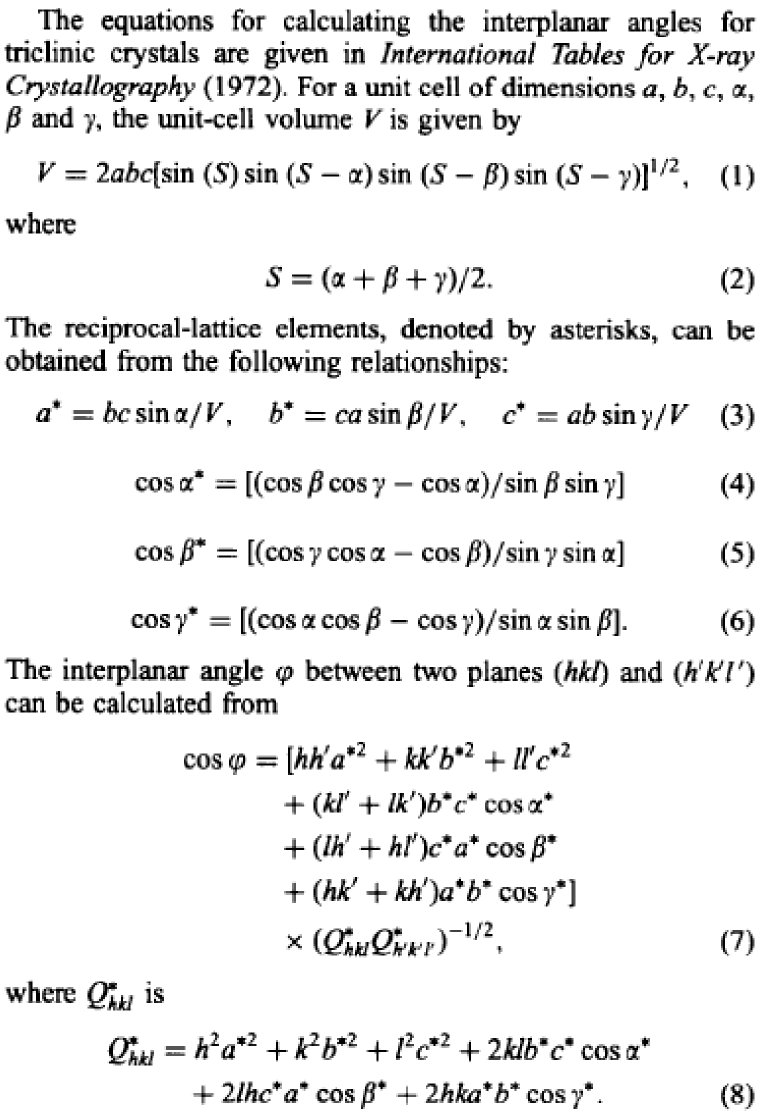

The equations for calculating the interplanar angles for triclinic crystals are given in *International Tables for X-ray Crystallography* (1972). For a unit cell of dimensions a, b, c, α, β and γ, the unit-cell volume V is given by

$$V = 2abc[\sin(S)\sin(S-\alpha)\sin(S-\beta)\sin(S-\gamma)]^{1/2}, \quad (1)$$

where

$$S = (\alpha+\beta+\gamma)/2. \quad (2)$$

The reciprocal-lattice elements, denoted by asterisks, can be obtained from the following relationships:

$$a^* = bc\sin\alpha/V, \quad b^* = ca\sin\beta/V, \quad c^* = ab\sin\gamma/V \quad (3)$$

$$\cos\alpha^* = [(\cos\beta\cos\gamma - \cos\alpha)/\sin\beta\sin\gamma] \quad (4)$$

$$\cos\beta^* = [(\cos\gamma\cos\alpha - \cos\beta)/\sin\gamma\sin\alpha] \quad (5)$$

$$\cos\gamma^* = [(\cos\alpha\cos\beta - \cos\gamma)/\sin\alpha\sin\beta]. \quad (6)$$

The interplanar angle φ between two planes (hkl) and ($h'k'l'$) can be calculated from

$$\begin{aligned}\cos\varphi = {} & [hh'a^{*2} + kk'b^{*2} + ll'c^{*2} \\ & + (kl' + lk')b^*c^*\cos\alpha^* \\ & + (lh' + hl')c^*a^*\cos\beta^* \\ & + (hk' + kh')a^*b^*\cos\gamma^*] \\ & \times (Q^*_{hkl}Q^*_{h'k'l'})^{-1/2}, \end{aligned} \quad (7)$$

where Q^*_{hkl} is

$$\begin{aligned}Q^*_{hkl} = {} & h^2a^{*2} + k^2b^{*2} + l^2c^{*2} + 2klb^*c^*\cos\alpha^* \\ & + 2lhc^*a^*\cos\beta^* + 2hka^*b^*\cos\gamma^*. \end{aligned} \quad (8)$$

(Equation 5.3) – Taken from Tam et al, 1995.[11]

Finally, the experimental diffraction pattern was compared with a simulated diffraction pattern of the matching zone axis to ensure that systematic absences and reflection intensities corresponded, and as a final confirmation that the indexing was correct (Figure 5.16).

A visual basic for applications (VBA) script was written to perform the indexing procedure computationally (with a third measured average d-spacing used in the calculation to reduce the chance of coincidental matches). The script outputs a list of zone axes where the difference between observed and theoretical values is below a selected threshold.

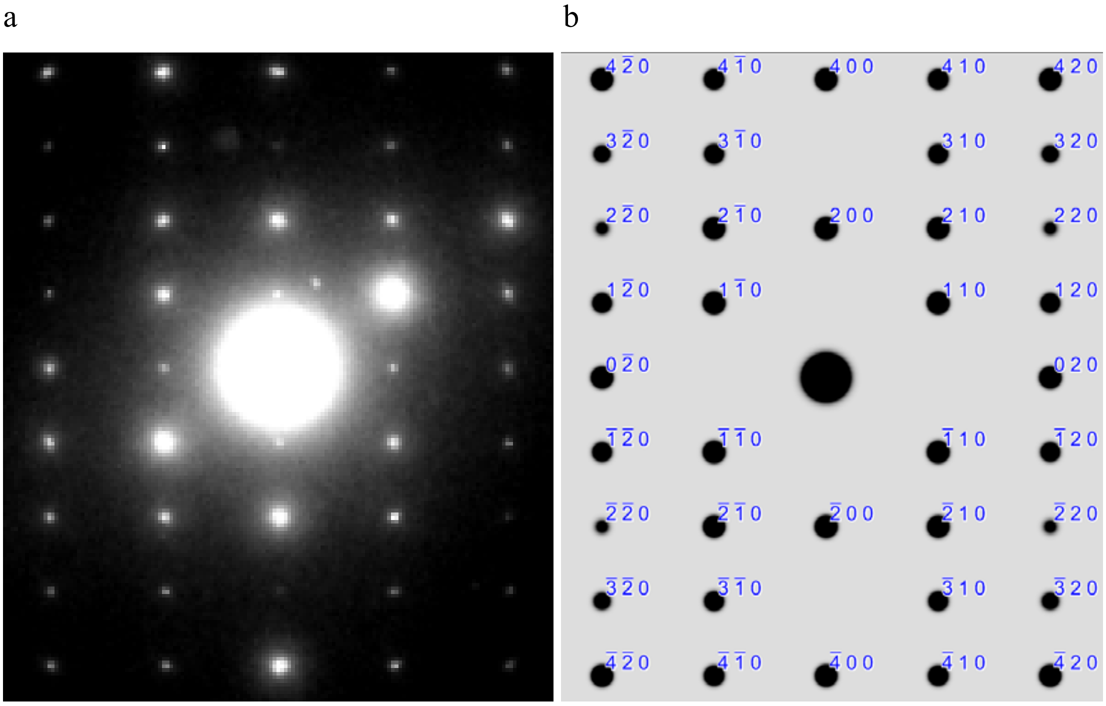

Figure 5.16 Comparison of (a) experimental and (b) simulated electron diffraction patterns of the <001> zone axis of amitriptyline hydrochloride. The simulated pattern was generated from CSD crystal structure YOVZEO.[10]

As every different crystal structure has its own unique set of zone axis diffraction patterns, zone axis electron diffraction patterns can be used as a way of identifying the crystal form of the sample being analysed. Indexing the experimental electron diffraction pattern of amitriptyline hydrochloride above not only demonstrated that the electron beam was aligned with the <001> zone axis of a crystal when the pattern was recorded, but also, and perhaps more importantly, confirmed that the crystal being analysed was of Form I of amitriptyline hydrochloride.

When analysing a sample of a crystal form for which there was no reported crystal structure it was not possible to index diffraction patterns in the same manner. In these cases, reflections from electron diffraction patterns were plotted on a 2θ scale and compared with the XRPD trace of the crystal form (an example is given in Section 6.2.4, Figure 6.10). The use of TEM for crystal phase identification is explored further in Chapter 6.

5.3.5 Multiple Scattering in Electron Diffraction Patterns

Certain symmetry elements in crystal structures, such as screw axes and glide planes, cause the reflections from some sets of crystal planes to be absent from diffraction patterns. These are called systematic absences.

In the <100> zone axis diffraction pattern of nifedipine the odd 0k0 and 00l reflections are expected to be absent. This can be seen in the simulated electron diffraction pattern shown in Figure 5.17a. However, these reflections are clearly present in the experimental electron diffraction pattern of the same zone axis (Figure 5.17b).

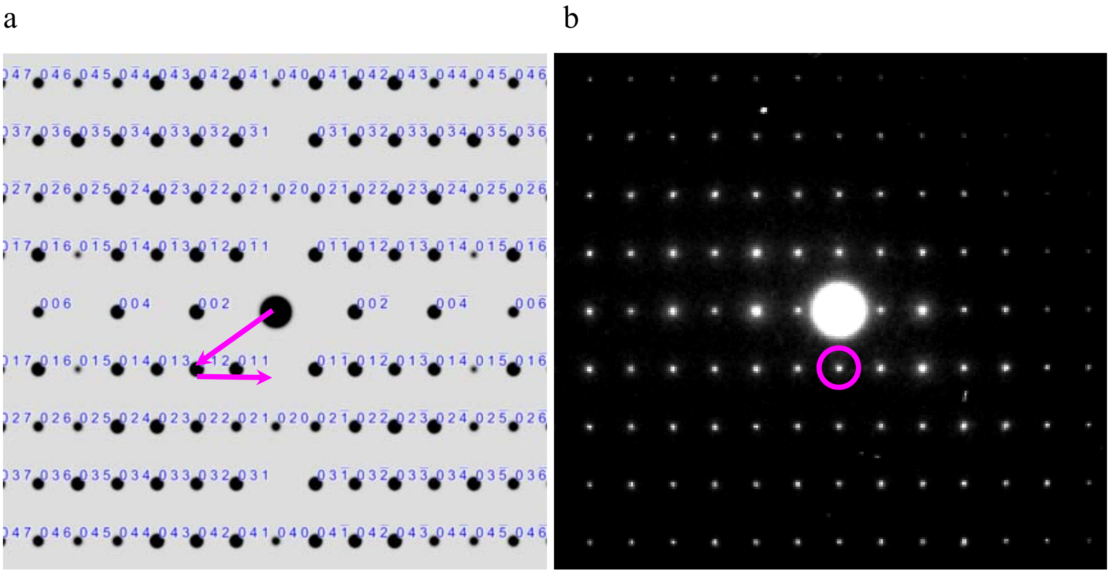

Figure 5.17 Multiple scattering in the <100> zone axis diffraction pattern of nifedipine. (a) Simulated electron diffraction pattern of the <100> zone axis of nifedipine based on a kinetic model with systematic absences allowed (CSD ref BICCIZ).[12] (b) Experimental electron diffraction pattern of the <100> zone axis of nifedipine. Reflections which should be systematic absences in the diffraction pattern are present due to multiple scattering. For example, a possible double diffraction event that would give a ‘010’ reflection is shown in magenta.

The simulated diffraction pattern is based on a kinematic model and assumes that electrons undergo only one scattering event as they pass through a crystal. The reason that the odd 0k0 and 00l reflections appear to be present in the experimental diffraction pattern is that multiple scattering has occurred (dynamical scattering). Electrons are often diffracted more than once as they pass through a sample as they interact strongly with the sample. The effect of these diffractions is additive, and may result in an electron being scattered at an angle that corresponds to one of the absences. An example of this is shown by the magenta arrows in Figure 5.17a. Diffraction by the (012) crystal planes in nifedipine followed by diffraction by the (00-2) planes gives an overall effect that is equivalent to diffraction by the (010) planes. Multiple scattering also has an effect on reflection intensities.

This phenomenon of multiple scattering was found to be an important consideration when analysing electron diffraction patterns of pharmaceutical materials. In contrast, multiple scattering is not observed with X-rays as they interact with samples far more weakly than electrons do.

5.3.6 Correlation between TEM Images and Diffraction Patterns

As shown above, it is possible to obtain images and diffraction patterns from the same region of sample during TEM analysis. There is often, however, a rotation between the two which must be measured so that the two types of information can be compared directly. This measurement was made by comparing images and diffraction patterns from molybdenum trioxide, crystals of which have a characteristic long edge which is parallel to the [001] crystallographic direction.[13,14]

Having performed this measurement, it was possible to correlate crystal morphology with crystal structure in pharmaceutical samples. For example, images and corresponding diffraction patterns of crystals of two samples of Form II of theophylline, prepared from nitromethane and methanol respectively, are shown in Figure 5.18. Crystallographic directions, taken from the diffraction patterns, were applied to the images. This analysis demonstrated that the relative growth rate of crystal faces in samples prepared from methanol was different to that observed in samples prepared from nitromethane. The lath shaped crystals from methanol are approximately rectangular with a length in the [010] direction and a width in the [001] direction. In contrast, the triangular crystals from nitromethane have grown more rapidly in the [001] direction than in the [010] direction. This difference in crystal growth behaviour could not have been detected by other methods with crystallites as small as those that were analysed in this study.

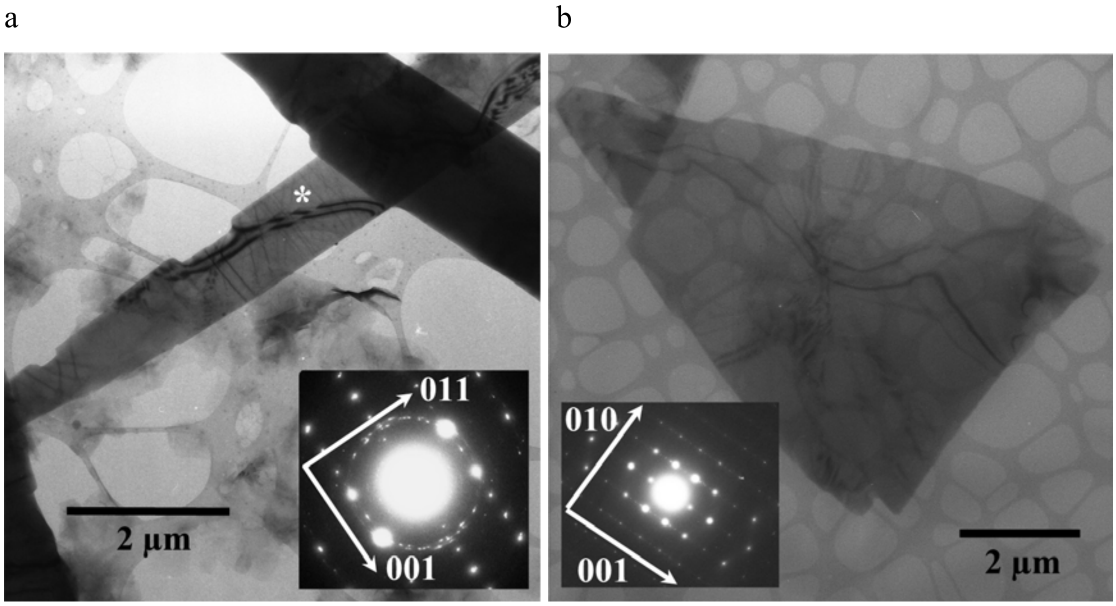

Figure 5.18 (a) TEM image showing a lath shaped crystal of theophylline Form II that was crystallized from methanol. The asterisk marks a region of the crystal where bend contours are distorted as they pass across defects running in the [010] direction. The corresponding <1-10> zone axis diffraction pattern is included as an inset. The ring of diffraction spots is due to reflections from small crystallites which grew on the amorphous carbon film support during sample preparation. (b) TEM image of a triangular crystal of theophylline prepared by cooling a saturated nitromethane solution. The corresponding <100> zone axis electron diffraction pattern of theophylline Form II is shown as an inset.

5.3.7 Dark Field Imaging

A dark field image is generated by tilting the incident electron beam so that after interacting with the sample one of the diffracted beams is directed straight down the instrument column. All other beams, including the main beam, are stopped by inserting an objective aperture. This configuration gives an image in which all regions of a sample are dark apart from those where Bragg diffraction to give the selected diffracted beam is occurring.

Dark field imaging is useful as it allows determination of the sets of crystal planes that are associated with each bend contour. The way that different bend contours interact with defects can then be used to identify the type of defect that is present.

An example of dark field imaging is given in Figure 5.19. The normal (bright field) TEM image of a plate-like crystal of theophylline shows many bend contours which cross in the circled region to form a bend contour pole (Figure 5.19a). A zone axis diffraction pattern was recorded from the circled region, and was indexed to the <100> zone axis of Form II of theophylline (Figure 5.19c). The dark field configuration was adjusted so that electrons diffracted by the (011) crystal planes were directed down the TEM column. The resulting dark field image shows regions of the crystal where Bragg scattering from the (011) crystal planes is occurring (Figure 5.19b). It is evident that this bend contour is disrupted by defects in the crystal, indicating that the (011) crystal planes are distorted by the defects.

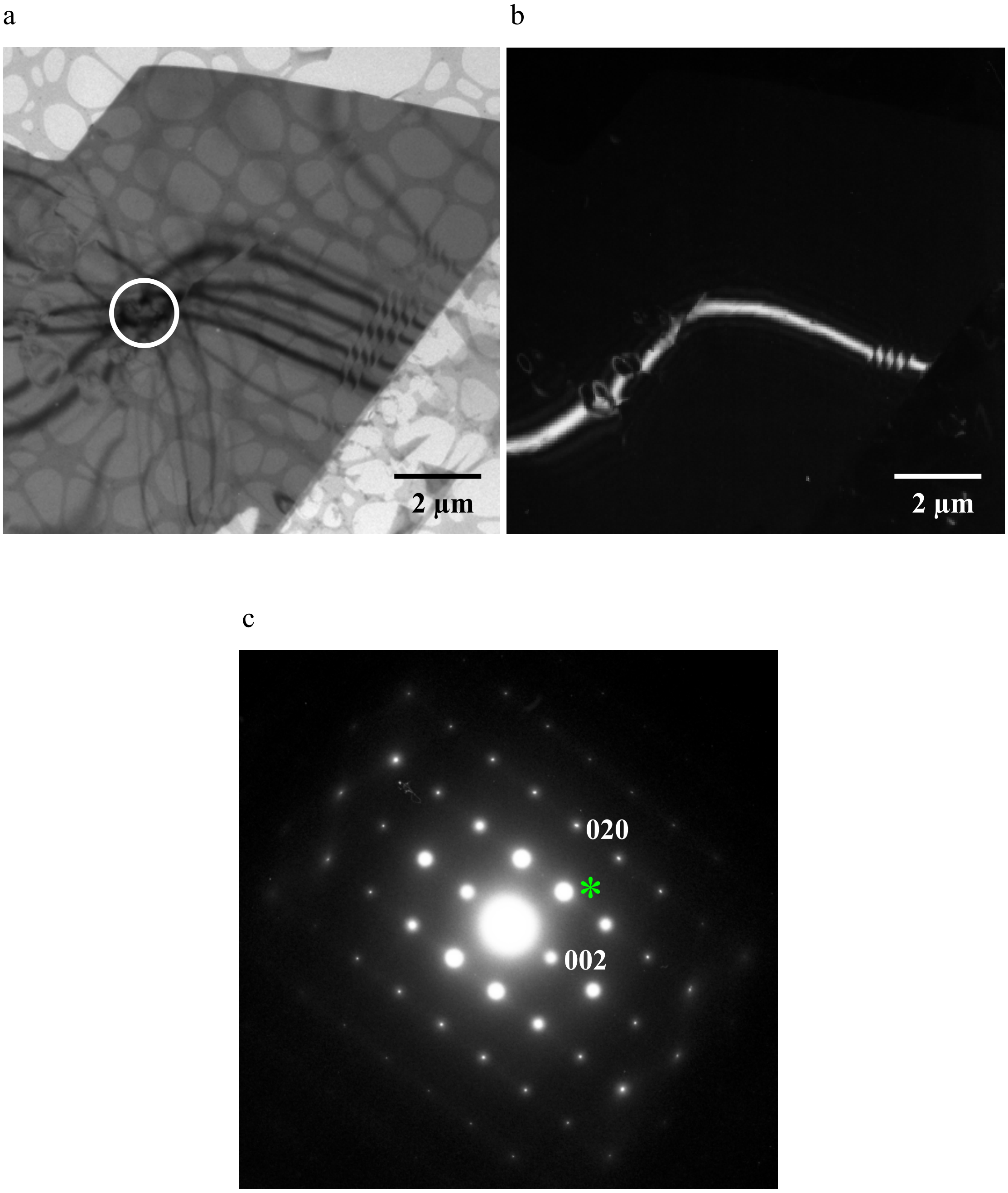

Figure 5.19 Dark field image analysis of a crystal of theophylline. (a) TEM (bright field) image. (b) Corresponding dark field image. (c) <100> zone axis electron diffraction pattern taken from the region circled in (a). The reflection marked with an asterisk (011) was used to generate the dark field image.

5.3.8 TEM Analysis with a High Resolution Instrument

A sample of Form II of theophylline was analysed using a high resolution JEOL 200CX TEM instrument. The beam lifetime of theophylline crystals in this instrument was less than one minute, over an order of magnitude shorter than in a CM30 instrument. The beam lifetime was shorter as it was not possible to spread the electron beam sufficiently to reduce beam flux to a level where severe localised sample heating in the beam was avoided. This heating caused rapid sample amorphisation.

Diffraction patterns and images were recorded using a CCD camera. While it was possible to obtain diffraction patterns, there was insufficient time to properly align them (Figure 5.20a). Bend contours and possible defects can be seen in the image recorded at 4000x magnification in Figure 5.20b, but the image quality is lower than that obtained with a CM30 instrument and photographic plates. High resolution images of theophylline were recorded, but there were no discernible fringes or features that would indicate a repeating array of molecules (Figure 5.20c). It is possible that focussing the images took longer than the beam lifetime of the crystals.

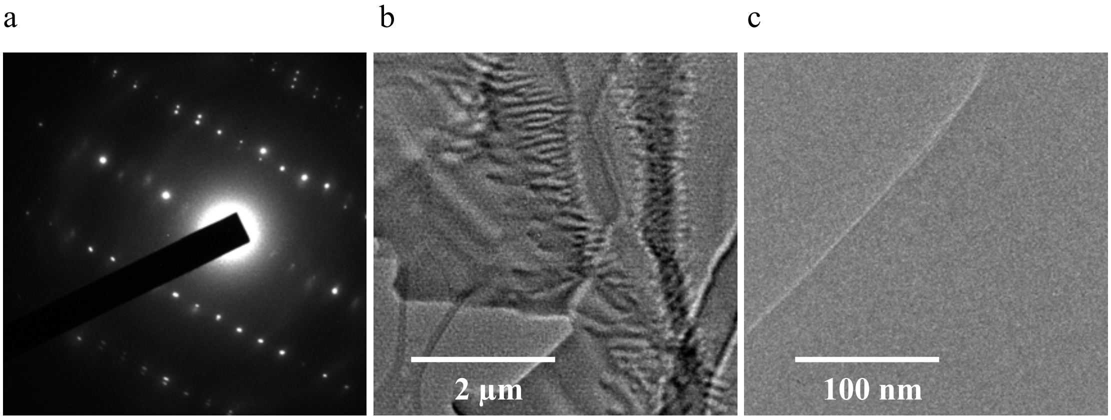

Figure 5.20 TEM analysis of Form II of theophylline using a JEOL CX200 instrument. (a) An electron diffraction pattern which is not properly aligned with a zone axis. (b) TEM image recorded at 4,000x magnification showing bend contours and possible defects. (c) TEM image recorded at 100,000x magnification. These images were recorded with Dr David Jefferson of the Department of Chemistry, University of Cambridge

5.4 Conclusions

It is clear that perceived problems with sample preparation and electron beam damage are not prohibitive to analysis of pharmaceuticals by TEM. The amount of information that was obtained about the samples that were analysed here was, however, found to be dependant on specimen morphology, with large, thin plates proving ideal. It was possible to obtain diffraction patterns for all compounds that were analysed by TEM before severe beam damage occurred, allowing the crystal phase to be identified. Furthermore, the described mapping of crystal habit to crystal structure for samples of theophylline, could not have been achieved with any other analytical technique currently used in pharmaceutical analysis.

Though TEM is not as straightforward a technique as some widely used methods such as XRPD and DSC, a different range of information can be obtained about pharmaceutical samples using this technique, demonstrating that TEM has a place in pharmaceutical analysis.

Initial attempts at high resolution TEM analysis were unsuccessful. High magnifications require high beam fluxes in order to give suitable sample illumination, and this causes rapid sample degradation. This work also showed that some TEM instruments are more suitable for pharmaceutical analysis than others as it is important to be able to spread the electron beam to reduce beam flux.

5.5 Further Work

There are existing methods for improving electron beam stability that could increase beam lifetimes even further than with the procedures described in this Chapter. For example, the use of a liquid helium cooled specimen stage could be explored. Also, samples, or the lacy carbon sample supports on which they rest, could be sputter coated with platinum in order to aid the dissipation of heat and charge during analysis. The platinum may, however, interfere with images or diffraction patterns, and this would need to be investigated.

5.6 References

1. Jones W., Thomas J. M. Applications of electron microscopy to organic solid-state chemistry. *Prog. Solid State Chem.*, 1979, 12(2), 101-124.

2. Thomas J. M., Williams J. O. Dislocations and the reactivity of organic solids. *Prog. Solid State Chem.*, 1971, 6, 119-154.

3. Reynolds P. A. Martensitic phase transitions in molecular crystals - p-dichlorobenzene. *Acta Crystallogr., Sect. A*, 1977, A33(1), 185-191.

4. Young R. J., Read R. T., Petermann J. Defects in polydiacetylene single crystals. Part 1. The perfect crystal and stacking faults. *J. Mater. Sci.*, 1981, 16(7), 1835-1842.

5. Kolb U., Gorelik T. E., Mugnaioli E., Stewart A. Structural Characterization of Organics Using Manual and Automated Electron Diffraction. *Polym. Rev.*, 2010, 50(3), 385-409.

6. Jones W., Thomas J. M., Williams J. O., Hobbs L. W. Electron microscopic studies of extended defects in organic molecular crystals. I. p-Terphenyl. *J. Chem. Soc., Faraday Trans. 2*, 1975, 71(1), 138-145.

7. Ohno T., Sengoku M., Arii T. Measurements of electron beam damage for organic crystals in a high voltage electron microscope with image plates. *Micron*, 2002, 33(4), 403-406.

8. Champness P. E. Transmission electron microscopy in earth science. *Annu. Rev. Earth Planet. Sci.*, 1977, 5, 203-226.

9. 2007. Gatan website. http://www.gatan.com/resources/knowhow/kh19_eels.php.

10. Klein C. L., Lear J., O'Rourke S., Williams S., Liang L. Crystal and molecular structures of tricyclic neuroleptics. *J Pharm Sci*, 1994, 83(9), 1253-1256.

11. Tam K. Y., Compton R. G. GAMATCH - a genetic algorithm-based program for indexing crystal faces. *J. Appl. Crystallogr.*, 1995, 28(5), 640-645.

12. Triggle A. M., Shefter E., Triggle D. J. Crystal structures of calcium channel antagonists: 2,6-dimethyl-3,5-dicarbomethoxy-4-[2-nitro-, 3-cyano-, 4-(dimethylamino)-, and 2,3,4,5,6-pentafluorophenyl]-1,4-dihydropyridine. *J. Med. Chem.*, 1980, 23(12), 1442-1445.

13. Williams D. B., Carter C. B. Transmission electron microscopy. A textbook for materials science. New York: Plenum Press, 1996.

14. Volta J. C., Forissier M., Theobald F., To Phong P. Dependence of selectivity on surface structure of molybdenum trioxide catalysts. *Faraday Discuss. Chem. Soc.*, 1981, 72, 225-233.

6 Crystal Form Identification by TEM

6.1 Introduction

As outlined in Chapter 1, finding all of the possible forms of an API, and understanding their behaviour, is a critical part of the drug development process. This Chapter describes an investigation into use of the diffraction capacity of an electron microscope for identifying the crystal form of pharmaceutical materials.

The approach to structure identification using the reflections in an electron diffraction pattern that was described in Section 5.3.4 was applied to the identification of the crystal phase of a variety of different pharmaceutical samples (including different polymorphs, salts, cocrystals and samples containing a mixture of phases) to test the robustness of the method and its general applicability.

The following examples demonstrate not only that electron diffraction could be used to routinely identify the crystal form of samples, but also that it could be applied in situations where phase identification with other analytical techniques was not possible, or gave ambiguous results.

6.2 Results and Discussion

6.2.1 Identifying Crystal Forms from their Electron Diffraction Patterns

Initial experiments investigated the ability to distinguish different polymorphs of paracetamol by TEM. There are three reported polymorphs of paracetamol.[1,2] Samples of Form I and Form II were generated (the identity of the crystal form being examined was determined by XRPD analysis and comparison with reference patterns for these forms (Form I – HXACAN01, Form II – HXACAN08)), but Form III has been shown to be highly unstable under ambient conditions, converting to Form II within an hour,[2] and so was not considered in the investigation.

The sample of Form I of paracetamol was prepared by rapidly cooling a saturated solution of paracetamol in methanol in a sealed vial. Crystals were isolated by filtration, then dried, and transferred to a TEM sample grid. An electron diffraction pattern from one of the resulting crystals is shown in Figure 6.1a. Values d_1, d_2, d_3, θ_1, θ_2 and θ_3 were measured to be 5.31 Å, 4.38 Å, 2.90 Å, 67.1 °, 37.5 ° and 29.4 ° respectively (Figure 6.1c). The procedure described in Section 5.3.4 was then used to find any zone axes of paracetamol Form I and paracetamol Form II that matched these values. The unit cell parameters for paracetamol Form I and Form II that were used to calculate d-spacings and interplanar angles were obtained from CSD structures HXACAN01 and HXACAN08 respectively.[1,3]

Only one zone axis of paracetamol Form I, the <-2-11> zone axis, was found to be consistent with the experimental diffraction pattern (using the set of crystal planes with h, k and l Miller indices between –9 and 9, and tolerances of d +/- 4 %, θ +/- 3 °). The calculated d-spacings and interplanar angles for this zone axis are $d_{(011)}$ = 5.283 Å, $d_{(-120)}$ = 4.358 Å, $d_{(-131)}$ = 2.863 Å, $\theta_{(011/-120)}$ = 67.3 °, $\theta_{(011/-13`)}$ = 37.3 ° and $\theta_{(-120/-131)}$ = 30.0 °. A simulated electron diffraction pattern of this zone axis was generated, and was found to match well with the experimental pattern (Figure 6.1b).

In addition, the <111> zone axis of paracetamol Form II had d-spacings and interplanar angles that were consistent with values calculated for the diffraction pattern (using the same tolerances). However, when the simulated diffraction pattern of this zone axis was compared with the experimental pattern (Figure 6.1d) it was clear that the two patterns did not match. Though there are some reflections in the simulated pattern that correspond to the positions of reflections in the experimental pattern (such as the 20-2 reflection which has been marked '20-2' in the experimental pattern), there are also several reflections that are not present in the experimental pattern. For example, the 11-2 and 12-3 reflections in the simulated pattern are not observed experimentally, indicating that the <111> zone axis of paracetamol Form II is not a match for the observed diffraction pattern.

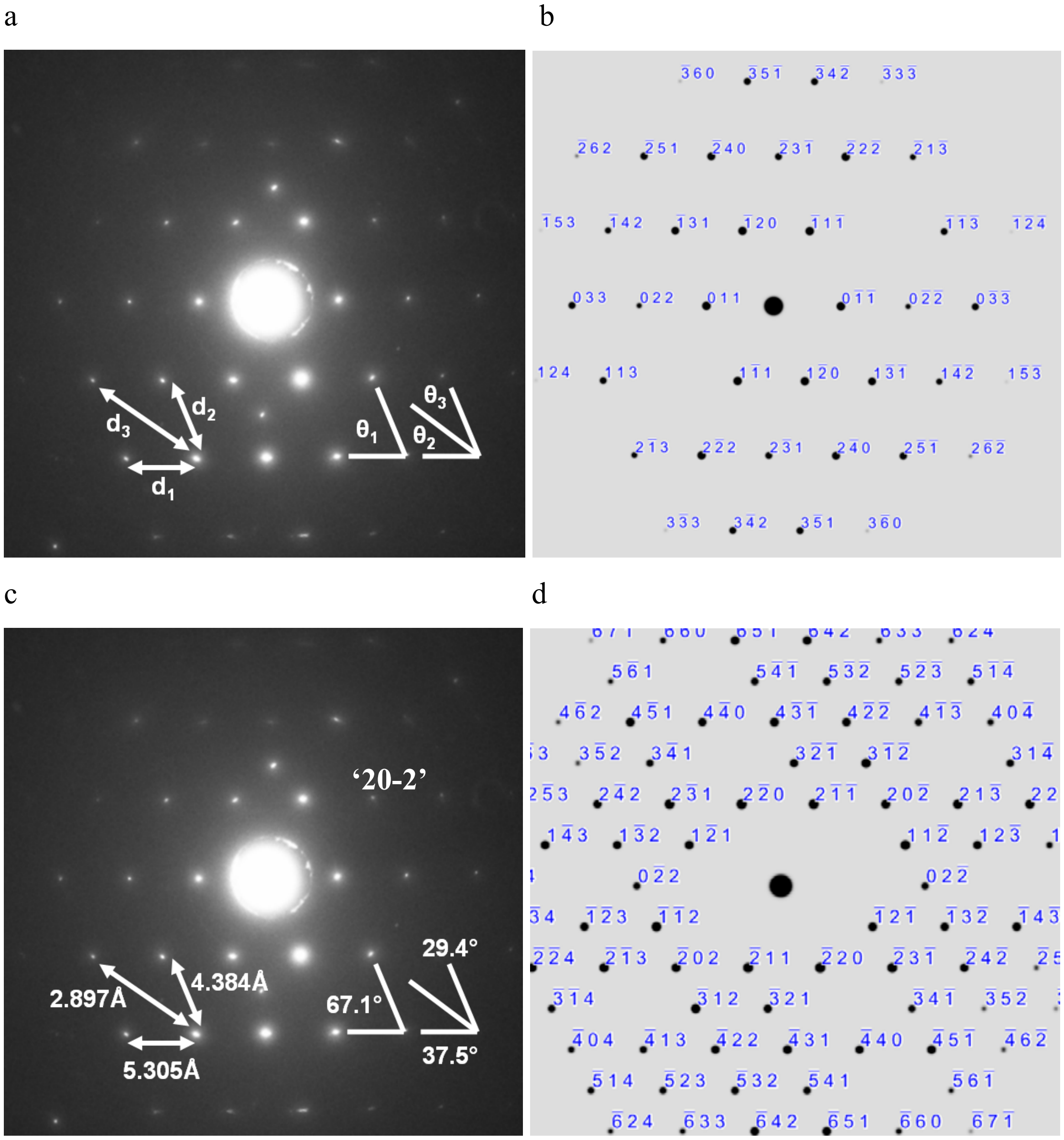

Figure 6.1 Indexing a zone axis electron diffraction pattern from a sample of paracetamol Form I. (a) Experimental zone axis electron diffraction pattern from a sample of paracetamol Form I. (b) Simulated electron diffraction pattern of the <-2-11> zone axis of paracetamol Form I (from CSD structure HXACAN01).[1] (c) Measured d-spacings and angles for the experimental electron diffraction pattern. (d) Simulated electron diffraction pattern of the <111> zone axis of paracetamol Form II (from CSD structure HXACAN08).[3]

These results demonstrated unambiguously that the crystal from which the diffraction pattern in Figure 6.1a was obtained was Form I of paracetamol (in agreement with the XRPD analysis of this sample). Electron diffraction patterns from several other crystals were obtained and indexed to confirm that the bulk of the sample was also Form I.

A sample of Form II of paracetamol was prepared by heating amorphous paracetamol to 125 °C in a DSC pan (the amorphous phase was generated by melting paracetamol at 190 °C and then quench cooling). After cooling to room temperature, the resulting crystals were transferred to a TEM sample grid. A TEM image of the sample is shown in Figure 6.2, along with a corresponding electron diffraction pattern.

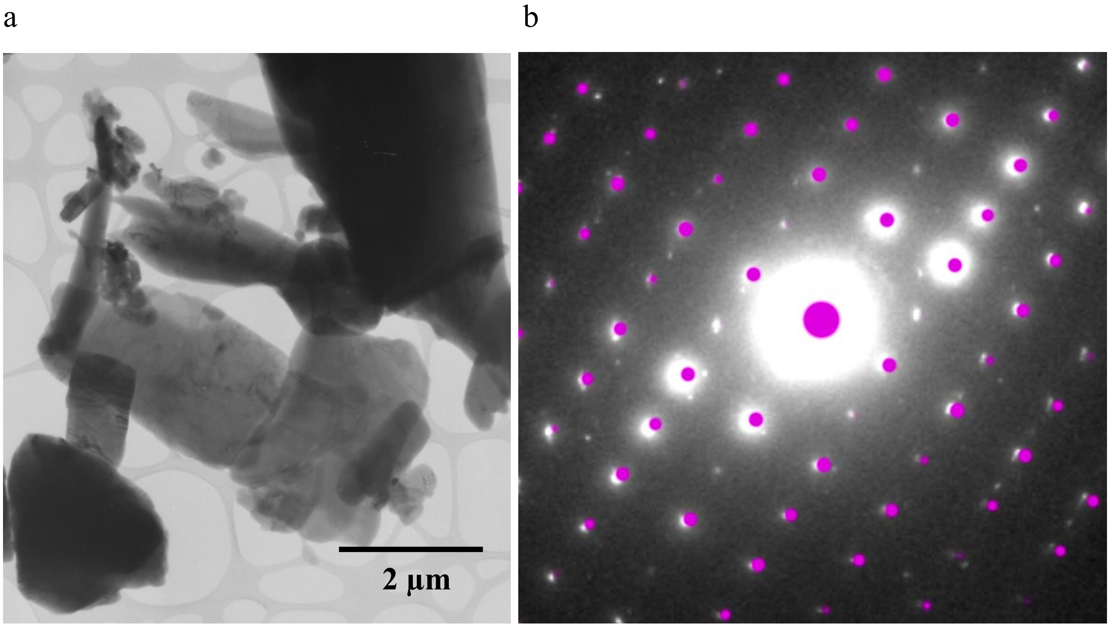

Figure 6.2 TEM analysis of a sample of paracetamol Form II. (a) TEM image of crystals of Form II of paracetamol. (b) A corresponding zone axis electron diffraction pattern from the sample. The simulated electron diffraction pattern of the <001> zone axis of paracetamol Form II is overlaid in magenta (from CSD structure HXACAN08).[3]

The diffraction pattern was indexed against Forms I and II of paracetamol and the only match was the <001> zone axis of Form II of paracetamol. A simulated diffraction pattern of this zone axis was generated. This pattern is overlaid in magenta on the experimental diffraction pattern in Figure 6.2b, with the good match demonstrating that the correct zone axis has been identified. This result showed unambiguously that the crystal from which the diffraction pattern in Figure 6.2b was obtained was Form II of paracetamol, in agreement with XRPD analysis.

A further sample of paracetamol was prepared by melting Form I of paracetamol at 200 °C, spreading a small amount of the resulting liquid phase thinly over a TEM sample support grid, and allowing it to cool and crystallise. All three of the known polymorphic forms of paracetamol have previously been crystallised from the melt,[2] and so it was not known, prior to TEM analysis, which form was present. In addition, the amount of sample on the TEM grid (<< 1 mg) was not sufficient for analysis by XRPD. TEM analysis of the sample is shown in Figure 6.3. From the TEM image it can be seen that paracetamol has crystallised as a thin film comprised of numerous different crystalline domains. The corresponding electron diffraction pattern could be indexed unambiguously to the <010> zone axis of Form I of paracetamol (repeated attempts to index as Form II and Form III were unsuccessful). Diffraction patterns from several other crystals were also indexed to Form I of paracetamol demonstrating that the bulk of the sample was Form I.

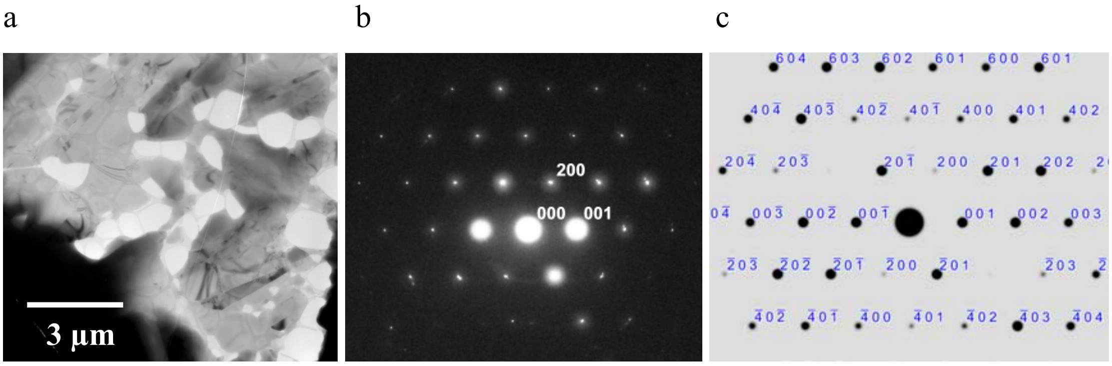

Figure 6.3 (a) TEM image of a sample of paracetamol prepared by crystallisation from the melt. (b) Experimental electron diffraction pattern from a region of the same sample (<010> zone axis of paracetamol Form I). (c) Simulated electron diffraction pattern of the <010> zone axis of paracetamol Form I (from CSD structure HXACAN01).[1] The evident differences between the reflection intensities in the experimental and simulated patterns (especially reflections 20-2 and –202) are due to the contribution of multiple scattering to the experimental pattern.

This work with paracetamol demonstrated that TEM could be used to identify different polymorphic forms, even under conditions where XRPD analysis was not possible because of the limited amount of material available.

Crystal phase identification was also possible with salts and cocrystals. The use of the diffraction pattern indexing method for the identification of the crystalline phase present in samples of a pharmaceutical salt (ranitidine hydrochloride) and of a cocrystal (2:1 caffeine:oxalic acid) is shown in Figure 6.4. Both specimens were prepared by careful crushing of large crystals (as received from supplier) between two glass slides. The ranitidine hydrochloride diffraction pattern was indexed against the Form II unit cell reported by Mirmehrabi et al (CSD ref TADZAZ03, $P2_1/n$, a = 7.208 Å, b = 12.979 Å, c = 18.807 Å, β = 95.06°)[4] and corresponds to a view down the <10-1> axis of the crystal. This diffraction pattern did not match any zone axis of Form I of ranitidine hydrochloride, or of Forms I and II of ranitidine free base. The diffraction pattern of the 2:1 cocrystal of caffeine and oxalic acid was indexed against the unit cell reported by Trask et al (CSD ref GANXUP, $P2_1/c$, a = 4.41430 Å, b = 14.7701 Å, c = 15.9119 Å, β = 96.4850°)[5] and corresponds to a view down the <110> axis of the crystal. This diffraction pattern did not match any zone axis of Forms I and II of caffeine, or of the alpha and beta polymorphs of oxalic acid.

6.2.2 Difficulties Associated with Phase Identification from Electron Diffraction Patterns

It was found that, while it was possible to determine the crystal phase of almost all of the samples that were analysed by TEM, this process was only possible if suitable electron diffraction patterns were obtained. Not all of the zone axis diffraction patterns that were recorded during this investigation could be indexed. For example, if there were just a few reflections in a diffraction pattern, the systematic errors associated with measuring average d-spacings and interplanar angles were large, making unambiguous indexing difficult.

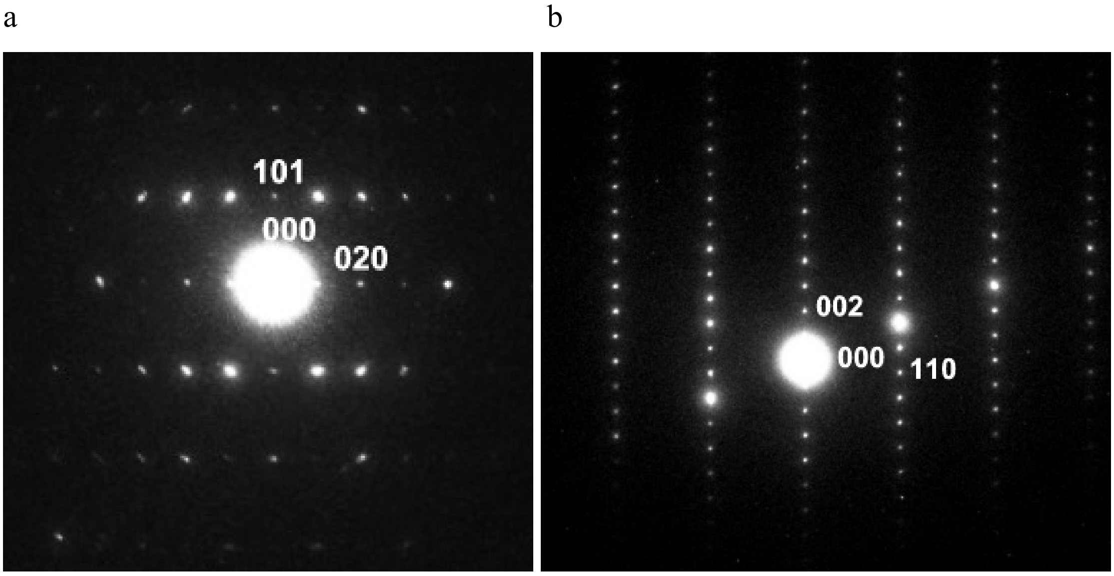

Figure 6.4 Electron diffraction patterns from a salt and a cocrystal which enabled the identity of the phases being analysed to be determined. (a) <10-1> zone axis electron diffraction pattern of Form II of ranitidine hydrochloride. (b) <110> zone axis electron diffraction pattern of a 2:1 caffeine:oxalic acid cocrystal (sample supplied by Andrew Cassidy of the Department of Chemistry, University of Cambridge).

This is illustrated by the diffraction pattern from a sample of caffeine in Figure 6.5a. The best match for this pattern is the <-111> zone axis of Form I of caffeine, but this indexing is not conclusive. Indexing was also difficult where diffraction patterns contained reflections from multiple crystals or crystalline domains. This is exemplified by the diffraction pattern from a sample of cholesterol in Figure 6.5b. There appear to be repeating patterns of reflections in this image, but obtaining a consistent set of d-spacings and angles is extremely difficult. Another hindrance to indexing was excessive streaking in diffraction patterns. Streaking due to stacking faults was observed in diffraction patterns of a 2:1 5-fluorouracil:phenazine cocrystal (Figure 6.5c). See also Chapter 9.

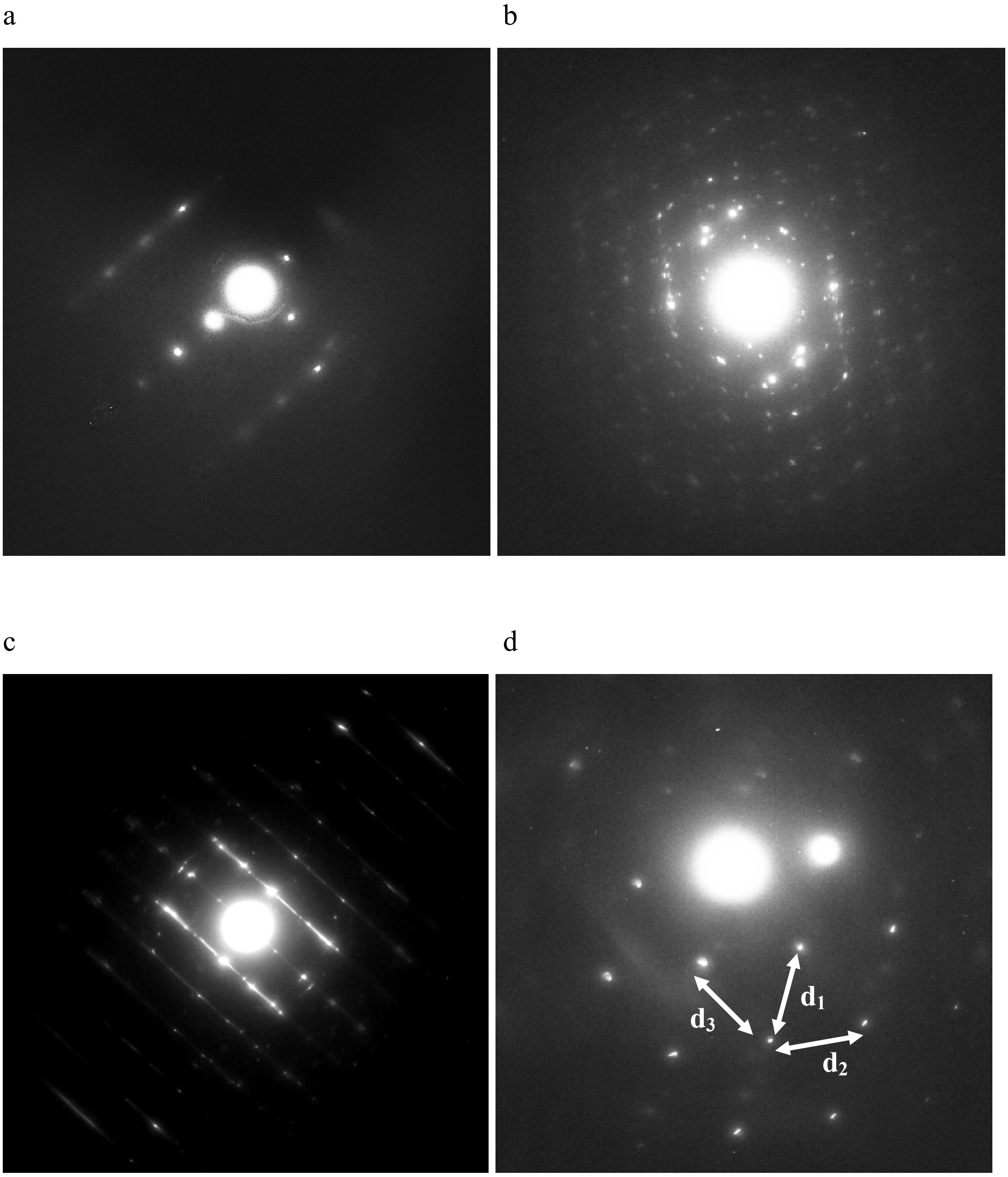

Figure 6.5 Examples of zone axis electron diffraction patterns where indexing was inconclusive or impossible. (a) A diffraction pattern, probably of the <-111> zone axis, of Form I of caffeine containing just a few reflections. (b) A diffraction pattern from a sample of cholesterol showing reflections from many overlapping crystallites. (c) A diffraction pattern from a 2:1 5-fluorouracil:phenazine cocrystal with streaking due to stacking faults. (d) A diffraction pattern of paracetamol that could not be indexed unambiguously as it was from a high index zone axis.

For some diffraction patterns there were several possible zone axis matches, making an unambiguous determination of the zone axis difficult, or impossible. This situation was common with diffraction patterns from high index zone axes, where the d-spacings of the planes giving rise to the reflections were small (< 3 Å). The crystal planes with the largest interplanar spacings in Forms I and II of paracetamol are listed in Table 6.1. It is evident that the first few d-spacings in the two lists differ significantly, and are characteristic of the two forms. As the d-spacing decreases, there are increasingly more crystal planes with similar values. Below 4 Å there is a lot of similarity in the d-spacings of crystal planes of Form I and Form II. For example, it was found that there were several zone axis patterns of paracetamol Form I and Form II that could be fitted to the diffraction pattern obtained from a sample of paracetamol that is shown in Figure 6.5d. The d-spacings calculated from this pattern were d_1 = 3.13 Å, d_2 = 3.06 Å and d_3 = 2.91 Å.

This observation showed that it was important to obtain characteristic diffraction patterns, with reflections from crystal planes with large d-spacings, when performing crystal phase identification by TEM. In practise, crystals were tilted with respect to the electron beam until zone axis diffraction patterns with small spot spacings were obtained. It was also clear that if several zone axis patterns were obtained from a crystal, and each could be indexed to a zone axis from the same crystal form, there was a greater confidence that the right form had been identified.

Table 6.1 The crystal planes with the largest d-spacings in (a) Form I and (b) Form II of paracetamol (crystal planes related by symmetry to those listed have been omitted).

a

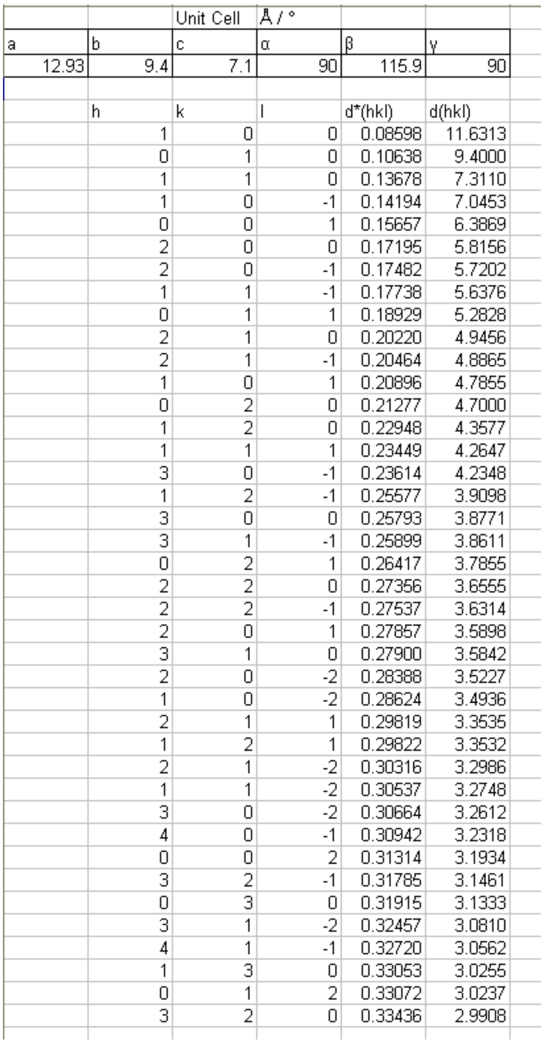

		Unit Cell	Å / °		
a	b	c	α	β	γ
12.93	9.4	7.1	90	115.9	90
	h	k	l	d*(hkl)	d(hkl)
	1	0	0	0.08598	11.6313
	0	1	0	0.10638	9.4000
	1	1	0	0.13678	7.3110
	1	0	-1	0.14194	7.0453
	0	0	1	0.15657	6.3869
	2	0	0	0.17195	5.8156
	2	0	-1	0.17482	5.7202
	1	1	-1	0.17738	5.6376
	0	1	1	0.18929	5.2828
	2	1	0	0.20220	4.9456
	2	1	-1	0.20464	4.8865
	1	0	1	0.20896	4.7855
	0	2	0	0.21277	4.7000
	1	2	0	0.22948	4.3577
	1	1	1	0.23449	4.2647
	3	0	-1	0.23614	4.2348
	1	2	-1	0.25577	3.9098
	3	0	0	0.25793	3.8771
	3	1	-1	0.25899	3.8611
	0	2	1	0.26417	3.7855
	2	2	0	0.27356	3.6555
	2	2	-1	0.27537	3.6314
	2	0	1	0.27857	3.5898
	3	1	0	0.27900	3.5842
	2	0	-2	0.28388	3.5227
	1	0	-2	0.28624	3.4936
	2	1	1	0.29819	3.3535
	1	2	1	0.29822	3.3532
	2	1	-2	0.30316	3.2986
	1	1	-2	0.30537	3.2748
	3	0	-2	0.30664	3.2612
	4	0	-1	0.30942	3.2318
	0	0	2	0.31314	3.1934
	3	2	-1	0.31785	3.1461
	0	3	0	0.31915	3.1333
	3	1	-2	0.32457	3.0810
	4	1	-1	0.32720	3.0562
	1	3	0	0.33053	3.0255
	0	1	2	0.33072	3.0237
	3	2	0	0.33436	2.9908

b

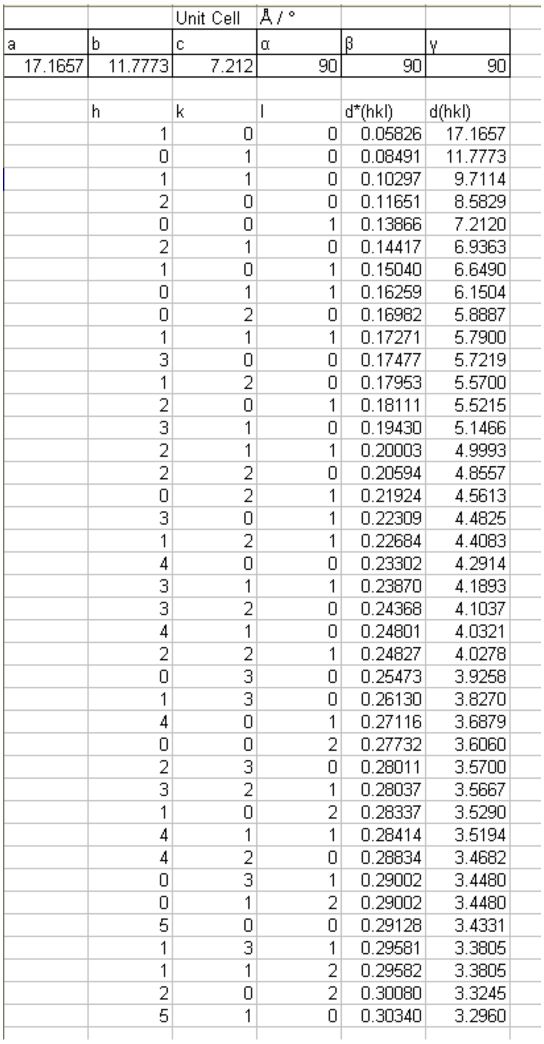

		Unit Cell	Å / °		
a	b	c	α	β	γ
17.1657	11.7773	7.212	90	90	90
	h	k	l	d*(hkl)	d(hkl)
	1	0	0	0.05826	17.1657
	0	1	0	0.08491	11.7773
	1	1	0	0.10297	9.7114
	2	0	0	0.11651	8.5829
	0	0	1	0.13866	7.2120
	2	1	0	0.14417	6.9363
	1	0	1	0.15040	6.6490
	0	1	1	0.16259	6.1504
	0	2	0	0.16982	5.8887
	1	1	1	0.17271	5.7900
	3	0	0	0.17477	5.7219
	1	2	0	0.17953	5.5700
	2	0	1	0.18111	5.5215
	3	1	0	0.19430	5.1466
	2	1	1	0.20003	4.9993
	2	2	0	0.20594	4.8557
	0	2	1	0.21924	4.5613
	3	0	1	0.22309	4.4825
	1	2	1	0.22684	4.4083
	4	0	0	0.23302	4.2914
	3	1	1	0.23870	4.1893
	3	2	0	0.24368	4.1037
	4	1	0	0.24801	4.0321
	2	2	1	0.24827	4.0278
	0	3	0	0.25473	3.9258
	1	3	0	0.26130	3.8270
	4	0	1	0.27116	3.6879
	0	0	2	0.27732	3.6060
	2	3	0	0.28011	3.5700
	3	2	1	0.28037	3.5667
	1	0	2	0.28337	3.5290
	4	1	1	0.28414	3.5194
	4	2	0	0.28834	3.4682
	0	3	1	0.29002	3.4480
	0	1	2	0.29002	3.4480
	5	0	0	0.29128	3.4331
	1	3	1	0.29581	3.3805
	1	1	2	0.29582	3.3805
	2	0	2	0.30080	3.3245
	5	1	0	0.30340	3.2960

6.2.3 Examples Where No Indexing was Possible

In a few cases, high quality diffraction patterns were obtained that could not be indexed to any zone axis of the compound(s) being analysed. The diffraction pattern in Figure 6.6, obtained from a sample of theophylline grown by cooling a saturated ethyl acetate solution, is shown as an example. Despite repeated attempts to index the pattern on the basis of Form II of theophylline, the phase known to be present in the bulk of the sample from XRPD analysis, no successful indexing was possible. Neither was it possible to index the pattern to the recently reported polymorph Form IV.[6] Likewise, comparison of the diffraction pattern reflections with XRPD peak positions of the other reported polymorphic forms of theophylline, for which there is no reported crystal structure (Forms I, III and a form recently reported by Roy et al (which will be referred to as Form V)),[7-9] did not give a match. It was later determined that the diffraction pattern came from a new polymorph of theophylline. This analysis required a combined TEM and crystal structure prediction approach which is described in Chapter 7.

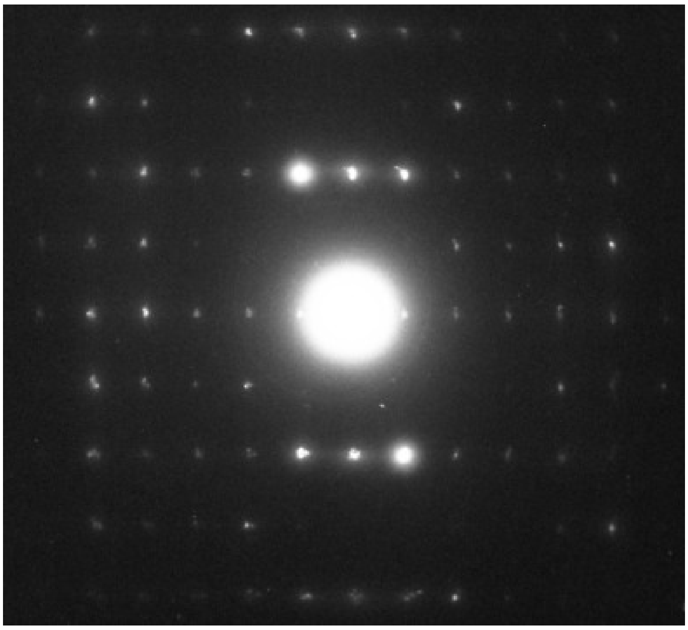

Figure 6.6 Diffraction pattern, from a sample thought to be solely Form II of theophylline, which could not be indexed to a zone axis of this theophylline polymorph.

Another system for which diffraction patterns were obtained that could not be indexed is the 1:1 RS-ibuprofen:nicotinamide cocrystal. This cocrystal has previously been prepared from the melt by Berry et al.[10] A small amount of a molten equimolar mixture of RS-ibuprofen and nicotinamide was thinly spread across a TEM sample support grid, and allowed to cool. A PLM image of the resulting sample displayed agglomerations of crystals of varying sizes and thicknesses (Figure 6.7a).

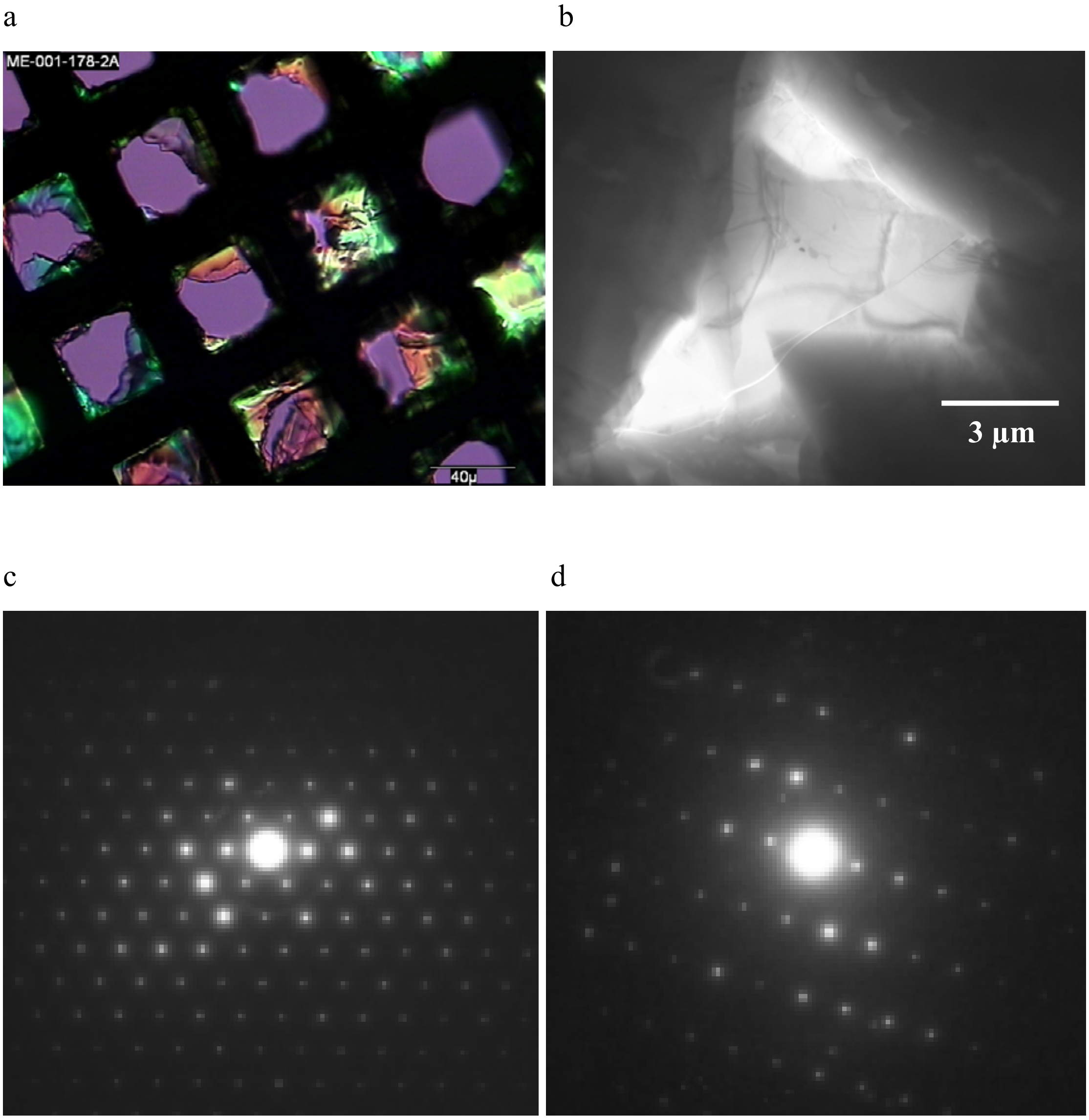

Figure 6.7 Analysis of a sample prepared by crystallising a molten equimolar mixture of RS-ibuprofen and nicotinamide. (a) PLM image of a sample of RS-ibuprofen and nicotinamide crystallised from the melt on a TEM sample grid. (b) TEM image of a sample of RS-ibuprofen and nicotinamide crystallised from the melt on a TEM sample grid. (c and d) Electron diffraction patterns from the same sample. It was not possible to index these diffraction patterns to any of the zone axes of the reported RS-ibuprofen:nicotinamide cocrystal.

The corresponding TEM image in Figure 6.7b showed that some regions of the sample were thin enough to observe features such as bend contours and cracks.

Several diffraction patterns were recorded from the sample (examples are shown in Figure 6.7c-d), but none could be satisfactorily indexed to the reported cocrystal phase. Neither could they be indexed to any zone axes of RS-ibuprofen or nicotinamide. This result suggests that a new crystal phase has been obtained, though further work would be required to determine the nature of this phase.

6.2.4 Identification of Crystal Phases in Mixtures

It was also found to be possible to use TEM for identifying the crystal phase of minor components in mixtures. The first example came from analysis of a sample of theophylline crystallised from methanol. The XRPD trace of this sample, which indicated that the sample was monophasic theophylline Form II, is shown in Figure 6.8 alongside a simulated trace of Form II.

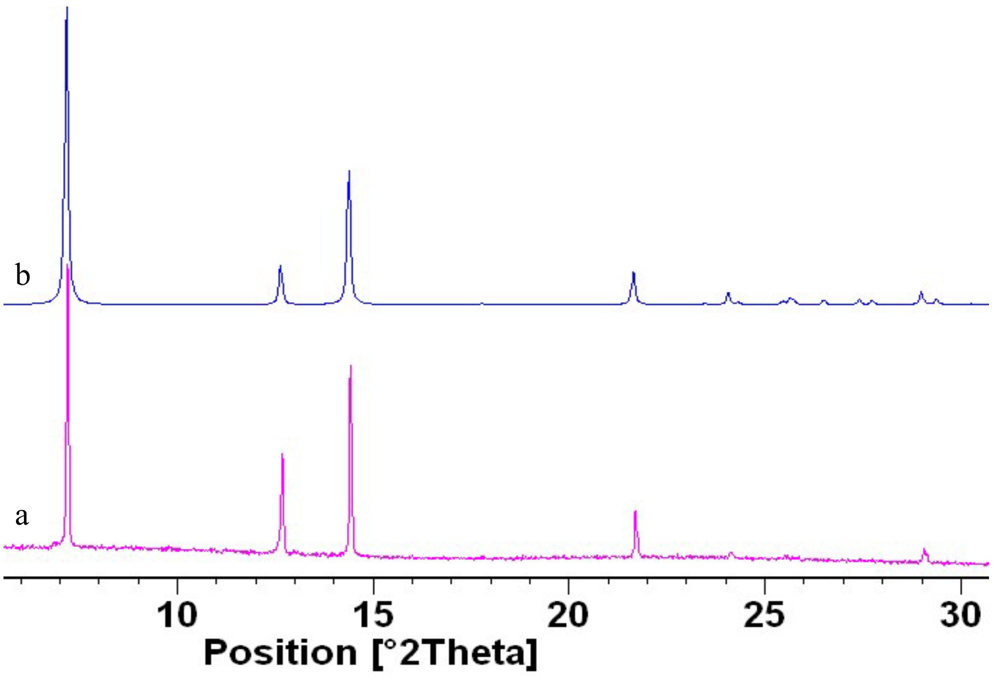

Figure 6.8 XRPD analysis of a sample of theophylline prepared by evaporative crystallisation from a solution in methanol. (a) XRPD trace of a sample of theophylline prepared by evaporative crystallisation from a solution in methanol. (b) Simulated XRPD trace of theophylline Form II (CSD ref BAPLOT01,[11] calculated to account for preferred orientation due to the plate-like crystal habit of the sample).

During TEM analysis of this sample, many crystals indexable as Form II of theophylline were observed (Figure 6.9a). However, TEM imaging also revealed a small number of crystals (approximately one in every hundred) that were morphologically different to the bulk sample. An image of one of these crystals is shown in Figure 6.9b. The corresponding diffraction pattern, included as an inset, could not be indexed to Form II of theophylline. By plotting the reflections on a 2θ scale, it was found that there was a probable match to Form V of theophylline (Figure 6.10). This example highlights the benefit that the high magnifications possible with TEM imaging give when studying mixtures of phases. The presence of Form V in the sample would not have been identified if it had been analysed by XRPD alone.

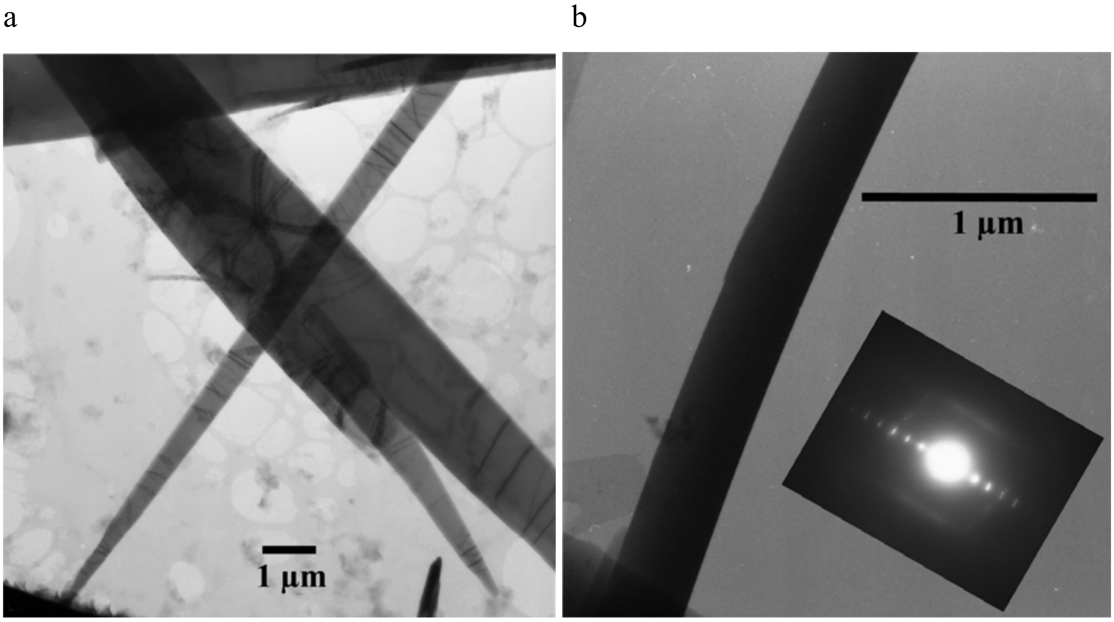

Figure 6.9 TEM characterisation of the sample that was analysed by XRPD in Figure 4.8. (a) TEM image of lath-shaped crystals of theophylline Form II. (b) TEM image of a crystal which appeared to be significantly darker, and therefore thicker, than other crystals of a similar size. The inset is an electron diffraction pattern from this crystal, in the correct relative orientation. The diffraction pattern was a match for the polymorph of theophylline that was reported by Roy et al.[9]

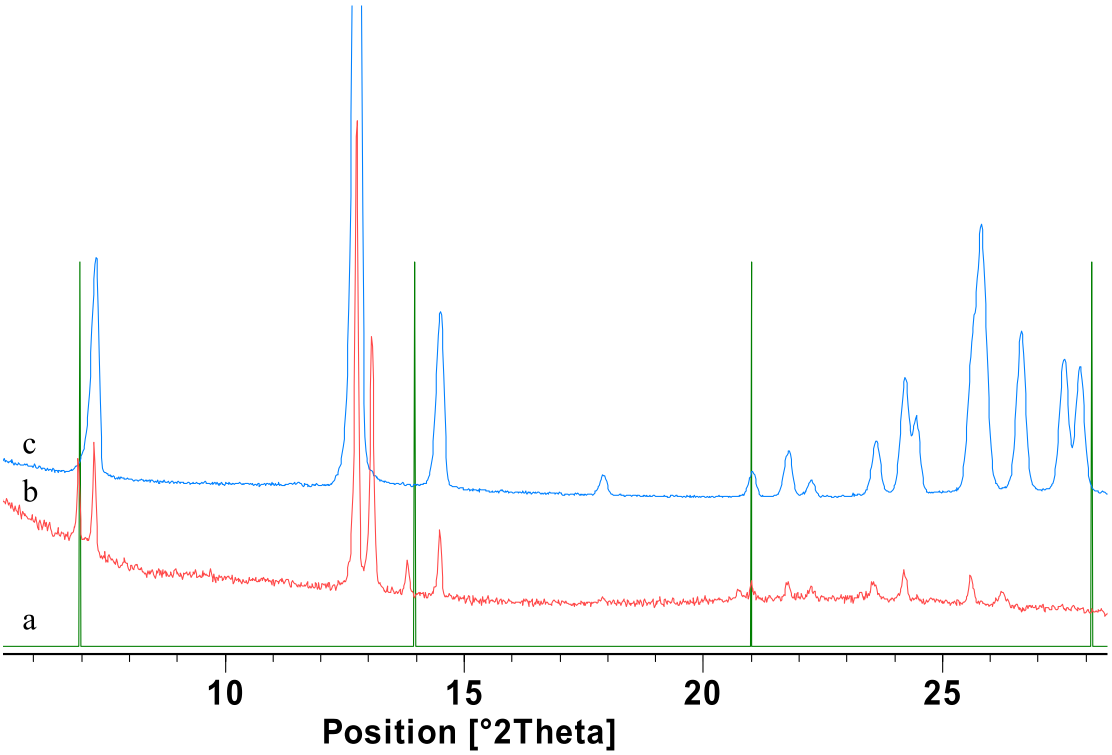

Figure 6.10 (a) Reflections from the electron diffraction pattern shown in Figure 6.9b plotted on a 2θ scale. (b) Reference XRPD trace of Form V of theophylline (this trace is a mixture of Form V and Form II). (b) Reference XRPD trace of Form II of theophylline.

A second example of the use of TEM for identifying the crystal phase of minor components in mixtures was obtained from characterisation of a 2:1 caffeine:oxalic acid cocrystal.[5] During an investigation by Cassidy et al,[12] it was found that on storing crystals of this cocrystal form at 75 %RH, small crystallites grew on their surface. SEM images of a crystal of the 2:1 caffeine:oxalic acid cocrystal before and after 1 week of storage at 75 % RH are shown in Figure 6.11.

The crystal form of the small crystallites was not known. It was speculated that they may be caffeine hydrate, but analysis by XRPD and Raman did not give any evidence to support this interpretation.

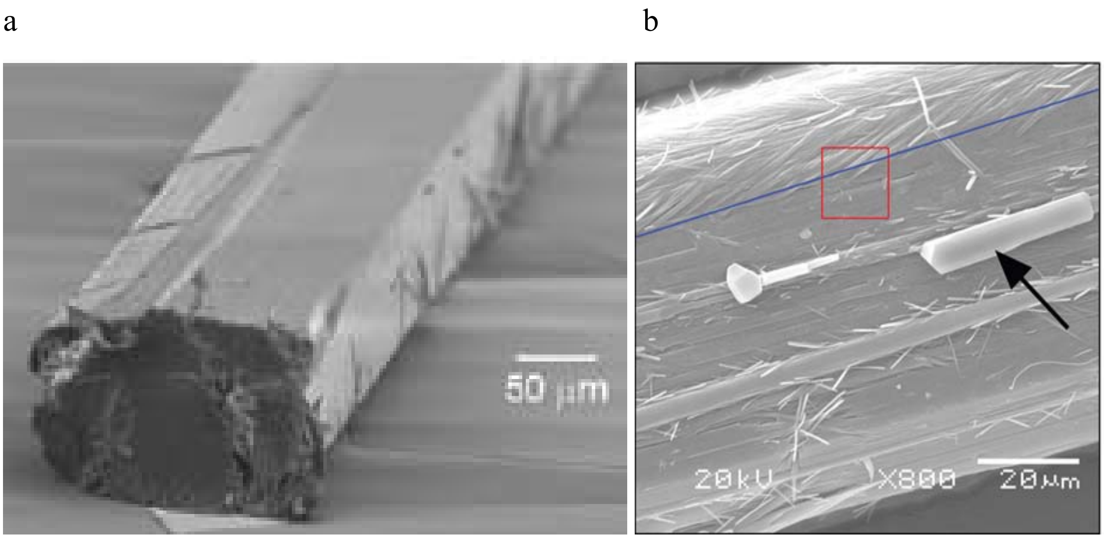

Figure 6.11 SEM analysis of a crystal of 2:1 caffeine:oxalic acid cocrystal (a) before and (b) after 1 week of storage at 75 %RH. Small crystallites formed on the surface of the crystal during storage. These images were recorded by Andrew Cassidy of the Department of Chemistry, University of Cambridge.[12]

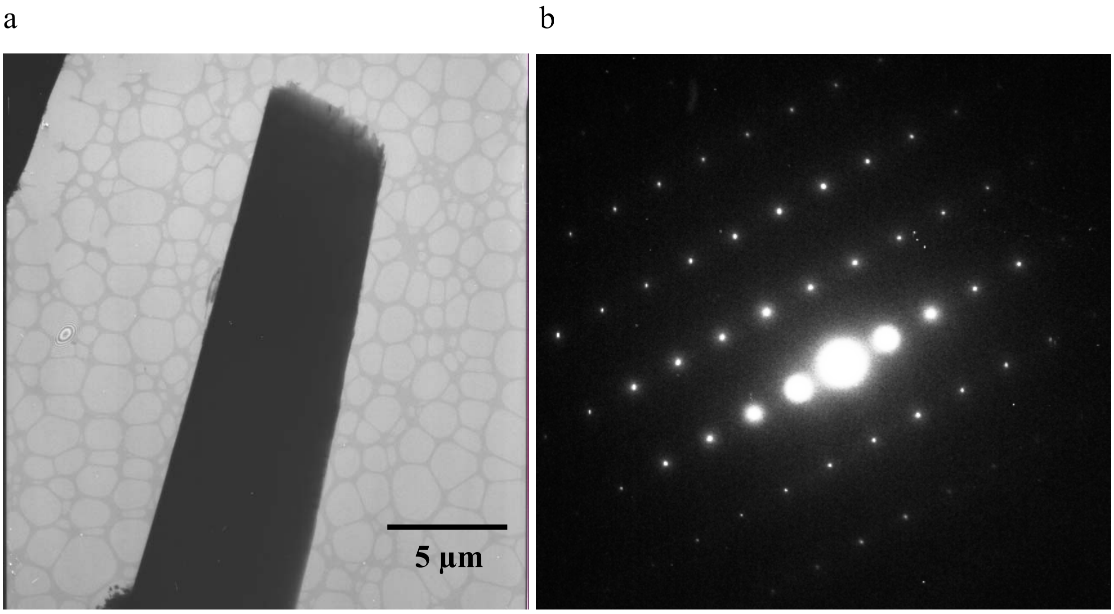

Figure 6.12 TEM analysis of a sample of 2:1 caffeine:oxalic acid cocrystal which had been stored at 75 %RH for 1 week. (a) A TEM image of a crystallite from this sample. It has a size and shape consistent with one of the surface crystallites in Figure 6.11b. (b) Corresponding electron diffraction pattern of the <121> zone axis of the 2:1 caffeine:oxalic acid cocrystal

A sample of 2:1 caffeine:oxalic acid cocrystal that had been stored at 75 %RH (supplied by Andrew Cassidy of the Department of Chemistry, University of Cambridge) was analysed by TEM to determine the crystal form of the surface crystallites. A TEM specimen was prepared by gently rolling crystals of the cocrystal on a TEM grid to transfer the crystallites. An example TEM image and diffraction pattern of one of the crystallites is shown in Figure 6.12. All of the crystallites that were analysed by TEM were found to be the 2:1 caffeine:oxalic acid cocrystal, demonstrating that the surface crystallites were in fact the same crystal form as the bulk sample.

6.3 Conclusions and Further Work

It was found that, if suitable electron diffraction patterns were recorded, the use of TEM to identify the crystal form of pharmaceutical samples was a fairly routine and widely applicable process. Furthermore, the detection of trace amounts of Form V of theophylline in a sample of Form II demonstrated that TEM has an advantage over techniques such as XRPD when analysing small amounts of material. This advantage could be utilised in areas such as solid form screening and patent infringement investigations.

One area of related further work would be to use electron diffraction patterns to determine the unit cell of new pharmaceutical crystal forms. The potential has been demonstrated by Li et al, who obtained unit cell parameters of roxifiban using a combined TEM and synchrotron XRPD approach.[13] During work for this thesis, several crystal forms for which there is no reported crystal structure have been analysed by TEM, and the diffraction patterns that have been obtained appear to be of sufficient quality for unit cell determination. For example, several high quality diffraction patterns were obtained from a sample of Form III of the caffeine:theophylline cocrystal (Figure 6.13). Appropriate software would be required to facilitate the indexing process.

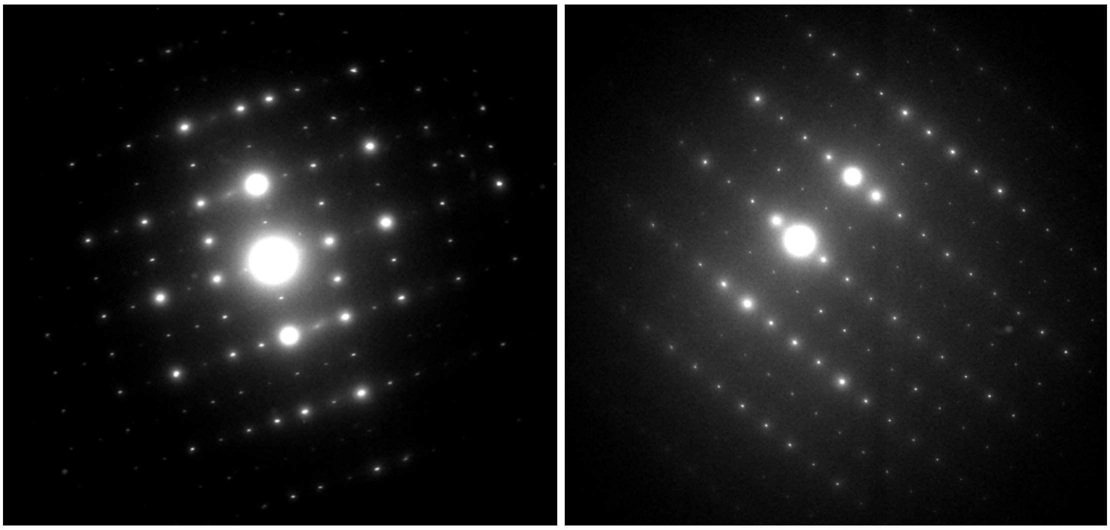

Figure 6.13 Electron diffraction patterns of Form III of the caffeine:theophylline cocrystal. It may be possible to use these patterns, and others, to determine the unit cell parameters of this crystal form.

6.4 References

1. Haisa M., Kashino S., Kawai R., Maeda H. The monoclinic form of p-hydroxyacetanilide. *Acta Crystallogr., Sect. B*, 1976, B32(4), 1283-1285.

2. Di Martino P., Conflant P., Drache M., Huvenne J. P., Guyot-Hermann A. M. Preparation and physical characterization of forms II and III of paracetamol. *J. Therm. Anal.*, 1997, 48(3), 447-458.

3. Nichols G., Frampton C. S. Physicochemical Characterization of the Orthorhombic Polymorph of Paracetamol Crystallized from Solution. *J. Pharm. Sci.*, 1998, 87(6), 684-693.

4. Mirmehrabi M., Rohani S., Murthy K. S. K., Radatus B. Characterization of tautomeric forms of ranitidine hydrochloride: thermal analysis, solid-state NMR, X-ray. *J. Cryst. Growth*, 2004, 260(3-4), 517-526.

5. Trask A. V., Motherwell W. D. S., Jones W. Pharmaceutical cocrystallization: Engineering a remedy for caffeine hydration. *Cryst. Growth Des.*, 2005, 5(3), 1013-1021.

6. Seton L., Khamar D., Bradshaw I. J., Hutcheon G. A. Solid State Forms of Theophylline: Presenting a New Anhydrous Polymorph. *Cryst. Growth Des.*, 2010, 10(9), 3879-3886.

7. Suzuki E., Shimomura K., Sekiguchi K. Thermochemical study of theophylline and its hydrate. *Chem. and Pharm. Bull.*, 1989, 37(2), 493-497.

8. Matsuo K., Matsuoka M. Solid-State Polymorphic Transition of Theophylline Anhydrate and Humidity Effect. *Cryst. Growth Des.*, 2007, 7(2), 411-415.

9. Roy C., Vega-Gonzalez A., Subra-Paternault P. Theophylline formulation by supercritical antisolvents. *Int. J. Pharm.*, 2007, 343(1-2), 79-89.

10. Berry D. J., Seaton C. C., Clegg W., Harrington R. W., Coles S. J., Horton P. N., Hursthouse M. B., Storey R., Jones W., Friscic T., Blagden N. Applying Hot-Stage Microscopy to Co-Crystal Screening: A Study of Nicotinamide with Seven Active Pharmaceutical Ingredients. *Cryst. Growth Des.*, 2008, 8(5), 1697-1712.

11. Ebisuzaki Y., Boyle P. D., Smith J. A. Methylxanthines. I. Anhydrous theophylline. *Acta Crystallogr., Sect. C: Cryst. Struct. Commun.*, 1997, C53(6), 777-779.

12. Cassidy A. M. C., Gardner C. E., Jones W. Following the surface response of caffeine cocrystals to controlled humidity storage by atomic force microscopy. *Int. J. Pharm.*, 2009, 379(1), 59-66.

13. Li Z. G., Harlow R. L., Foris C. M., Li H., Ma P., Vickery R. D., Maurin M. B., Toby B. H. Polymorph determination for the GP IIb/IIIa antagonist, roxifiban. *J. Pharm. Sci.*, 1999, 88(3), 297-301.

7 Crystal Structure Determination using a Combined TEM and Crystal Structure Prediction Approach

7.1 Introduction

This Chapter describes the development of a novel approach to crystal structure determination that builds on the phase identification work described in Chapter 6.

The ability to routinely solve crystal structures by X-ray diffraction was an important achievement of the 20th century, and is a cornerstone of analytical chemistry. There are, however, limitations with the technique, especially for weakly diffracting organic compounds, and for strongly diffracting crystals if they are very small. Even with a synchotron X-ray source, it is not normally possible to solve a structure from a single crystal with a thickness of less than 1 μm. Also, structure solution from powder X-ray data is unlikely to be successful with multi-component mixtures (even small amounts of impurities can make pattern indexing difficult), or with binary mixtures where the compound of interest is present as a minor phase.[1,2] These limitations could be overcome in many cases by using TEM, since diffraction data can be obtained from much smaller amounts of sample (< 1 fg).[3] Also, it is possible to analyse many different crystals from a sample individually, allowing the characterisation of minor phases in mixtures. However, solving crystal structures from electron diffraction patterns is not straightforward.[2,4] Even if a crystal is sufficiently thin for TEM analysis, and can be analysed for sufficient time to obtain multiple diffraction patterns before degrading, there are limited tilt ranges in TEM instruments and it is difficult to obtain accurate diffraction intensities due to multiple (dynamical) scattering.[4,5]

Here, an alternative approach for determining the crystal structure of phases, based on TEM, is described. In this method, a set of potential low energy crystal structures for a molecule is generated using crystal structure prediction (CSP). TEM analysis, and in particular electron diffraction, is then used to identify which of these potential crystal structures matches the experimental sample.

CSP is an approach for computationally generating potential crystal structures.[6,7] One of the main uses of CSP is providing information on the likelihood of finding new polymorphs of a compound. For example, CSP may generate structures that have not been observed experimentally, but that have a similar, or lower, lattice energy than the known forms of the compound.[8] CSP is also used to determine the crystal structure of polymorphs when it is not possible to grow crystals suitable for structure solution by single crystal X-ray diffraction. This is typically done by comparing an experimental XRPD trace of the sample of interest with simulated traces calculated for each of the potential crystal structures that were generated by CSP.[9] Recently, a similar approach using SSNMR instead of XRPD has been reported.[10]

All of the CSP data sets described in this Chapter were provided by Dr. Graeme Day and Dr. Katarzyna Heyczyk of the Department of Chemistry, University of Cambridge.

The combined TEM/CSP approach to crystal structure determination was applied to the identification of a new polymorph of the compound theophylline.

7.2 Results

Initial work in this investigation was performed with electron diffraction patterns from a known crystal form to establish whether, from a set of theoretical structures generated by CSP, the structure corresponding to this form could be identified using the indexing procedure described in Chapters 5 and 6.

7.2.1 Development Work with Paracetamol Form II

CSP work on paracetamol generated a set of 14 potential crystal structures with lattice energies within 10 $kJ.mol^{-1}$ of the global minimum. The lowest in energy (AM30) was found to match Form I of paracetamol, and the second lowest in energy (CB47) to match Form II.[11] The unit cell parameters of these 14 crystal structures are listed in Table 7.1, and were used to calculate sets of d-spacings and interplanar angles.

Table 7.1 Unit cell parameters for the 14 crystal structures of paracetamol generated by CSP that have lattice energies within 10 kJ.mol^{-1} of the global minimum.[11]

CSP Structure	Unit Cell Parameters						Space group
	a / Å	b / Å	c / Å	α / °	β / °	γ / °	
AM30	12.119	8.944	7.278	90	80.03	90	$P2_1/n$
CB47	17.249	12.086	7.382	90	90	90	Pbca
AI22	8.247	6.751	16.668	90	126.23	90	$P2_1/c$
AY8	15.874	4.519	10.692	90	90	90	$Pca2_1$
CC19	31.121	5.074	9.886	90	82.23	90	$P2_1$
AQ6	7.344	16.281	6.571	90	90	90	$P2_12_12_1$
AK6	16.128	5.049	9.624	90	79.12	90	$P2_1/c$
AQ14	7.071	15.834	6.776	90	90	90	$P2_12_12_1$
CB9	17.451	12.162	7.301	90	90	90	Pbca
CC8	6.841	16.665	13.498	90	90	90	Pbca
AK22	15.837	5.067	9.870	90	86.63	90	$P2_1/c$
AI16	7.578	8.090	12.704	90	103.33	90	$P2_1/c$
AM4	5.929	7.604	17.07	90	80.68	90	$P2_1/c$
AK4	19.035	5.296	8.080	90	101.63	90	$P2_1/c$

The two electron diffraction patterns shown in Figure 7.1, obtained from the sample of Form II of paracetamol that is described on Page 149, were used in the study. Three d-spacings and three corresponding interplanar angles were measured from the two patterns (Pattern a – 11.82 Å, 8.82 Å, 7.07 Å, 89.8 °, 53.0 ° and 37.0 °. Pattern b – 17.44 Å, 4.61 Å, 4.47 Å, 89.2 °, 75.9 ° and 14.9 °). The diffraction patterns were indexed to the <001> zone axis and <121> zone axis of Form II of paracetamol respectively (using CSD crystal structure HXACAN23).[12]

Attempts were made to index the two diffraction patterns against the 14 theoretical paracetamol structures that were generated by CSP, using tolerances of d +/- 5 % and θ +/- 3 °. After numerical matching and visual comparison of experimental and simulated patterns, there were three possible zone axis matches for Pattern a, and two possible zone axis matches for Pattern b (sets of symmetry equivalent zone axes were counted as one match) from these 14 structures (see Table 7.2).

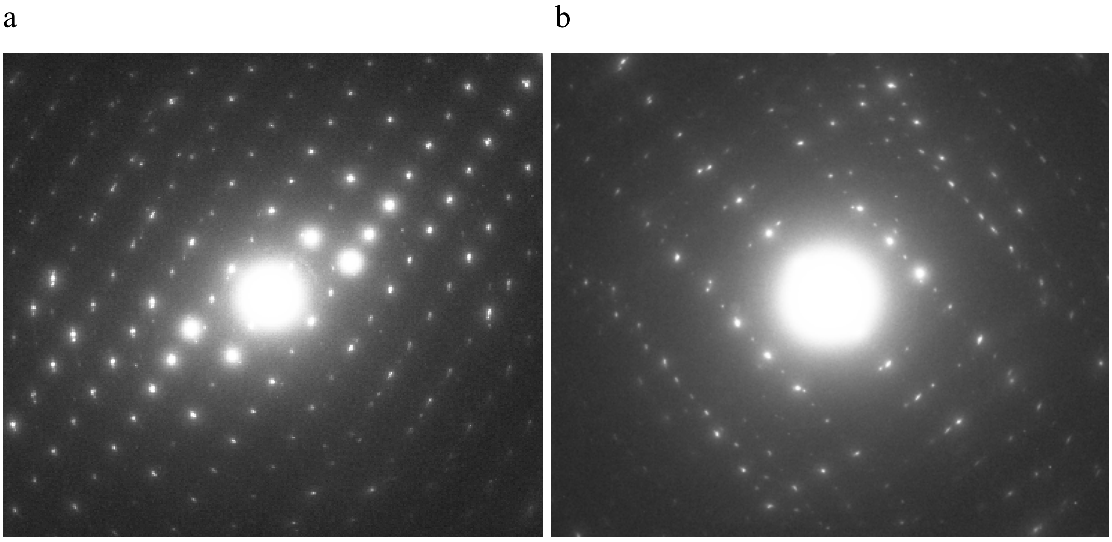

Figure 7.1 Electron diffraction patterns of (a) the <001> zone axis and (b) the <012> zone axis of Form II of paracetamol.

Table 7.2 Zone axes of the 14 paracetamol CSP structures that could be matched to the diffraction patterns of Form II of paracetamol shown in Figure 7.1.

Pattern	CSP Structure	Zone Axis	D-spacings and Interplanar Angles					
			d_1 / Å	d_2 / Å	d_3 / Å	θ_1 / °	θ_2 / °	θ_3 / °
a	AM30	<001>	11.936	8.944	7.157	90.0	53.2	36.8
a	CB47	<001>	12.086	8.624	7.020	90.0	54.5	35.5
a	CB9	<001>	12.162	8.725	7.090	90.0	54.3	35.7
b	CB47	<012>	17.249	4.676	4.513	90.0	74.8	15.2
b	CC8	<012>	16.665	4.805	4.617	90.0	73.9	16.1

The results showed that it would not be possible to use either of the diffraction patterns alone to determine unambiguously which of the CSP structures was a match for the experimental sample of Form II of paracetamol. However, the only theoretical structure to which both diffraction patterns could be indexed was CB47. This is the CSP structure that corresponds to Form II of paracetamol.

This study with Form II of paracetamol demonstrated that using electron diffraction patterns it was possible to identify, from a set of theoretical crystal structure generated by CSP, which theoretical structure corresponded to the crystal form of the sample being analysed.

7.2.2 Development Work with Paracetamol Form I

The above procedure was repeated for form I of paracetamol. The electron diffraction patterns shown in Figure 7.2, obtained from a sample of Form I of paracetamol prepared by crystallisation from the melt, were used in the study. Three d-spacings and three corresponding interplanar angles were measured from the two patterns (Pattern a – 11.51 Å, 5.65 Å, 5.26 Å, 85.4 °, 67.7 ° and 26.6 °. Pattern b – 6.34 Å, 5.80 Å, 5.67 Å, 64.4 °, 62.0 ° and 53.7 °). These diffraction patterns were indexed to the <011> zone axis and <010> zone axis of Form I of paracetamol respectively (using CSD crystal structure HXACAN01).[13]

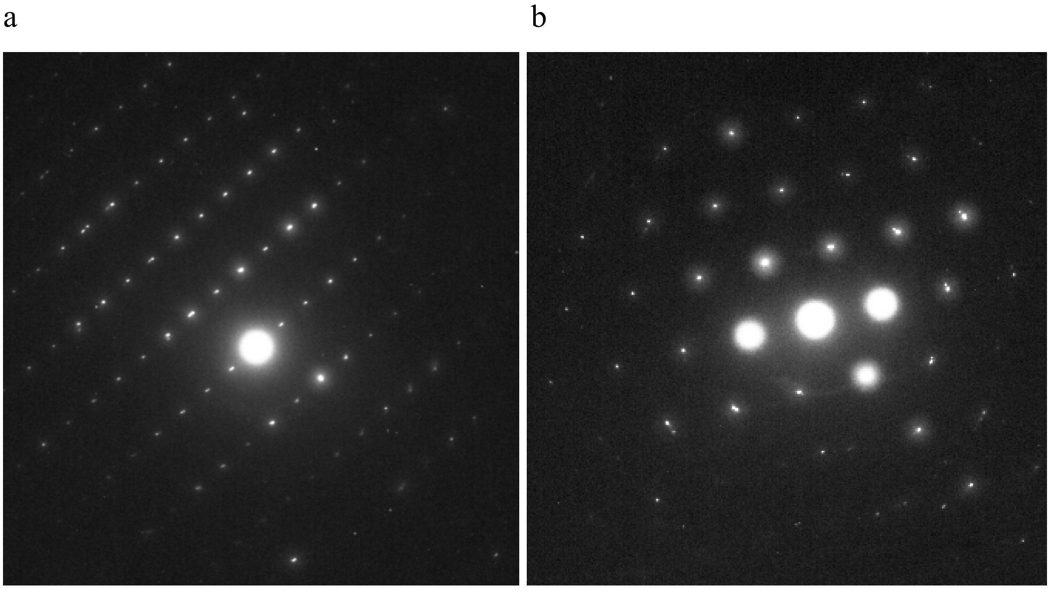

Figure 7.2 Electron diffraction patterns of (a) the <011> zone axis and (b) the <010> zone axis of Form I of paracetamol.

Attempts were made to index the two diffraction patterns against the 14 theoretical paracetamol structures that were generated by CSP, using tolerances of d +/- 5 % and θ +/- 3 °. After numerical matching and visual comparison of experimental and simulated patterns, there were no possible zone axis matches for Pattern a, and two possible zone axis matches for Pattern b. These matches are listed in Table 7.3.

Table 7.3 Zone axes of the 14 paracetamol CSP structures that could be matched to the diffraction patterns of Form I of paracetamol shown in Figure 7.2.

Pattern	CSP Structure	Zone Axis	D-spacings and Interplanar Angles					
			d_1 / Å	d_2 / Å	d_3 / Å	θ_1 / °	θ_2 / °	θ_3 / °
b	CB47	<211>	6.300	5.918	5.703	64.6	60.5	54.9
b	CB9	<211>	6.260	5.892	5.742	63.7	60.9	55.3

None of the 14 CSP structures could be matched to both pattern a and pattern b. This was an unexpected result as it had been possible to index these diffraction patterns to the experimental crystal structure of Form I of paracetamol (CSD structure HXACAN01). It was therefore expected that they would also match the CSP crystal structure that is known to correspond to Form I of paracetamol, AM30.

The two diffraction patterns were therefore re-indexed against the 14 paracetamol CSP structures using widened tolerances of d +/- 7.5 % and θ +/- 4 °. After numerical matching and visual comparison of experimental and simulated patterns, there was one possible zone axis match for Pattern a, and five possible zone axis matches for Pattern b. These matches are listed in Table 7.4.

Table 7.4 Zone axes of the 14 paracetamol CSP structures that were matched to the diffraction patterns of Form I of paracetamol in Figure 7.2 using widened tolerances.

Pattern	CSP Structure	Zone Axis	D-spacings and Interplanar Angles					
			d_1 / Å	d_2 / Å	d_3 / Å	θ_1 / °	θ_2 / °	θ_3 / °
a	AM30	<011>	11.936	5.593	5.350	82.2	71.4	26.4
b	AM30	<010>	6.676	5.968	5.723	66.5	61.6	51.8
b	CB47	<211>	6.300	5.918	5.703	64.6	60.5	54.9
b	CB9	<211>	6.260	5.892	5.742	63.7	60.9	55.3
b	CB9	<132>	5.892	5.599	5.248	66.3	59.1	54.6
b	CC8	<121>	6.256	6.102	5.730	65.2	58.5	56.3

It was possible to index both pattern a and pattern b of the paracetamol Form I electron diffraction patterns to only one of the theoretical crystal structures generated by CSP, AM30. This is the CSP structure that matches Form I of paracetamol.

The reason that the tolerances had to be widened before both electron diffraction patterns could be matched to the predicted crystal structure AM30, is that there are slight differences between this theoretical structure and the actual, experimentally observed crystal structure of Form I of paracetamol (HXACAN01).[13] The predicted structure has the same space group, intermolecular interactions and overall arrangement of molecules as are found in Form I of paracetamol, but the exact positions and orientations of molecules are not reproduced perfectly. This can be seen by comparing the unit cell parameters of the observed and theoretical structures of Form I of paracetamol (Table 7.5). In contrast, there is a much better match between the observed and theoretical structures of Form II of paracetamol (CSD ref. HXACAN23,[12] and CB47 respectively), which is why indexing electron diffraction patterns of this crystal form to the predicted structure was more straightforward. The effect of these differences can also be seen in the simulated XRPD traces of these crystal structures (Figure 7.3). The simulated XRPD traces of the observed and theoretical crystal structures of Form II of paracetamol are more closely matched than those of Form I of paracetamol.

Table 7.5 Comparison of unit cell parameters for an observed crystal structure with those of the corresponding theoretical crystal structure, generated by CSP, for both Form I and Form II of paracetamol. Differences are given in brackets (as percentages). The table indicates the greater similarity between the observed and predicted structures of Form II in comparison to those of Form I.

Crystal Structure	Unit Cell Parameters					
	a / Å	b / Å	c / Å	α / °	β / °	γ / °
HXACAN01 (Experimental Form I)	12.930	9.400	7.100	90	115.90	90
AM30 (Predicted Form I)*	13.011 (0.63 %)	8.944 (4.85 %)	7.278 (2.51 %)	90	113.46 (2.1 %)	90
HXACAN23 (Experimental Form II)	17.162	11.837	7.406	90	90	90
CB47 (Predicted Form II)	17.249 (0.51 %)	12.086 (2.10 %)	7.382 (0.32 %)	90	90	90

* The unit cell parameters were recalculated to match the cell setting in HXACAN01

There will always be slight differences between experimental crystal structures, and equivalent structures generated by CSP, as when generating structures it is not possible to exactly model the distribution of electron density around atoms or the attractive and repulsive forces that dictate the positions of atoms within a crystal structure. The magnitude of these differences will govern the ease with which electron diffraction patterns can be matched to the correct CSP structure when using the combined TEM/CSP method for determining the crystal structure of samples.

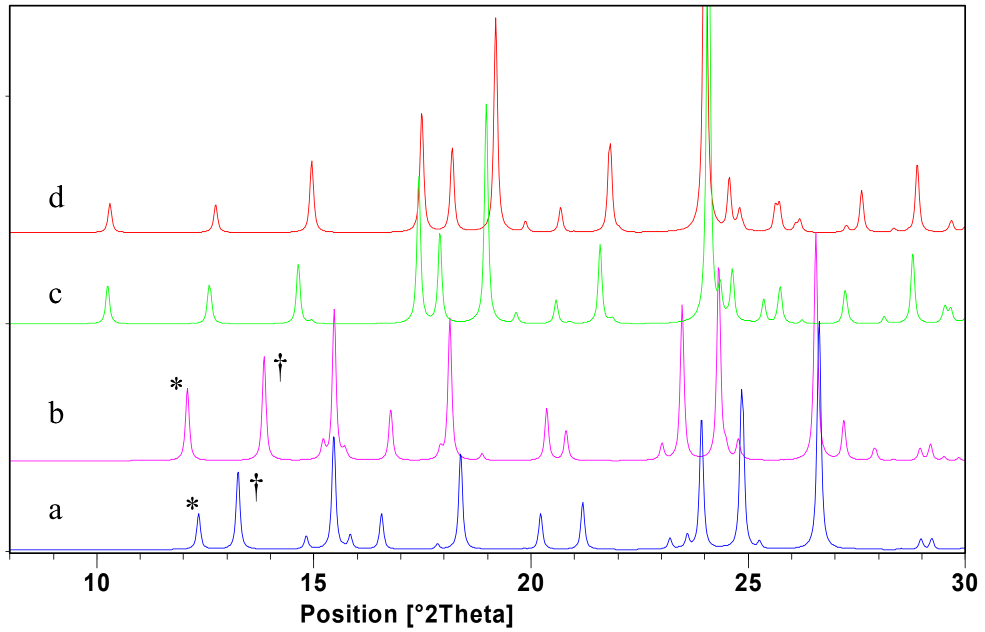

Figure 7.3 Comparison of simulated XRPD traces of observed and theoretical crystal structures of Form I and Form II of paracetamol. (a) Theoretical crystal structure of paracetamol Form I, AM30. (b) Observed crystal structure of paracetamol Form I, HXACAN01.[13] The peaks in these traces that are marked with an asterisk are due to diffraction from equivalent crystal planes, as are the peaks marked with a † symbol. (c) Theoretical crystal structure of paracetamol Form II, CB47. (d) Observed crystal structure of paracetamol Form II, HXACAN23.[12]

7.2.3 Development Work with Theophylline Form II

A set of predicted theophylline crystal structures was generated by CSP. A plot of lattice energy against density for these predicted structures is shown in Figure 7.4. The second lowest energy structure, #2, was found to be a match to the experimental crystal structure of the thermodynamically stable polymorph of theophylline, Form II (CSD ref. BAPLOT01).[14]

The lowest energy predicted structure does not correspond to a known polymorph of theophylline. This is an indication that further experimental work should be conducted in order to isolate this potential crystal phase experimentally.

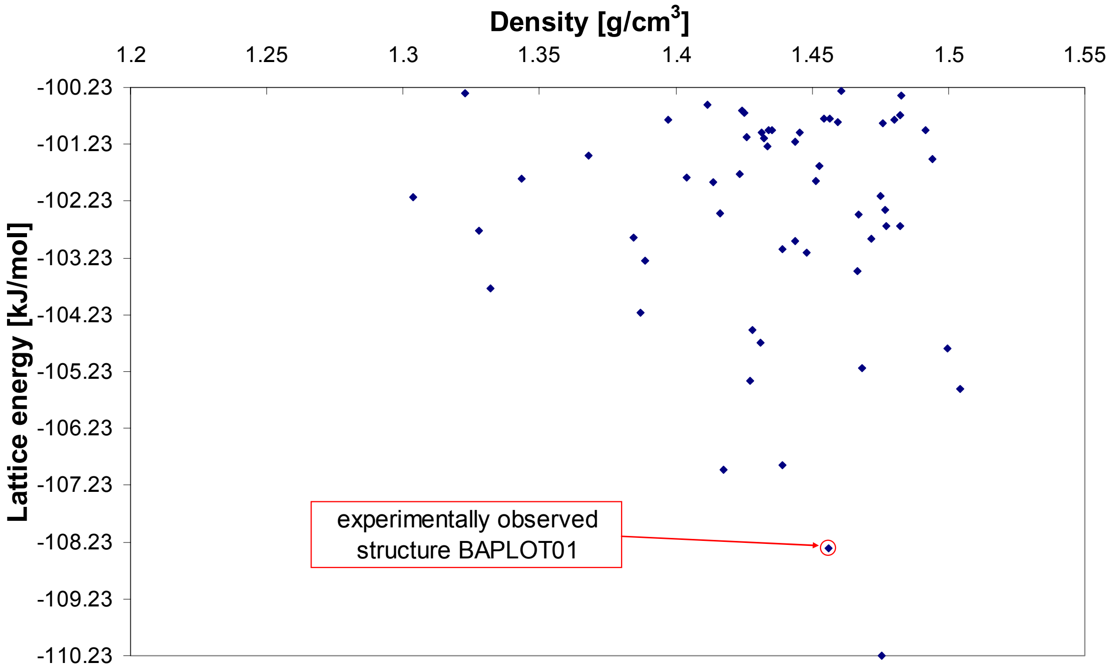

Figure 7.4 A plot of lattice energy against density for predicted crystal structures of theophylline that have lattice energies within 10 kJ.mol^{-1} of the global minimum. This plot was prepared by Katarzyna Hejczyk of the Department of Chemistry, University of Cambridge.

The 20 lowest energy structures were used for investigating the combined TEM/CSP method for crystal structure determination. The unit cell parameters of these 20 structures are listed in Table 7.6, and were used to calculate sets of d-spacings and interplanar angles.

The electron diffraction patterns shown in Figure 7.5, obtained from a sample of Form II of theophylline prepared by cooling a saturated solution of theophylline in nitromethane, were used in the study. The crystal form of this sample was determined by XRPD analysis. Three d-spacings and three corresponding interplanar angles were measured from the two patterns (Pattern a – 4.23 Å, 3.50 Å, 3.50 Å, 65.7 °, 65.3 ° and 48.9 °. Pattern b – 8.53 Å, 3.80 Å, 3.48 Å, 89.9 °, 66.2 ° and 24.0 °). The diffraction patterns were indexed to the <100> zone axis and <110> zone axis of Form II of theophylline respectively (using CSD crystal structure BAPLOT01).

Table 7.6 Unit cell parameters for the experimental structure of Form II of theophylline and the 20 lowest energy predicted crystal structures of theophylline.

CSP Structure	Unit Cell Parameters						Space group
	a / Å	b / Å	c / Å	α / °	β / °	γ / °	
Experimental Form II (BAPLOT01)	24.612	3.830	8.501	90	90	90	$Pna2_1$
#1	8.130	9.519	10.512	90	94.43	90	$P2_1/c$
#2	24.614	3.927	8.503	90	90	90	$Pna2_1$
#3	9.566	6.892	25.609	90	90	90	Pbca
#4	10.346	9.635	8.359	90	93.55	90	$P2_1/c$
#5	7.608	14.086	7.620	90	103.08	90	$P2_1/c$
#6	3.926	25.490	8.385	90	92.44	90	Cc
#7	8.853	12.937	7.130	90	93.52	90	$P2_1/c$
#8	7.495	7.551	8.354	67.44	66.22	78.50	P-1
#9	9.567	10.069	17.365	90	90	90	Pbca
#10	13.725	13.065	9.510	90	100.61	90	C2/c
#11	16.062	13.014	9.565	90	120.34	90	C2/c
#12	9.285	24.195	3.999	90	90	90	$Pna2_1$
#13	15.454	13.036	8.195	90	98.70	90	C2/c
#14	19.979	9.493	10.154	90	116.50	90	C2/c
#15	7.024	18.480	13.109	90	103.76	90	C2/c
#16	13.108	15.806	4.014	90	90	90	$Pna2_1$
#17	4.232	12.214	16.045	90	92.10	90	$P2_1/c$
#18	3.906	15.475	13.468	90	92.73	90	$P2_1/c$
#19	3.938	27.208	8.593	90	110.13	90	$P2_1/c$
#20	3.977	24.389	9.294	90	91.46	90	$P2_1/c$

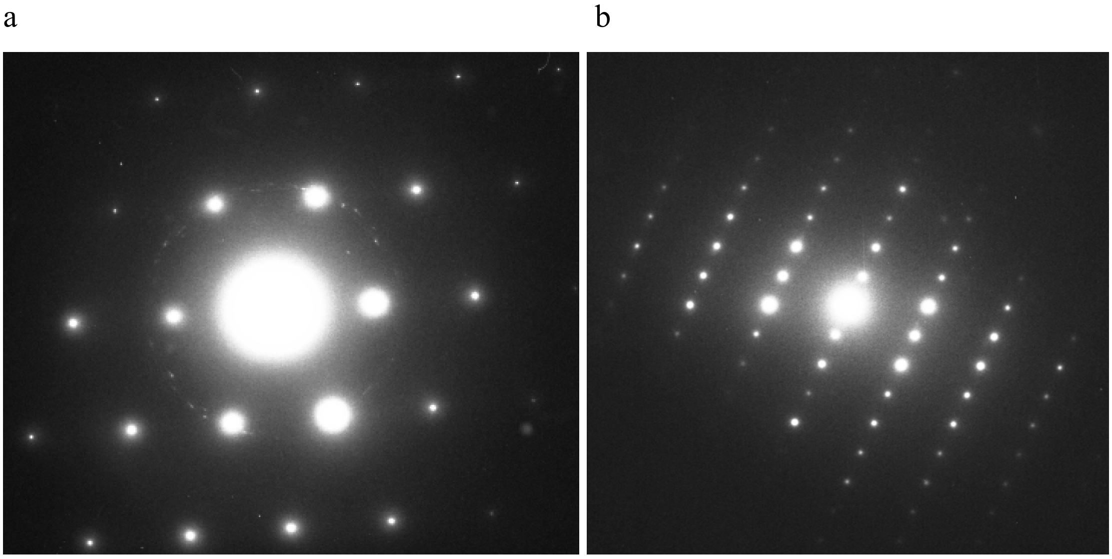

Figure 7.5 Electron diffraction patterns of (a) the <100> zone axis and (b) the <110> zone axis of Form II of theophylline.

Attempts were made to index the two diffraction patterns against the 20 theoretical theophylline crystal structures generated by CSP, using tolerances of d +/- 7.5 % and θ +/- 3 °. After numerical matching and visual comparison of experimental and simulated patterns, it was found that there were there were many possible zone axis matches for both Pattern a and Pattern b. Numbers of zone axis matches are listed in Table 7.7 (sets of symmetry equivalent zone axes were counted as one match).

Five of the crystal structures generated by CSP (#2, #7, #12, #14 and #20) contained zone axes that were consistent with both of the theophylline diffraction patterns. This meant that it was not possible to unambiguously determine which of the structures corresponded to the crystal phase being analysed.

The indexing procedure was repeated using tighter tolerances of d +/- 4 % and θ +/- 3 °, and with data from an additional experimental diffraction pattern, the <111> zone axis pattern shown in Figure 7.6 (Pattern c). After numerical matching and visual comparison of experimental and simulated patterns, only theoretical structure #2 could be matched to all three of the experimental diffraction patterns. Crystal structure #2 is the CSP structure that matches Form II of theophylline.

Table 7.7 Numbers of zone axes of the 20 theophylline CSP structures that could be matched to the diffraction patterns of Form II of theophylline shown in Figure 7.5.

CSP Structure	Number of Matches		CSP Structure	Number of Matches	
	Pattern a	Pattern b		Pattern a	Pattern b
#1	1	0	#11	> 5	0
#2	4	5	#12	1	1
#3	0	0	#13	4	0
#4	0	0	#14	> 5	2
#5	2	0	#15	> 5	0
#6	0	2	#16	2	0
#7	1	1	#17	2	0
#8	3	0	#18	4	0
#9	0	0	#19	3	0
#10	> 5	0	#20	1	2

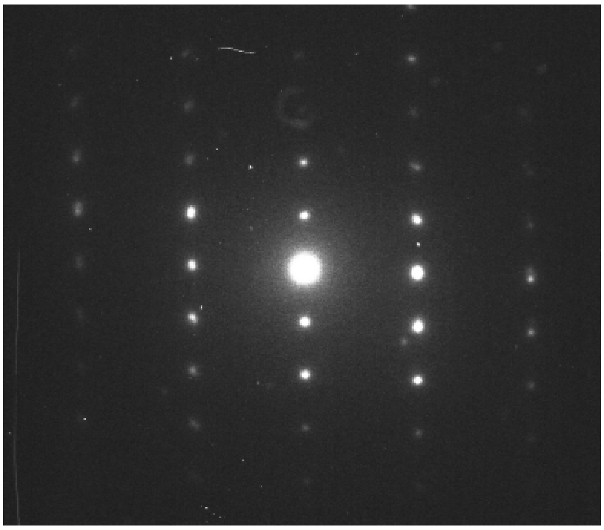

Figure 7.6 Electron diffraction pattern of the <111> zone axis of Form II of theophylline (Pattern c).

In this example, uniquely matching the experimental electron diffraction patterns from a sample of Form II of theophylline to one of the 20 predicted CSP structures of theophylline was made difficult by the large number of zone axes of the CSP structures which could be fitted to the experimental electron diffraction patterns. This large number of matches resulted from the small d-spacings of the reflections in experimental diffraction patterns from Form II of theophylline (even though the experimental diffraction patterns were from low index zone axes). The normal to the plate face of crystals of theophylline is in the [100] crystallographic direction, and so it is the <100> zone axis that is most likely to be observed during TEM diffraction analysis. All crystal planes in the <100> zone that do not give systematic absences have d-spacings of < 5 Å. As described in Section 6.2.2, as interplanar spacings decrease, the possibility of coincidental matches increases, making corresponding reflections difficult to uniquely identify.

Despite these difficulties, it was still possible to match the electron diffraction patterns to the CSP structure corresponding to Form II of theophylline.

7.2.4 Application of the TEM/CSP Method to Scyllo-Inositol

As a further test of the TEM/CSP method it was applied to crystal structure determination with scyllo-inositol, a potential treatment for Alzheimer's disease.[15] The investigation was approached as if an unknown crystal form was being investigated (a blind test). The sample of scyllo-inositol used in the study was not characterised prior to the TEM/CSP work and so it was not known which of the two reported polymorphs of scyllo-inositol[9] was present.

A set of predicted scyllo-inositol crystal structures was generated by CSP.[9] These structures were supplied without knowledge of which structures corresponded to the known polymorphs of scyllo-inositol. The unit cell parameters of the 11 crystal structures with lattice energies within 20 kJ.mol^{-1} of the global minimum are listed in Table 7.8, and were used to calculate sets of d-spacings and interplanar angles.

Table 7.8 Unit cell parameters for the 11 lowest energy predicted crystal structures of scyllo-inositol.

CSP Structure	Unit Cell Parameters						Space group
	a / Å	b / Å	c / Å	α / °	β / °	γ / °	
S1	5.001	6.437	11.420	90.00	115.43	90.00	$P2_1/c$
S2	12.012	12.012	4.270	90.00	90.00	120.00	R-3
S3	21.484	6.291	11.480	90.00	71.10	90.00	C2/c
S4	20.173	6.352	11.427	90.00	97.43	90.00	C2/c
S5	9.565	6.289	11.486	90.00	82.22	90.00	$P2_1/c$
S6	8.768	7.941	9.564	90.00	147.23	90.00	$P2_1/c$
S7	8.770	7.939	9.566	90.00	147.24	90.00	$P2_1/c$
S8	11.011	6.876	11.127	90.00	124.78	90.00	$P2_1/c$
S9	6.446	6.856	8.145	92.76	104.84	94.46	P-1
S10	10.212	6.513	4.996	90.00	91.11	90.00	$P2_1$
S11	10.523	7.183	10.980	90.00	122.16	90.00	$P2_1/c$

The electron diffraction patterns shown in Figure 7.7 were obtained from TEM analysis of a sample of scyllo-inositol that was prepared by gently crushing crystals between two glass slides and transferring the fragments to a TEM sample grid. Three d-spacings and three corresponding interplanar angles were measured from the two patterns (Pattern a – 10.70 Å, 6.59 Å, 5.60 Å, 89.8 °, 58.4 ° and 31.6 °. Pattern b – 6.65 Å, 4.59 Å, 3.77 Å, 89.4 °, 55.2 ° and 34.7 °). Because the sample had not been analysed by XRPD prior to this study it was not known whether it was monophasic or comprised of a mixture of forms. For this reason, the diffraction patterns were recorded from the same crystal, by tilting with respect to the electron beam, as this avoided the possibility of having diffraction patterns from different crystal phases (this was not important in the previous examples as the samples were known to be monophasic from XRPD analysis).

Attempts were made to index the two diffraction patterns against the 11 scyllo-inositol crystal structures that were generated by CSP, using tolerances of d +/- 5 % and θ +/- 3 °. After numerical matching and visual comparison of experimental and simulated patterns, there were two possible zone axis matches for Pattern a, and four possible zone axis matches for Pattern b (sets of symmetry equivalent zone axes were counted as one match) from these 11 structures. These matches are listed in Table 7.9.

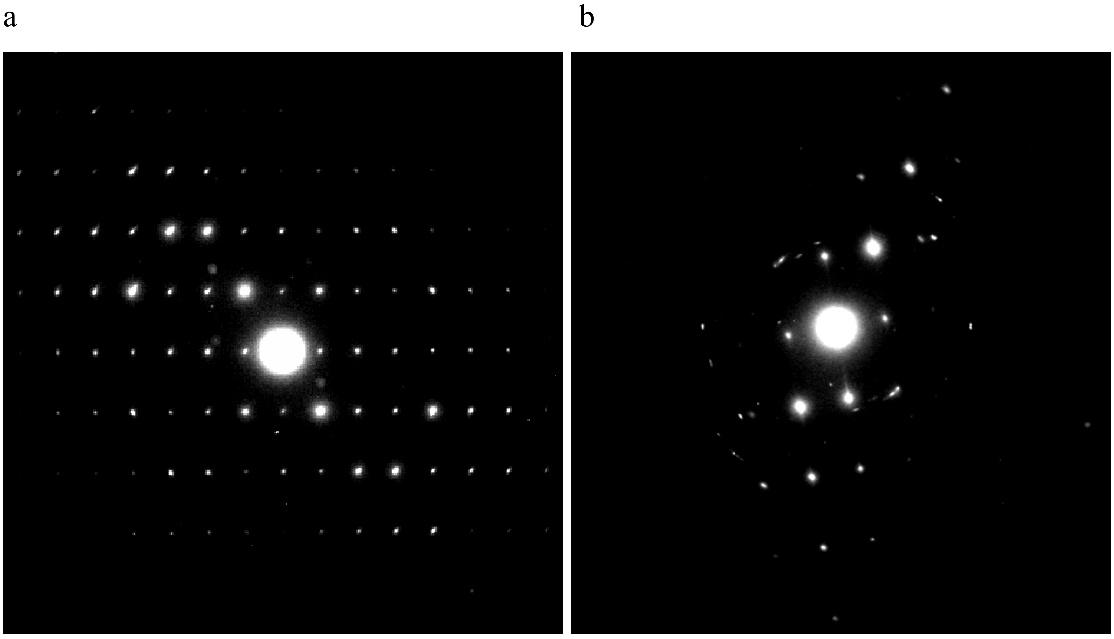

Figure 7.7 Electron diffraction patterns from a crystal of scyllo-inositol.

Table 7.9 Zone axes of the 11 scyllo-inositol CSP structures that could be matched to the diffraction patterns of scyllo-inositol shown in Figure 7.7.

Pattern	CSP Structure	Zone Axis	D-spacings and Interplanar Angles					
			d_1 / Å	d_2 / Å	d_3 / Å	θ_1 / °	θ_2 / °	θ_3 / °
a	S1	<100>	10.314	6.437	5.460	90.0	58.0	32.0
a	S10	<001>	10.210	6.513	5.491	90.0	57.5	32.5
b	S1	<001>	6.437	4.516	3.697	90.0	54.9	35.1
b	S1	<201>	6.437	4.483	3.679	90.0	55.1	34.9
b	S10	<101>	6.513	4.522	3.714	90.0	55.2	34.8
b	S10	<10-1>	6.513	4.453	3.676	90.0	55.6	34.4

On the basis of these results, it was possible to discount a majority of the predicted scyllo-inositol crystal structures. It was not, however, possible to determine if the experimental sample corresponded to structure S1 or structure S10.

On comparing the two theoretical crystal structures S1 and S10, it was observed that they are structurally related. The packing of scyllo-inositol molecules in the two structures was found to be similar, but the conformation of the molecules themselves is different. In structure S1, two of the hydroxyl groups of each scyllo-inositol molecule point in a different direction than the corresponding groups in structure S10 (Figure 7.8).

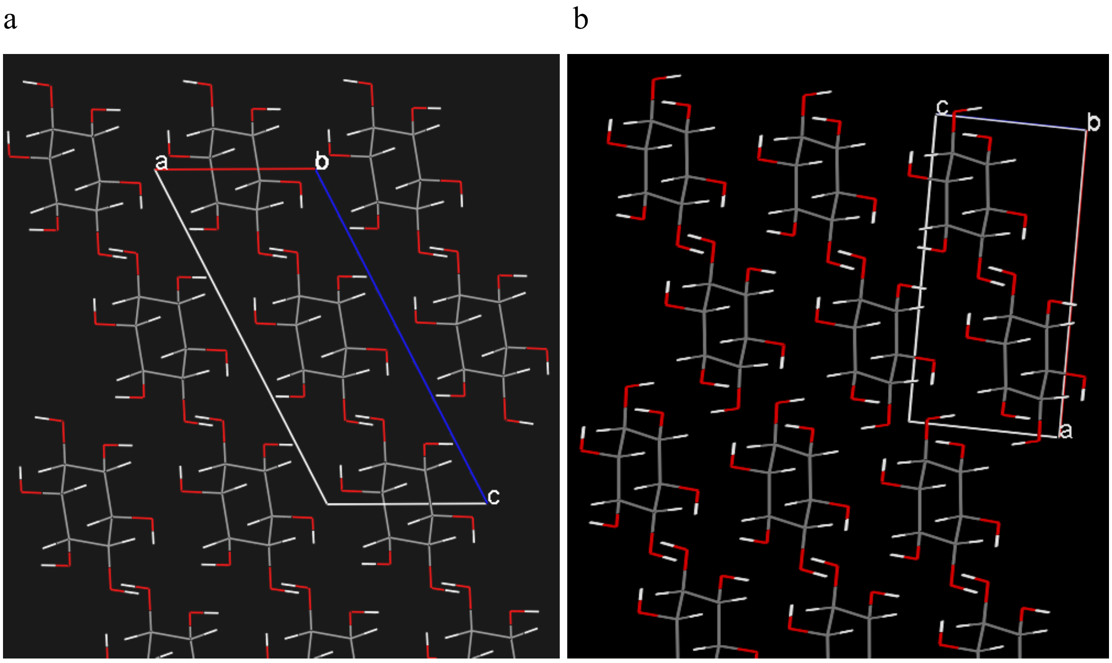

Figure 7.8 A comparison of the molecular packing arrangements in (a) predicted crystal structure S1, and (b) predicted crystal structure S10. In both cases the structures are viewed down the b-axis.

This small difference in hydroxyl group orientations results in the two crystal structures having different space groups, and different systematic absences. The simulated electron diffraction patterns of the <100> zone axis of structure S1 and the equivalent zone axis, <001>, of structure S10 are shown in Figure 7.9. In the structure

S1 pattern there are two sets of absences, odd 0k0 and 00l reflections, whereas in the pattern from structure S10 there is just one set of absences, odd 0k0 reflections.

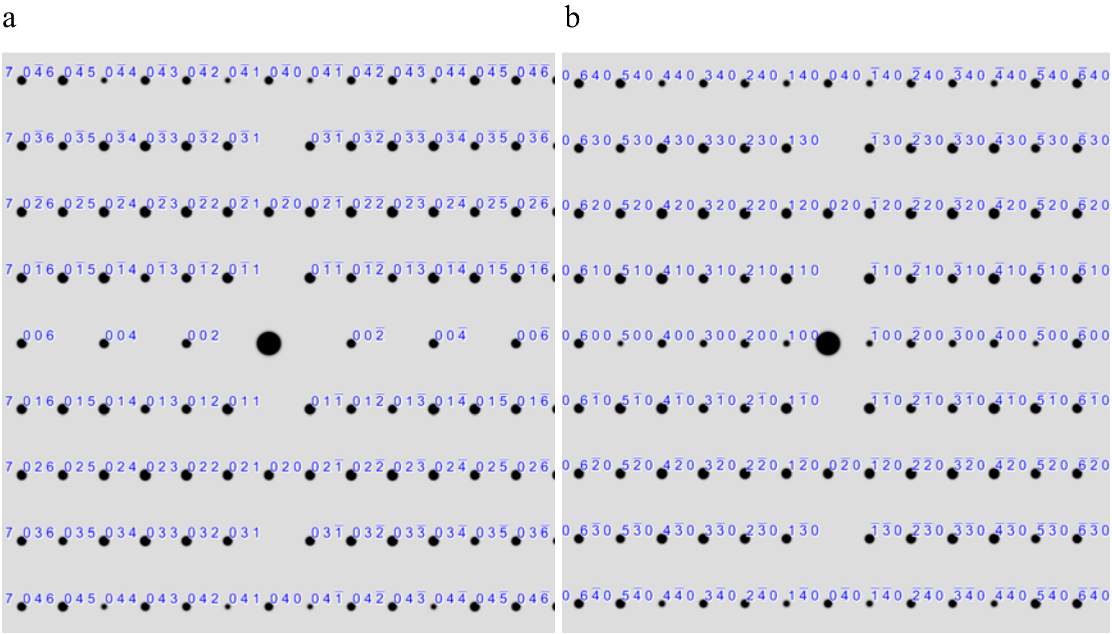

Figure 7.9 A comparison of the simulated electron diffraction patterns of (a) the <100> zone axis of predicted structure S1 of scyllo-inositol, and (b) the <001> zone axis of predicted structure S10 of scyllo-inositol.

Comparing experimental Pattern a (Figure 7.7a) with the two simulated patterns in Figure 7.9, there appears to be better match with the simulated pattern of CSP structure S10 than with that of S1. As described in Section 5.3.5, systematic absences are not always seen in electron diffraction patterns due to multiple scattering, but in Pattern a there is one line of reflections running above and below the central spot which appear to modulate in intensity, suggesting absences, and one line of reflections running left and right of the central spot which do not show modulation.

Two further electron diffraction patterns from the same zone axis as Pattern a were recorded from other crystallites of scyllo-inositol (Figure 7.10). These patterns showed evidence of two sets of absences as expected for CSP structure S1.

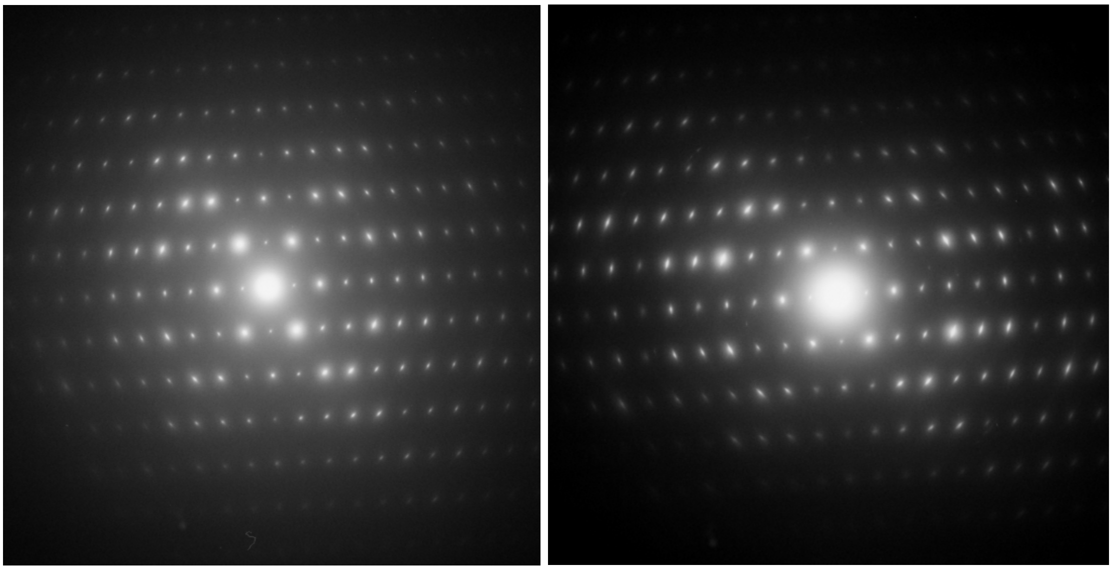

Figure 7.10 Electron diffraction patterns from the same zone axis of scyllo-inositol as Pattern a (Figure 7.7a). The modulations in reflection intensity suggest two sets of absences, odd 0k0 and 00l reflections.

In summary, from the set of 11 lowest energy theoretical crystal structures of scyllo-inositol that were generated by CSP, nine were found to be inconsistent with electron diffraction patterns from a crystal of scyllo-inositol, but it was not possible to distinguish between the remaining two structures (S1 and S10). Structure S1 was identified as being the more likely of these two predicted polymorphs to actually exist as it has a significantly lower calculated lattice energy.

This blind test of the combined TEM/CSP approach to crystal structure determination was found to be a success as predicted structure S1 corresponds to one of the experimentally observed crystal structures of scyllo-inositol (Form I, the triclinic polymorph), and the experimental sample of scyllo-inositol that was used in the study was confirmed to be Form I by XRPD. There are no reported single crystal structures that correspond to predicted structure S10, while Form II of scyllo-inositol corresponds to structure S9.[9]

The danger of over-interpreting the systematic absences in electron diffraction patterns is illustrated by the three diffraction patterns in Figure 7.11. This series of patterns was obtained from the same scyllo-inositol Form I crystal by making slight changes to the orientation of the crystal with respect to the electron beam. All three correspond to the <110> zone axis in which odd 00l reflections should be systematically absent. Depending on the exact tilt conditions, modulation in the intensities of the 00l reflections (in the row to the left and right of the main spot) is either extremely clear (Figure 7.11a), or almost not evident at all (Figure 7.11c).

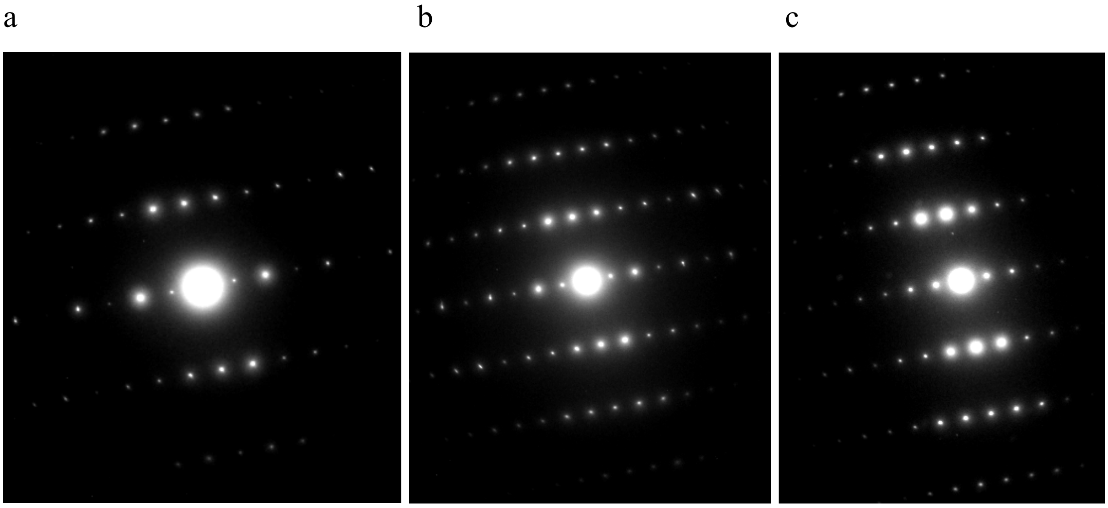

Figure 7.11 Three electron diffraction patterns from the same crystal of Form I of scyllo-inositol recorded at slightly different tilt angles around the <110> zone axis.

Several zone axis electron diffraction patterns that were obtained from crystals of Form I of scyllo-inositol could not be indexed to predicted crystal structure S1 (or S10) using tolerances of d +/- 5 % and θ +/- 3 °. This was found to be due to differences in the unit cell dimensions of the experimental and predicted crystal structures of Form I of scyllo-inositol, a similar finding to that from the work with paracetamol Form I.

7.2.5 Identification of a New Polymorph of Theophylline

A sample of theophylline prepared by evaporation of a nitromethane solution directly onto a TEM grid on a glass slide was analysed by TEM. A majority of the crystals in this sample were triangular plates of Form II of theophylline as shown in Figure 7.12a. However, while scanning across the sample, a crystal was observed which had a significantly different morphology (Figure 7.12b).

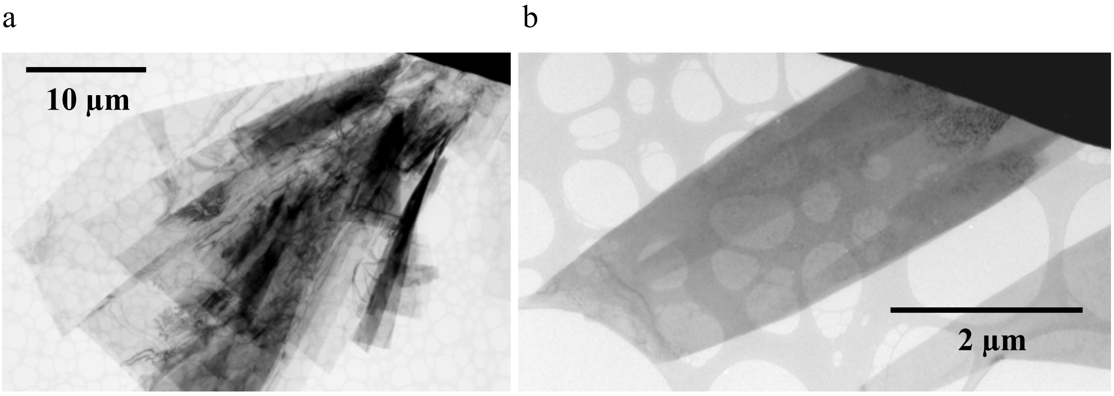

Figure 7.12 TEM analysis of a sample of theophylline prepared by evaporation of a nitromethane solution. (a) A TEM image of overlapping triangular crystals of Form II of theophylline. (b) A crystal from the same sample with a more lath-like morphology.

Two electron diffraction patterns obtained from this particular crystal are shown in Figure 7.13. These diffraction patterns could not be indexed to Form II of theophylline, indicating that the crystal was of a different crystal form to the bulk of the sample. The diffraction data was also inconsistent with Forms I, III, IV and V of theophylline,[16-19] suggesting that a new polymorph of theophylline may have been obtained.

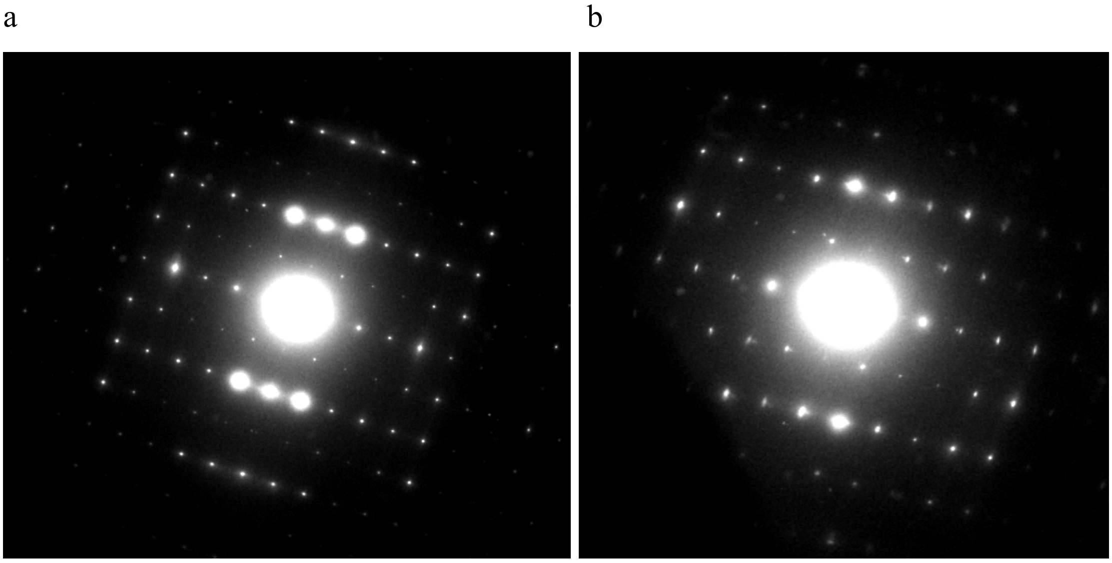

Figure 7.13 Electron diffraction patterns obtained from the crystal of theophylline shown in Figure 7.12b.

In order to determine the crystal structure of this new phase, the two diffraction patterns were indexed against the set of predicted crystal structures that was described in Section 7.2.3. All 60 of the predicted theophylline structures that had a lattice energy within 10 kJ.mol^{-1} of the global minimum were included, and tolerances of d +/- 5 % and θ +/- 3 ° were used.

After numerical matching and visual comparison of experimental and simulated patterns, the only CSP structure to which both diffraction patterns could be indexed was #3 (Orthorhombic, Pbca). The matching experimental and calculated d-spacings and interplanar angles are listed in Table 7.10. Overlays of experimental and simulated diffraction patterns are shown in Figure 7.14. There is a good agreement in both the positions and intensities of reflections. This result confirmed that the crystal structure of the new polymorph of theophylline had been determined.

Table 7.10 Comparison of observed d-spacings and interplanar angles for the diffraction patterns shown in Figure 7.13, indexed as the <101> and <121> zone axes, and the corresponding values for structure #3.

Diffraction pattern	D-spacings and Interplanar Angles					
	d_1 / Å	d_2 / Å	d_3 / Å	θ_1 / °	θ_2 / °	θ_3 / °
Observed pattern a	9.39	6.92	5.59	89.7	53.8	36.6
<101> zone axis of structure #3	8.961	6.892	5.463	90.0	52.4	37.6
Observed pattern b	8.96	5.97	5.41	80.4	62.8	36.2
<121> zone axis of structure #3	8.961	6.069	5.463	80.5	62.6	37.0

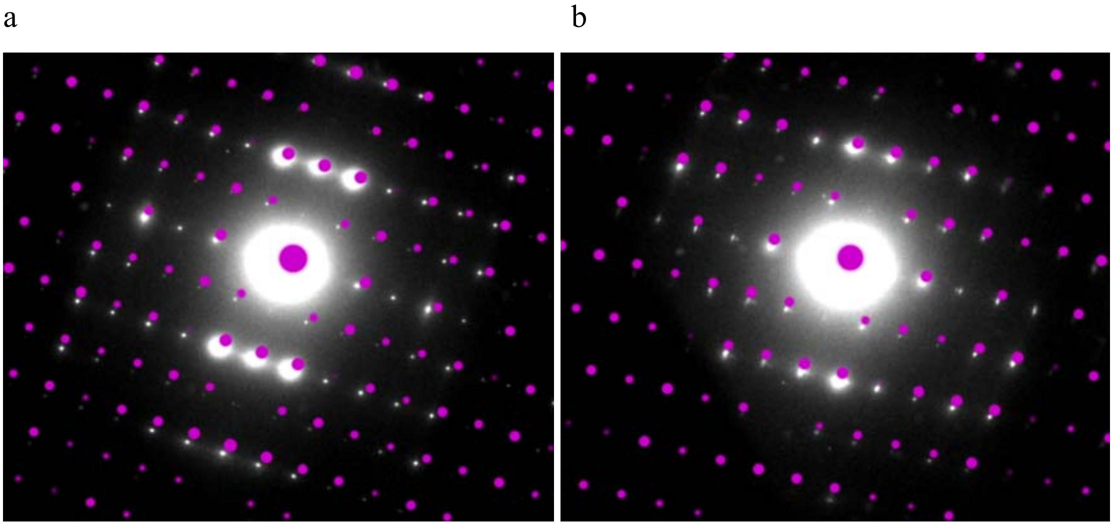

Figure 7.14 Overlay of experimental and simulated electron diffraction patterns from a new polymorph of theophylline. (a) Experimental <101> zone axis electron diffraction pattern with a simulated <101> zone axis pattern of predicted structure #3 overlaid in purple. (b) Experimental <121> zone axis electron diffraction pattern with a simulated <121> zone axis pattern of predicted structure #3 overlaid in purple.

The molecular packing arrangement in the crystal structure of the new polymorph of theophylline is shown in Figure 7.15. Theophylline molecules form hydrogen bonded chains which stack to form sheets, as in Form II of theophylline. The way that the sheets pack together is different in Form II and the new theophylline polymorph.

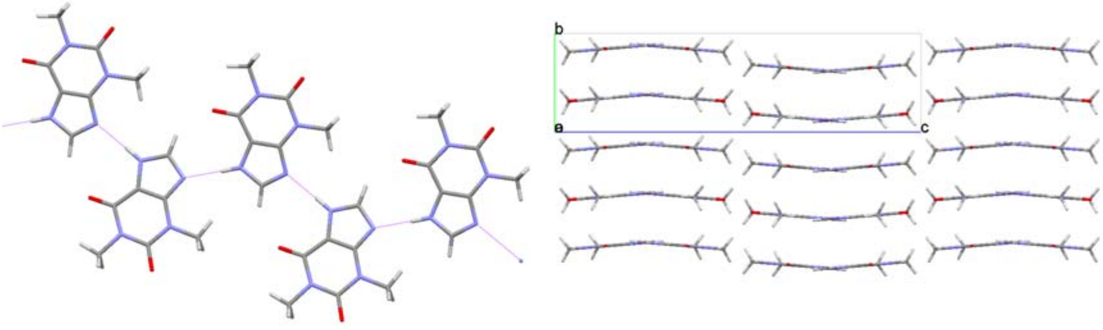

Figure 7.15 The molecular packing arrangement in predicted theophylline crystal structure #3.

During further TEM analysis, a second crystal of the new polymorph of theophylline was identified, but it is estimated that less than one in every hundred crystals in the sample was of this phase. The sample was also analysed by XRPD (Figure 7.16). The resulting trace matched that of Form II of theophylline (taking into account preferred orientation due to the plate-like crystal morphology), and there was no evidence of the presence of the new polymorph of theophylline. If this sample had been analysed by XRPD only, the new polymorph would not have been detected. This is a significant finding given the importance of identifying all crystal forms of an API during drug development in the pharmaceutical industry.

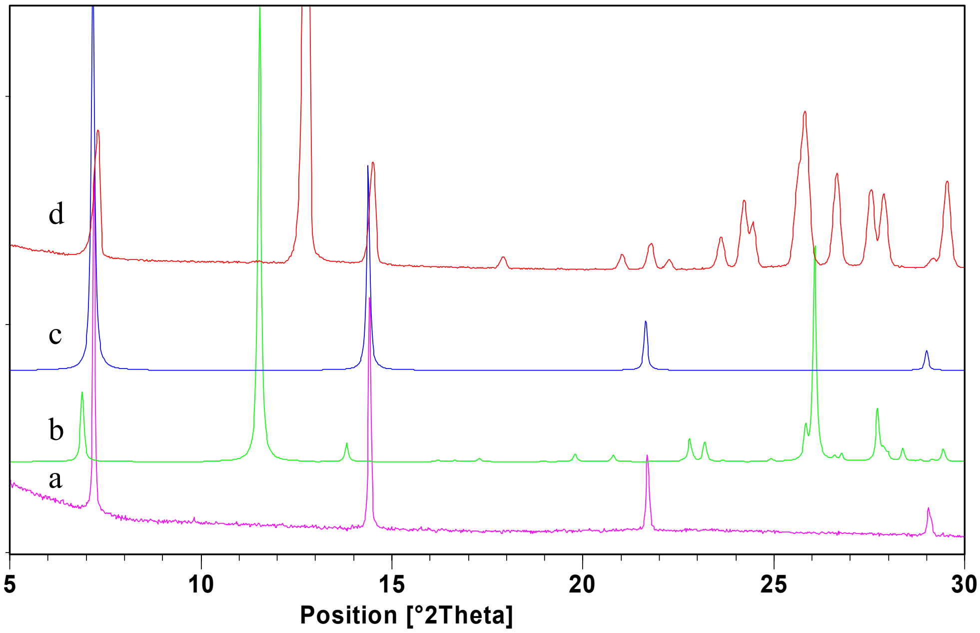

Figure 7.16 XRPD analysis of a sample of theophylline, prepared by evaporation of a nitromethane solution, which was found to contain crystals of a new polymorph of theophylline by TEM. (a) XRPD trace of a sample of theophylline, prepared by evaporation of a nitromethane solution, which was found to contain crystals of a new polymorph of theophylline by TEM. (b) Simulated XRPD trace of predicted theophylline crystal structure #3. (c) Simulated XRPD trace of Form II of theophylline (CSD ref BAPLOT01,[14] calculated to take into account preferred orientation due to the plate-like crystal morphology of the sample). (d) Reference trace of form II of theophylline.

7.3 Conclusions

A novel method for solving crystal structures through a combined TEM and CSP approach was successfully developed.

This approach was used to identify a new polymorph of theophylline that was present as a trace amount in a mixture with Form II of theophylline. The electron diffraction patterns that were used for crystal structure determination were obtained from a single crystallite with dimensions of 5 μm x 2 μm x < 0.3 μm and an approximate mass of 3 pg. Crystal structure solution would not have been possible for a crystal of this size using X-ray diffraction, even with a synchotron source. In fact, it is highly unlikely that this new crystal phase would have been observed at all with techniques traditionally used for pharmaceutical analysis.

The approach may not be applicable to all samples. If there are large differences between experimental and predicted crystal structures it may be impossible to identify the correct predicted structure. It is also possible that the experimentally observed structure is not generated at all by CSP.[20] CSP methodologies do not usually include all 230 space groups, and often focus on generating structures with just one molecule in the asymmetric unit. In addition, the chances of a crystal structure being predicted by CSP become lower as molecule size and flexibility increase.[21] The TEM/CSP approach may also fail if only diffraction patterns containing reflections corresponding to crystal planes with small d-spacings are used in the analysis.

The methods and potentials used in CSP work are constantly improving. As predictions get more accurate, and it is possible to handle more flexible molecules, the combined TEM/CSP approach to crystal structure determination will only become more widely applicable.

7.4 Further Work

Attempts should be made to prepare a pure phase of the new polymorph of theophylline through an investigation of conditions which promote nucleation of this form rather than Form II.

Precession electron diffraction is a method for generating diffraction patterns with more accurate reflection intensities.[22] This technique should be applied to analysis of samples of scyllo-inositol to generate unambiguous evidence for the existence of predicted crystal form #10.

7.5 References

1. Kolb U., Gorelik T. E., Mugnaioli E., Stewart A. Structural Characterization of Organics Using Manual and Automated Electron Diffraction. *Polym. Rev.*, 2010, 50(3), 385-409.

2. Weirich T. E., Ramlau R., Simon A., Hovmoeller S., Zou X. A crystal structure determined with 0.02 Å accuracy by electron microscopy. *Nature*, 1996, 382(6587), 144-146.

3. Thomas J. M., Midgley P. A. High-resolution transmission electron microscopy: the ultimate nanoanalytical technique. *Chem. Commun.*, 2004, (11), 1253-1267.

4. Dorset D. L. Electron crystallography - accomplishments and challenges. *Acta Crystallogr., Sect. A: Found. Crystallogr.*, 1998, A54(6, Pt. 1), 750-757.

5. Williams D. B., Carter C. B. Transmission electron microscopy. A textbook for materials science. New York: Plenum Press, 1996, p.

6. Price S. L. Computed Crystal Energy Landscapes for Understanding and Predicting Organic Crystal Structures and Polymorphism. *Acc. Chem. Res.*, 2009, 42(1), 117-126.

7. Woodley S. M., Catlow R. Crystal structure prediction from first principles. *Nat. Mater.*, 2008, 7(12), 937-946.

8. Hulme A. T., Price S. L., Tocher D. A. A New Polymorph of 5-Fluorouracil Found Following Computational Crystal Structure Predictions. *J. Am. Chem. Soc.*, 2005, 127(4), 1116-1117.

9. Day G. M., Van de Streek J., Bonnet A., Burley J. C., Jones W., Motherwell W. D. S. Polymorphism of Scyllo-Inositol: Joining Crystal Structure Prediction with Experiment to Elucidate the Structures of Two Polymorphs. *Cryst. Growth Des.*, 2006, 6(10), 2301-2307.

10. Salager E., Day G. M., Stein R. S., Pickard C. J., Elena B., Emsley L. Powder Crystallography by Combined Crystal Structure Prediction and High-Resolution 1H Solid-State NMR Spectroscopy. *J. Am. Chem. Soc.*, 2010, 132(8), 2564-2566.

11. Beyer T., Day G. M., Price S. L. The Prediction, Morphology, and Mechanical Properties of the Polymorphs of Paracetamol. *J. Am. Chem. Soc.*, 2001, 123(21), 5086-5094.

12. Drebushchak T. N., Boldyreva E. V. Variable temperature (100-360 K) single-crystal x-ray diffraction study of the orthorhombic polymorph of paracetamol (p-hydroxyacetanilide). *Z. Kristallogr.*, 2004, 219(8), 506-512.

13. Haisa M., Kashino S., Kawai R., Maeda H. The monoclinic form of p-hydroxyacetanilide. *Acta Crystallogr., Sect. B*, 1976, B32(4), 1283-1285.

14. Ebisuzaki Y., Boyle P. D., Smith J. A. Methylxanthines. I. Anhydrous theophylline. *Acta Crystallogr., Sect. C: Cryst. Struct. Commun.*, 1997, C53(6), 777-779.

15. McLaurin J. 2007. Method of preventing, treating and diagnosing disorders of protein aggregation. Application: US: (Can.). 1-33

16. Suzuki E., Shimomura K., Sekiguchi K. Thermochemical study of theophylline and its hydrate. *Chem. and Pharm. Bull.*, 1989, 37(2), 493-497.

17. Matsuo K., Matsuoka M. Solid-State Polymorphic Transition of Theophylline Anhydrate and Humidity Effect. *Cryst. Growth Des.*, 2007, 7(2), 411-415.

18. Seton L., Khamar D., Bradshaw I. J., Hutcheon G. A. Solid State Forms of Theophylline: Presenting a New Anhydrous Polymorph. *Cryst. Growth Des.*, 2010, 10(9), 3879-3886.

19. Roy C., Vega-Gonzalez A., Subra-Paternault P. Theophylline formulation by supercritical antisolvents. *Int. J. Pharm.*, 2007, 343(1-2), 79-89.

20. Day G. M., Cooper T. G., Cruz-Cabeza A. J., Hejczyk K. E., Ammon H. L., Boerrigter S. X. M., Tan J. S., Della Valle R. G., Venuti E., Jose J., Gadre S. R., Desiraju G. R., Thakur T. S., van Eijck B. P., Facelli J. C., Bazterra V. E., Ferraro M. B., Hofmann D. W. M., Neumann M. A., Leusen F. J. J., Kendrick J., Price S. L., Misquitta A. J., Karamertzanis P. G., Welch G. W. A., Scheraga H. A., Arnautova Y. A., Schmidt M. U., van de Streek J., Wolf A. K., Schweizer B. Significant progress in predicting the crystal structures of small organic molecules - a report on the fourth blind test. *Acta Crystallogr., Sect. B: Struct. Sci.*, 2009, B65(2), 107-125.

21. Day G. M., Cooper T. G. Crystal packing predictions of the alpha-amino acids: methods assessment and structural observations. *CrystEngComm*, 2010, 12(8), 2443-2453.

22. Vincent R., Midgley P. A. Double conical beam-rocking system for measurement of integrated electron diffraction intensities. *Ultramicroscopy*, 1994, 53(3), 271-282.

8 Characterisation of Sub-Micron Sized Particles of Pharmaceutical Materials by TEM

8.1 Introduction

Reducing the crystal size of a drug compound to a sub-micron range has been demonstrated to be a means of significantly improving solubility and bioavailability through an increase in sample surface area.[1-3] Sub-micron sized particles of pharmaceutical materials are prepared by techniques such as milling, grinding, homogenisation and precipitation.[2]

TEM is routinely used for studying inorganic nanoparticles.[5-7] Here, TEM was applied to the analysis of sub-micron sized crystals of theophylline that were generated by ball milling, and to monitoring changes that occurred both during and after grinding. The suitability of TEM for the characterisation of sub-micron sized pharmaceutical samples was assessed.

AFM is a technique which has previously been used for analysing sub-micron sized particles of pharmaceutical materials.[8] AFM was used in this study to compliment the information obtained from TEM analysis.

8.2 Results and Discussion

A 180 mg portion of a sample of Form II of theophylline was dry ground in a ball mill for 30 minutes, and the non-ground and ground specimens were analysed by TEM. A TEM image of the pre-grinding sample showed a triangular plate of theophylline with a length of 10 μm (Figure 8.1a). The top part of the triangle had undergone fracturing. The post-grinding sample consisted of agglomerates of nano-sized particulates (Figure 8.1b).

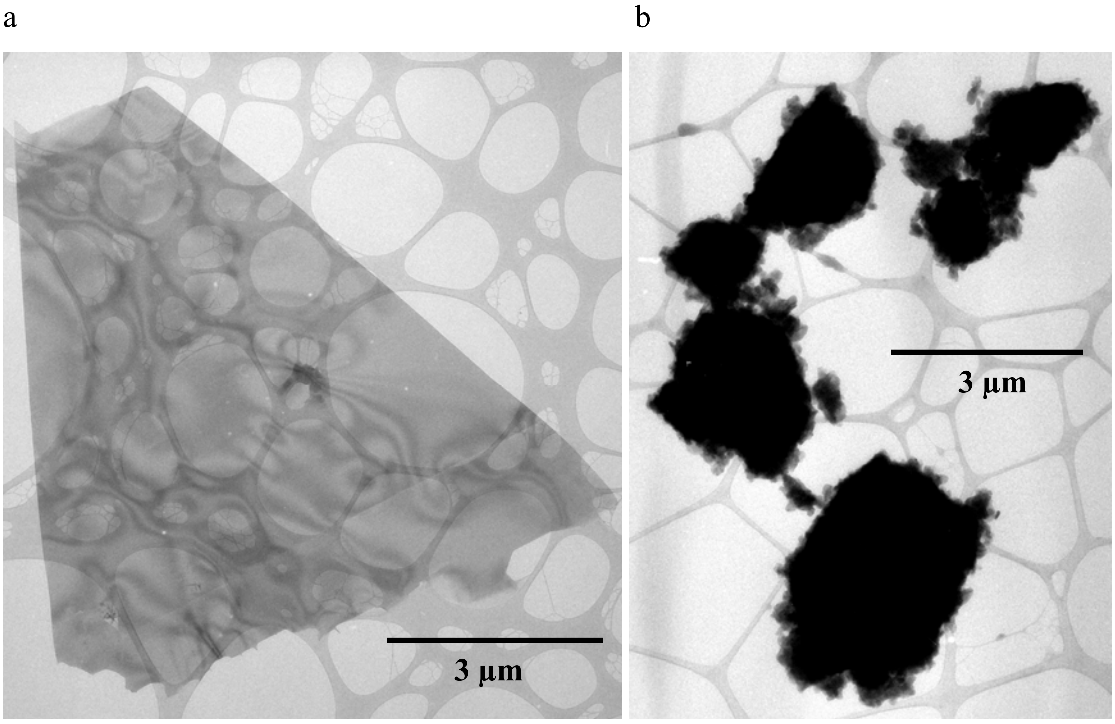

Figure 8.1 TEM images of a sample of Form II of theophylline before and after grinding in a ball mill. (a) A triangular crystal of Form II of theophylline prepared by cooling a saturated solution of theophylline in ethyl acetate to induce crystallisation. (b) Crystallites of Form II of theophylline after dry grinding in a ball mill for 30 minutes.

The dry ground sample was then re-ground for 20 minutes with the addition of 20 µl of nitromethane. It was evident from TEM analysis that the particle size of the resulting sample was several times greater than that of the dry ground sample (Figure 8.2). An image of the dry ground sample (Figure 8.2a) showed agglomerated crystallites with an approximate average particle diameter of 100 nm. The rounded morphology of the individual nano-sized crystallites could be discerned. After liquid assisted grinding, the particles still had a rounded morphology, but the average particle diameter had increased to approximately 400 nm. Bend contours could be seen, and were wider and rougher than those in solution grown crystals, indicating that there was a high defect content in the crystals after liquid assisted grinding (Figure 8.2b). Dry ground crystals were too small for bend contours to be seen.

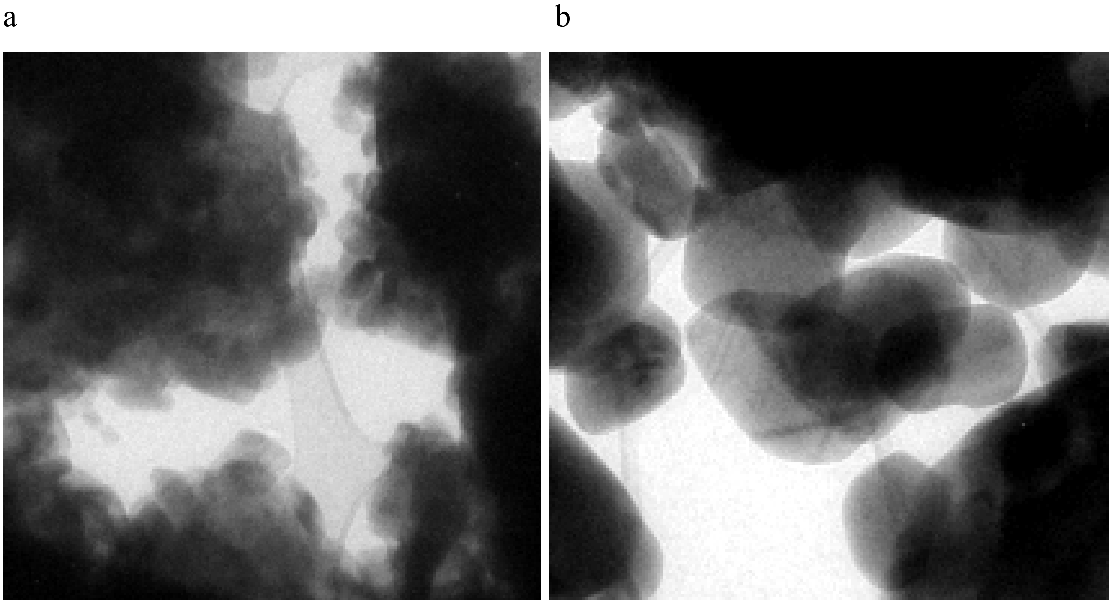

Figure 8.2 Representative TEM images of Form II of theophylline after dry grinding and liquid assisted grinding with nitromethane. Each image shows a 2 µm x 2 µm region of sample. (a) Sample prepared by dry grinding theophylline for 30 minutes. (b) The same sample after grinding again for 20 minutes in the presence of 20 µl of nitromethane.

The dry grinding and liquid assisted grinding samples of theophylline were also analysed by PLM, SEM and AFM to compare the images obtained by these techniques with those from TEM. PLM images of the two samples are shown in Figure 8.3. Agglomerates were evident in the dry grinding sample, but it was difficult to discern individual crystallites. After liquid assisted grinding, the sample appeared to be less agglomerated, and individual crystallites could be seen. Though slight differences between the two samples could be observed by PLM, the higher magnification TEM images were more informative.

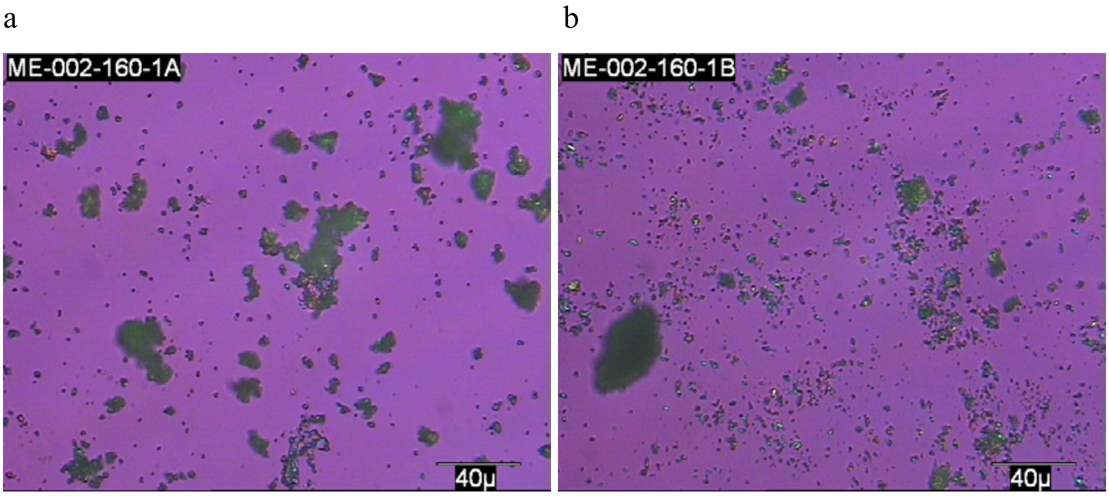

Figure 8.3 Representative PLM images of Form II of theophylline after dry grinding and liquid assisted grinding with nitromethane. (a) Sample prepared by dry grinding theophylline for 30 minutes. (b) The same sample after grinding again for 20 minutes in the presence of 20 µl of nitromethane.

SEM images of particle surfaces in the dry grinding and liquid assisted grinding samples of theophylline are shown in Figure 8.4.

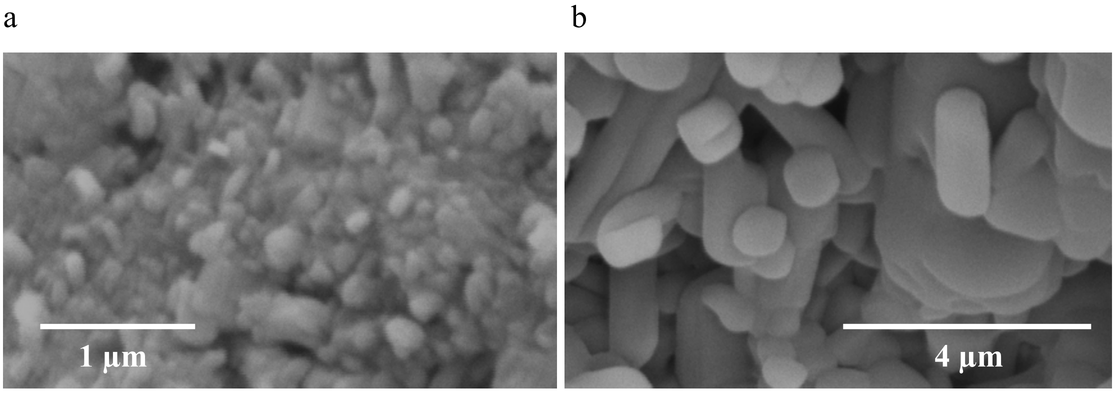

Figure 8.4 Representative SEM images of Form II of theophylline after dry grinding and liquid assisted grinding with nitromethane (recorded on a JEOL-5800LV instrument). (a) Sample prepared by dry grinding theophylline for 30 minutes. (b) The same sample after grinding again for 20 minutes in the presence of 20 µl of nitromethane.

Particle sizes were seen to be between 50 and 200 nm for the dry grinding sample and between 300 nm and 1.5 μm for the liquid assisted grinding sample, with a rounded plate morphology evident in the latter. The necessity of sputter coating the samples with platinum prior to analysis (to reduce charging) will have introduced a significant error in particle size measurements for the smaller particles from dry grinding as the platinum coating is approximately 5-10 nm thick, but the observations are consistent with those obtained by TEM analysis.

Characterisation of the ground materials by AFM was not straightforward. The small crystallites tended to move around during analysis, or stick to the AFM tip. Also, AFM is better suited to studying relatively flat surfaces, rather than the rounded particles analysed here. AFM images are shown in Figure 8.5. Height differences across the images are shown through a colour scale with higher regions appearing lighter. It is apparent that the crystallites of theophylline from dry grinding are approximately spherical with diameters of up to 200 nm. The particle from liquid assisted grinding shown in Figure 8.5b is significantly larger, over 1 μm across, with a more flattened shape. It is evident that the particle is comprised of four different crystalline domains that have intergrown. Note that as the AFM tip moved across the edge of the particle, the point of the tip was no longer in contact with any surface, and the side of the AFM tip dragged down the crystal edge until the point of the tip made contact with the mica sample support. This resulted in a loss of image quality at the edges of the particle.

It was significantly more difficult to image the ground samples by AFM than it was by TEM, but the AFM images do have greater resolution. Similar resolutions were possible in the TEM instrument, but required increased beam flux in order to achieve adequate illumination, and this caused amorphisation of the sample. Even though the edges of particles are not imaged well by AFM (for the reasons described above), particle sizes could be measured more accurately than with TEM, and a better understanding of the 3-dimensional shape of the particles could be obtained. The two techniques gave complimentary information about the theophylline samples, with surface detail revealed by AFM analysis and bulk particle information gained from TEM.

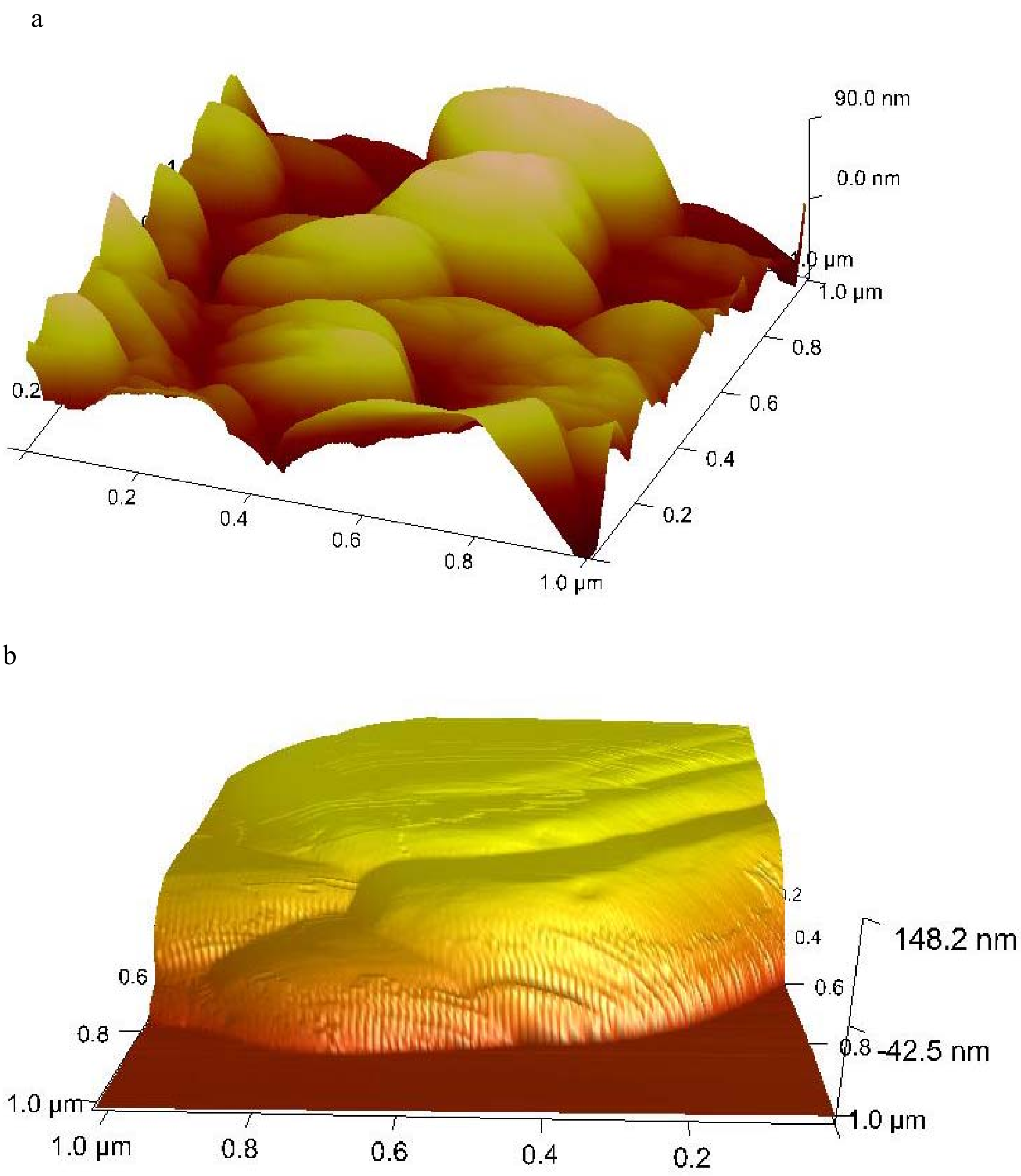

Figure 8.5 Representative AFM height images of Form II of theophylline after dry grinding and liquid assisted grinding with nitromethane. Each image shows a 1 µm x 1 µm region of sample. Higher regions of the sample appear lighter in the images. (a) Sample prepared by dry grinding theophylline for 30 minutes. (b) The same sample after grinding again for 20 minutes in the presence of 20 µl of nitromethane.

A key advantage of using TEM was that diffraction analysis could be performed. It was not possible to obtain diffraction patterns that were suitable for indexing from the dry-grinding sample as the beam intensity that was required to obtain good diffraction patterns from the small crystallites in this sample caused rapid amorphisation. However, the fact that diffraction spots were observed at all did indicate that some crystalline material was present. The diffraction pattern in Figure 8.6a shows reflections from several crystallites and a halo consistent with the presence of amorphous solid. It is not clear if the amorphous material was generated during grinding or during TEM analysis, though it is likely to the former as beam exposure was kept to a minimum (< 5 minutes). Phase identification was possible with the larger crystallites from liquid assisted grinding. For example, the diffraction pattern shown in Figure 8.6b was indexed to the <121> zone axis Form II of theophylline.

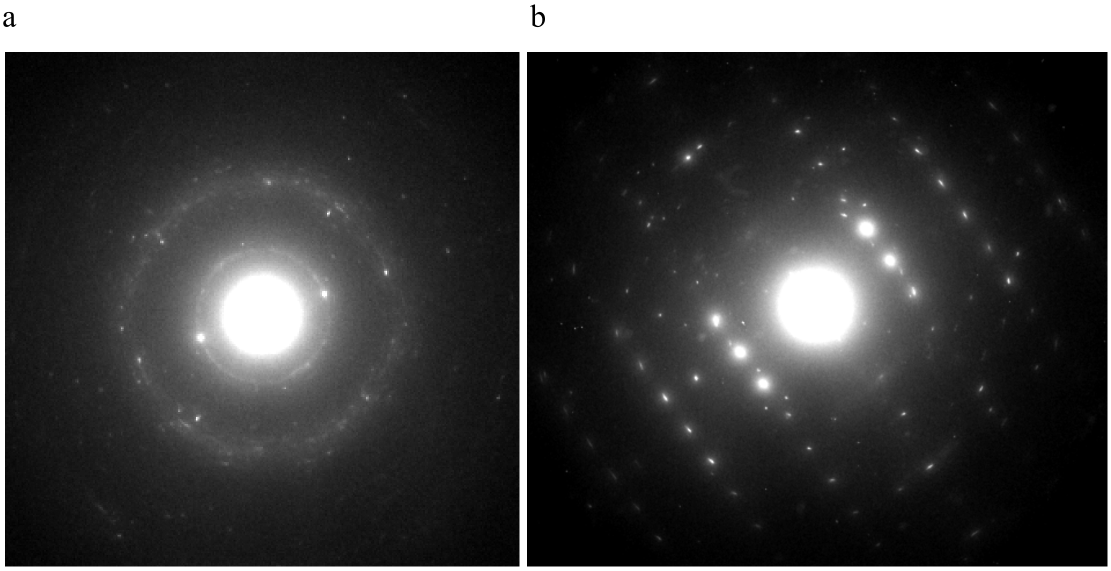

Figure 8.6 TEM electron diffraction patterns from Form II of theophylline after dry grinding and liquid assisted grinding with nitromethane. (a) A diffraction pattern from a sample prepared by dry grinding theophylline for 30 minutes. (b) A diffraction pattern from the same sample after grinding again for 20 minutes in the presence of 20 µl of nitromethane. This pattern was indexed to the <121> zone axis of Form II of theophylline.

At first glance, the observation that the size of the theophylline particles increased during the liquid assisted grinding experiment seems to be counter-intuitive, as grinding is thought to be a destructive process. The role of the small amount of solvent that is added during liquid assisted grinding has been reported to be one of enhancement of molecular mobility,[11] and while it has been shown previously that samples display a reduced tendency to amorphisation during liquid assisted grinding in comparison to dry grinding,[12] the observation of crystal growth during liquid assisted grinding was unexpected. This finding suggests that solution phase processes such as dissolution and re-crystallisation may have been occurring during the liquid assisted grinding experiments. While the 20 μl of nitromethane used in the above experiment was less than an equimolar ratio with respect to theophylline (0.37 equivalents), and also over 1000 times less than would be required to completely dissolve all of the solid used in the experiment, it was calculated that this volume would be enough to cover each of the theophylline particles present in the grinding vial with approximately 25 layers of solvent molecules (assuming that the average diameter of the theophylline particles was 100 nm).

Crystal growth during liquid assisted grinding was investigated further by varying the duration of the liquid assisted grinding phase. Two samples of Form II of theophylline were prepared by dry grinding. This grinding was followed by liquid assisted grinding with 20 μl of nitromethane for 5 minutes and 1 hour respectively. The TEM image in Figure 8.7a shows particles of theophylline that were ground with nitromethane for 5 minutes. These crystals were smaller than those obtained by grinding with nitromethane for 1 hour, shown in Figure 8.7b. The average particle diameter of the 1 hour liquid assisted grinding sample was approximately 1 μm, larger that of the 20 minute liquid assisted grinding sample shown in Figure 8.2b. This suggested that crystal growth had occurred throughout the hour of liquid assisted grinding. It is thought that eventually a steady particle size distribution would be obtained, where crystal growth is offset by crystal fracture and cleavage due to impacts in the ball mill.

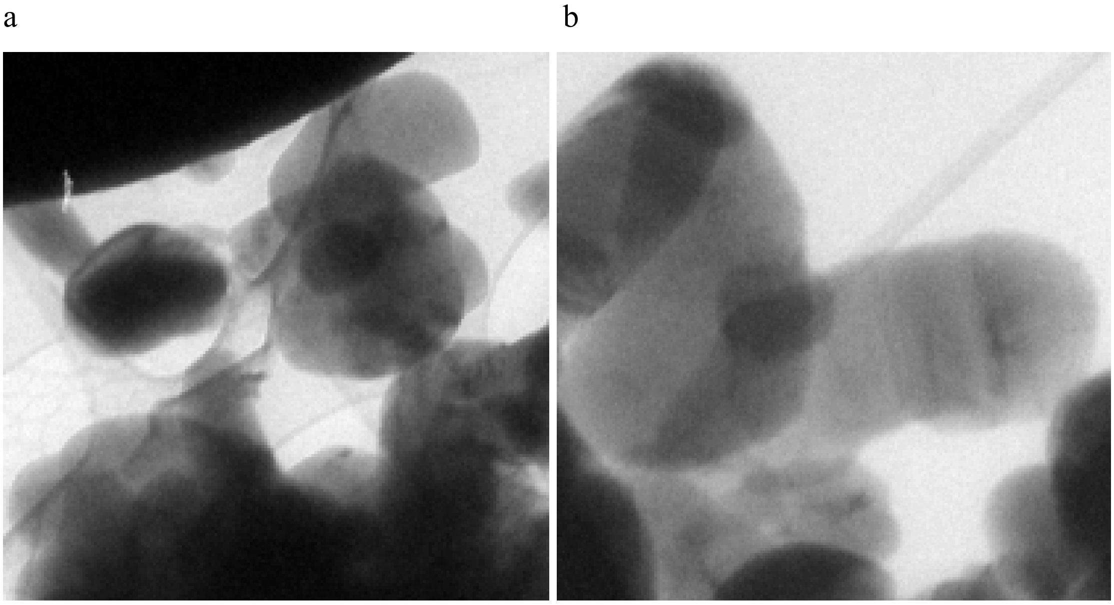

Figure 8.7 TEM images of samples of Form II of theophylline that were initially dry ground for 30 minutes and then ground again with nitromethane for different durations. Each image shows a 2 µm x 2 µm region of sample. (a) Sample of theophylline prepared by dry grinding for 30 minutes followed by grinding with nitromethane for 5 minutes. (b) Sample of theophylline prepared by dry grinding for 30 minutes followed by grinding with nitromethane for 1 hour.

The solvent used in the liquid assisted grinding part of the experiment was then varied to determine the effect of solvent solubility on particle size. Experiments were performed with methanol and cyclohexane, solvents in which the solubility of theophylline was found to be 5 $mg.ml^{-1}$ and << 1 $mg.ml^{-1}$ respectively. Again, theophylline was first dry ground for 30 minutes, and then subjected to liquid assisted grinding for 20 minutes. A TEM image of the cyclohexane sample is shown in Figure 8.8a. There were two different crystal morphologies in the sample, with some particles being lath shaped and others more rounded. The particle size was between 100 and 400 µm, greater than that in the dry ground samples. The methanol sample contained lath shaped particles, and the particle size was larger than in the cyclohexane sample, with some particles having lengths of over 2 µm (Figure 8.8b).

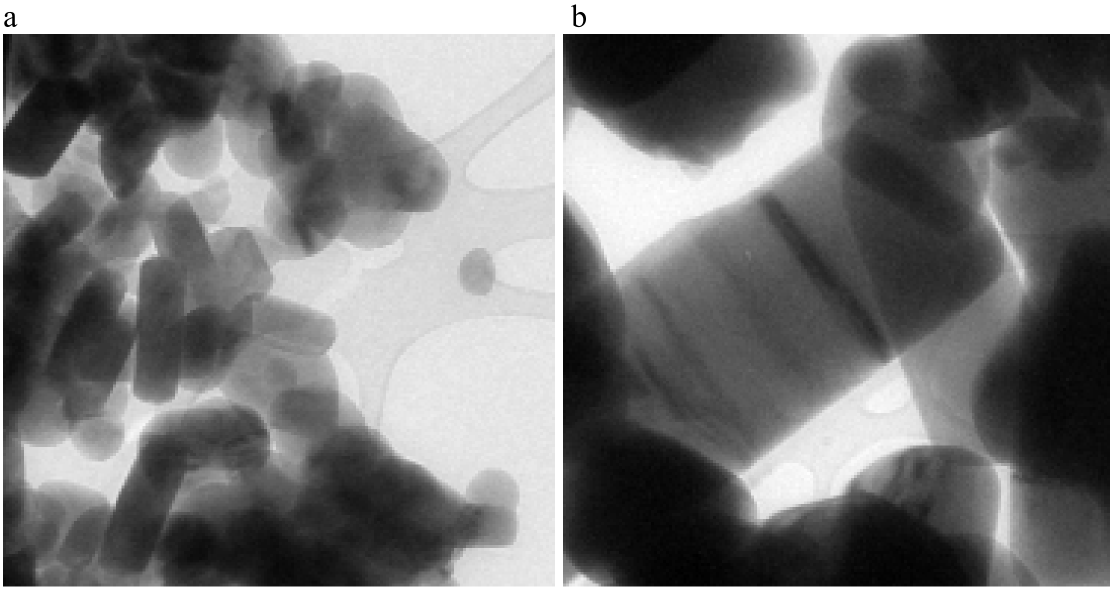

Figure 8.8 TEM images of samples of Form II of theophylline that were initially dry ground for 30 minutes and then ground again with different solvents for different 20 minutes. Each image shows a 2 μm x 2 μm region of sample. (a) Sample of theophylline prepared by dry grinding for 30 minutes followed by grinding with cyclohexane for 20 minutes. (b) Sample of theophylline prepared by dry grinding for 30 minutes followed by grinding with methanol for 20 minutes.

The relative particle size increase that was observed during 20 minutes of liquid assisted grinding with nitromethane, cyclohexane and methanol was found to reflect the solubility of theophylline in these solvents: methanol < nitromethane < cyclohexane. This trend again suggested that solution phase processes such as dissolution and re-crystallisation may be occurring during liquid assisted grinding experiments.

A dry-ground sample of Form II of theophylline was also stored under ambient conditions for 5 days, after which it was analysed by TEM. During storage, there was a change in particle shape to a lath morphology, and the particle size increased significantly to between 200 μm and 500 μm (Figure 8.9a).

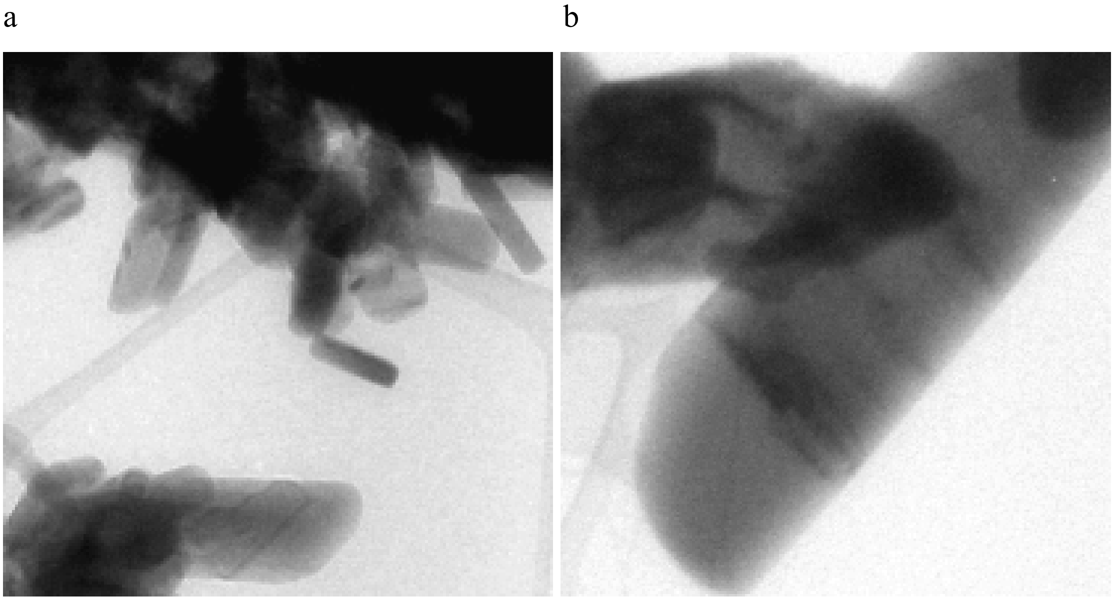

Figure 8.9 TEM images of samples of Form II of theophylline that were initially dry ground for 30 minutes and then stored under different conditions for 5 days. Each image shows a 2 µm x 2 µm region of sample. (a) Sample of theophylline prepared by dry grinding for 30 minutes followed by storage under ambient conditions for 5 days. (b) Sample of theophylline prepared by dry grinding for 30 minutes followed by storage in a nitromethane atmosphere for 5 days.

In a separate experiment, a dry-ground sample of theophylline was stored in a nitromethane atmosphere, yielding rectangular plate-like crystals up to 2 µm in length. The discontinuous nature of bend contours across the crystals indicated the presence of multiple crystal domains and / or the presence of defects (Figure 8.9b).

AFM analysis of the crystals that were stored in a nitromethane atmosphere showed that they had very flat plate faces, representing a large change from the approximately spherical appearance of the dry ground crystals prior to storage (Figure 8.10).

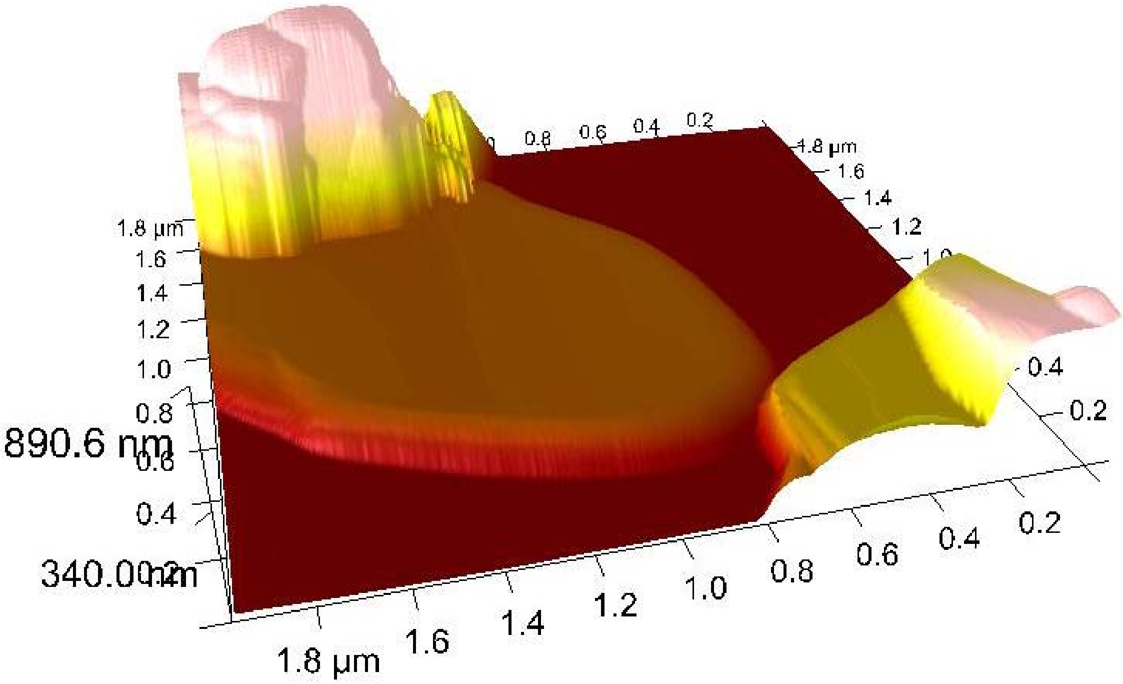

Figure 8.10 Representative AFM height image of Form II of theophylline after dry grinding followed by 5 days of storage in a nitromethane atmosphere. Higher regions of the sample appear lighter in the image.

8.3 Conclusions

TEM is an ideal technique for characterising sub-micron sized particles of pharmaceutical materials, and has clear advantages over other techniques in image detail and phase identification. AFM analysis yielded useful complementary information about the shape and surface of particles.

This work has given an insight into grinding processes. Liquid assisted grinding can cause an increase in the particle size of a sample, and may well involve a solution phase. Dry grinding with theophylline was found to be better method for reducing particle size than wet milling, a result which differs to previous findings with the drug H0-221.[4]

Large changes in particle size and morphology were observed for theophylline crystals in the days following ball milling. This indicates that if milling were to be used as a step in a drug manufacturing process it would be necessary to perform particle size measurements at the same time-point after milling for each batch of material that is prepared in order to ensure uniformity.

8.4 Further Work

This work could be extended by using TEM to investigate cocrystallisation by dry and liquid assisted grinding in a ball mill (and monitor changes in particle size and morphology during this process). A particular advantage of TEM would be the ability to detect small amounts of cocrystal formation in samples where the coformers did not convert in the bulk of the sample, or to detect small amounts of unreacted coformers in samples which did convert. For example, unreacted theophylline has been observed in a sample of Form III of the caffeine:theophylline cocrystal prepared by grinding.

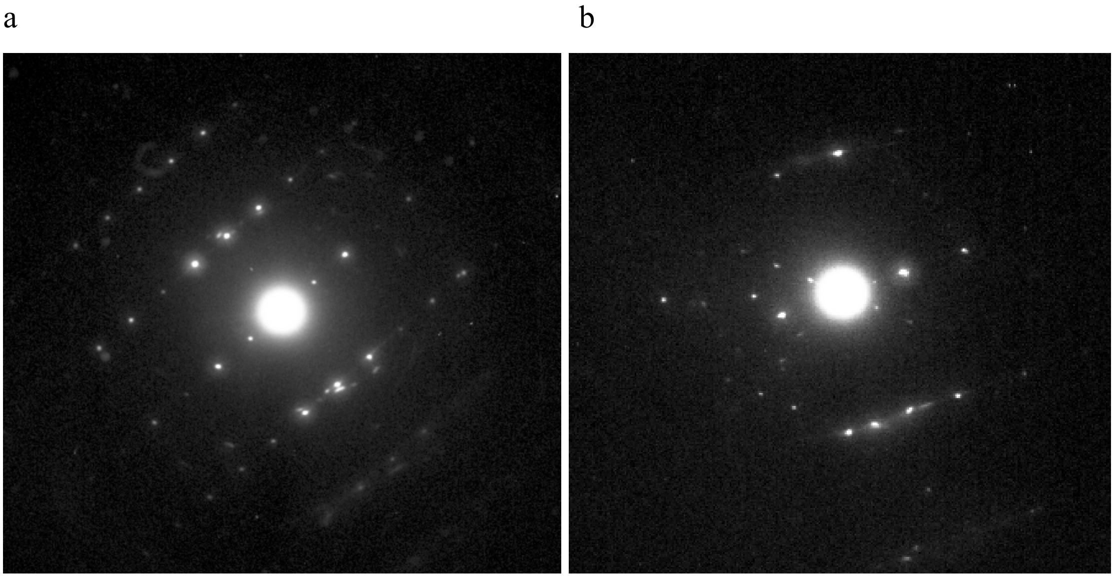

Figure 8.11 Electron diffraction patterns from a sample prepared by grinding equimolar amounts of caffeine and theophylline with nitromethane. (a) <121> zone axis electron diffraction pattern of Form II of theophylline. (b) <142> zone axis electron diffraction pattern of Form II of theophylline.

Two electron diffraction patterns from this sample were indexed to the <121> and <142> zone axes of Form II of theophylline respectively (Figure 8.11). XRPD analysis gave no indication that the sample contained a mixture of phases.

8.5 References

1. Blagden N., de Matas M., Gavan P. T., York P. Crystal engineering of active pharmaceutical ingredients to improve solubility and dissolution rates. *Adv. Drug Delivery Rev.*, 2007, 59(7), 617-630.

2. Merisko-Liversidge E. M., Liversidge G. G. Drug nanoparticles: formulating poorly water-soluble compounds. *Toxicol. Pathol.*, 2008, 36(1), 43-48.

3. Kondo N., Iwao T., Kikuchi M., Shu H., Yamanouchi K., Yokoyama K., Ohyama K., Ogyu S. Pharmacokinetics of a micronized, poorly water-soluble drug, HO-221, in experimental animals. *Biol. Pharm. Bull.*, 1993, 16(8), 796-800.

4. Itoh K., Pongpeerapat A., Tozuka Y., Oguchi T., Yamamoto K. Nanoparticle formation of poorly water-soluble drugs from ternary ground mixtures with PVP and SDS. *Chem. Pharm. Bull.*, 2003, 51(2), 171-174.

5. Williams D. B., Carter C. B. Transmission electron microscopy. A textbook for materials science. New York: Plenum Press, 1996.

6. Tham D., Nam C. Y., Byon K., Kim J., Fischer J. E. Applications of electron microscopy to the characterization of semiconductor nanowires. *Appl. Phys. A: Mater. Sci. Process.*, 2006, 85(3), 227-231.

7. Weirich T. E., Zou X., Ramlau R., Simon A., Cascarano G. L., Giacovazzo C., Hovmoller S. Structures of nanometre-size crystals determined from selected-area electron diffraction data. *Acta Crystallogr., Sect. A: Found. Crystallogr.*, 2000, A56(1), 29-35.

8. Shi H. G., Farber L., Michaels J. N., Dickey A., Thompson K. C., Shelukar S. D., Hurter P. N., Reynolds S. D., Kaufman M. J. Characterization of Crystalline Drug Nanoparticles Using Atomic Force Microscopy and Complementary Techniques. *Pharm. Res.*, 2003, 20(3), 479-484.

9. Binnig G., Quate C. F., Gerber C. Atomic force microscope. *Phys. Rev. Lett.*, 1986, 56(9), 930-933.

10. Binnig G., Gerber C., Stoll E., Albrecht T. R., Quate C. F. Atomic resolution with atomic force microscope. *Europhys. Lett.*, 1987, 3(12), 1281-1286.

11. Friscic T., Jones W. Recent Advances in Understanding the Mechanism of Cocrystal Formation via Grinding. *Cryst. Growth Des.*, 2009, 9(3), 1621-1637.

12. Nguyen K. L., Friscic T., Day G. M., Gladden L. F., Jones W. Terahertz time-domain spectroscopy and the quantitative monitoring of mechanochemical cocrystal formation. *Nat. Mater.*, 2007, 6(3), 206-209.

9 Defects in Pharmaceutical Crystals

9.1 Introduction

As described in Section 1.5, crystal defects are likely to have an influence on the solid-state behaviour of a pharmaceutical compound. To date, however, such a relationship has rarely been investigated. The aim of the work in this Chapter was to use TEM to observe and characterise defects in pharmaceutical crystals, and to find examples linking defects to crystal properties. Three types of defect that are commonly observed in crystals are edge dislocations, screw dislocations and stacking faults. Schematics of an edge dislocation and a screw dislocation are shown in Figure 9.1.

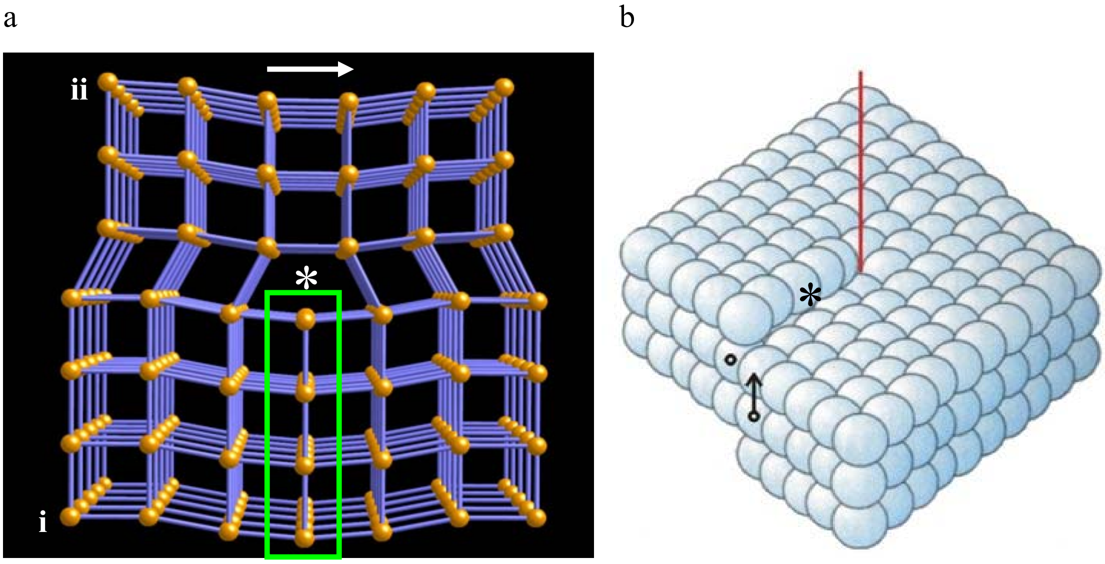

Figure 9.1 Schematics of two types of defects that are present in crystals. (a) An edge dislocation. There is an extra plane of atoms (highlighted by a green box) in the bottom part of the crystal. The core of the dislocation is located at the asterisk, and is running perpendicular to the plane of the page. The Burger's vector of the dislocation is shown with an arrow. (b) A screw dislocation. The dislocation is running in the direction shown by the red line. The Burger's vector of the dislocation is shown with an arrow. The asterisk marks an edge site where molecules can readily attach. This image was taken from the website of the research group of Dr Ulrich T. Schwarz.[1]

An edge dislocation is caused by the presence of an extra half plane of atoms / molecules in a crystal. This is shown in Figure 9.1a by the plane of atoms highlighted with a green box. As can be seen from the figure, the presence of an edge dislocation causes localised distortion of crystal planes. In a screw dislocation one section of a crystal is displaced by a certain distance (usually one unit cell) with respect to an adjacent section (Figure 9.1b). Again, there is localised distortion of the crystal planes. During crystal growth, molecules can readily attach to the edge site (marked with an asterisk in Figure 9.1b). This edge will spiral around the red line creating new layers of molecules and forming a screw dislocation hillock.[2] In order to fully describe these two types of dislocation it is necessary to determine the direction of the defect as well as the associated Burger's vector and slip systems.[3] Burger's vectors for the dislocations in Figure 9.1 are shown by the arrows.

Stacking faults are planar defects caused by displacement or mismatching of whole layers of atoms or molecules.[4] For example, the {111} planes of atoms in a face centred cubic lattice are close packed, and atoms in one layer are shifted with respect to atoms in the layers above and below. These layers form an ABCABCABC type stacking arrangement. A typical stacking fault in this type of structure is an ABCA|CABC sequence (The line marks the location of the defect).[3]

For many materials, defects such as screw dislocations, edge dislocations and stacking faults show up as regions of contrast within TEM images.[5-8] Defects cause local distortion of crystal planes and this can bring them into the correct orientation for Bragg diffraction to occur. This region of the sample will then appear dark due to diffraction contrast. During this investigation into pharmaceutical systems, however, defects were not observed directly through diffraction contrast. The presence of defects in these materials was inferred from their influence on bend contours, using the approach that is described in Section 5.1, and shown in Figure 5.2.

The TEM investigation was complemented by the use of AFM to identify defects at crystal surfaces. Defects in pharmaceutical crystals have been detected previously with AFM by observing the way surface crystal layers are disrupted by the presence of the defects.[2,9]

Defects at the (001) surface of an aspirin crystal are shown in the AFM height image with overlaid amplitude signal in Figure 9.2.

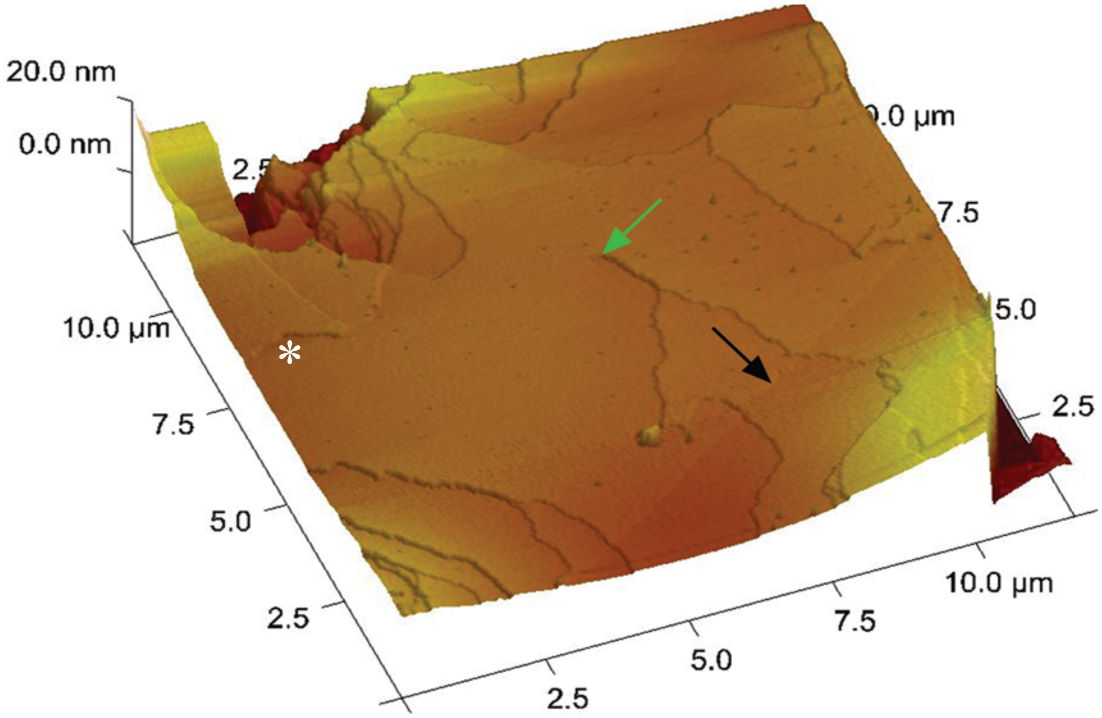

Figure 9.2 An AFM height image with overlaid amplitude signal showing defects on the (001) surface of a crystal of aspirin. The steps which can be seen on the image are the edges of individual layers of molecules. The green arrow highlights a region where a layer of molecules appears to be emergent from the crystal surface. This is a screw dislocation and the position of the green arrow corresponds to the bottom of the red line in the schematic in Figure 9.1b (there is a clockwise screw in the above Figure and an anticlockwise screw in Figure 9.1b). The black arrow highlights a step which runs from bottom left to middle right of the image. The region of crystal surface on the upper left side of this feature is higher than the region on the other side, but the height difference is less than that of one layer of molecules, indicating that the feature is below the crystal surface. This is an edge dislocation and the height difference results from the presence of an incomplete layer of molecules below the crystal surface. In the schematic in Figure 9.1a the surface running between the i and ii symbols is equivalent of the aspirin (001) surface that is shown in this AFM image. The image was recorded by Andrew M. C. Cassidy of the Department of Chemistry, University of Cambridge and is used with permission.

During an AFM measurement, the tip which is used to probe the sample travels in a horizontal path from the left edge of the sample to the right edge and then back again. The tip is then displaced upwards by a small increment, and the horizontal scan is repeated. In this manner, a square or rectangular region of the sample surface is imaged (note that the AFM image in Figure 9.2 has been rotated during image processing). In tapping mode, the tip is also oscillating up and down as it crosses the sample. If the tip moves from a lower to higher region of sample the oscillation amplitude decreases and vice versa (there is a feedback loop to ensure that when a change in amplitude is detected an adjustment is then made to restore the original amplitude). This information is recorded as an amplitude signal, and can be used to show whether the tip has moved upwards or downwards on encountering each of the steps on the crystal surface when travelling in a given direction (either to the left or to the right) across the sample. One way of visualising AFM amplitude images is to imagine that light is shining from either the left or right side of the image. Steps on the sample surface, corresponding to the edges of layers of molecules, will either be ‘lit up’, or ‘in shadow’, depending on their orientation. This can be seen for the edge of a layer of aspirin molecules that is highlighted with an asterisk in Figure 9.2.

Defects were observed in crystals of several pharmaceutically active compounds using both TEM and AFM. Defects in crystals of Form II of theophylline were studied in detail in order to determine the nature of the defects and observe their influence on crystal behaviour.

9.2 Results

9.2.1 Defects in Crystals of Form III of the 1:1 Caffeine:Theophylline Cocrystal

Crystals of Form III of the caffeine:theophylline cocrystal with a thin, lath morphology were prepared by slow evaporation of a 3:2 DMF:dioxane solution. These crystals were analysed by TEM, and were found to have relatively large areas that were thin enough to bend, hence giving rise to bend contours. Defects were identified in the resulting images (Figure 9.3).

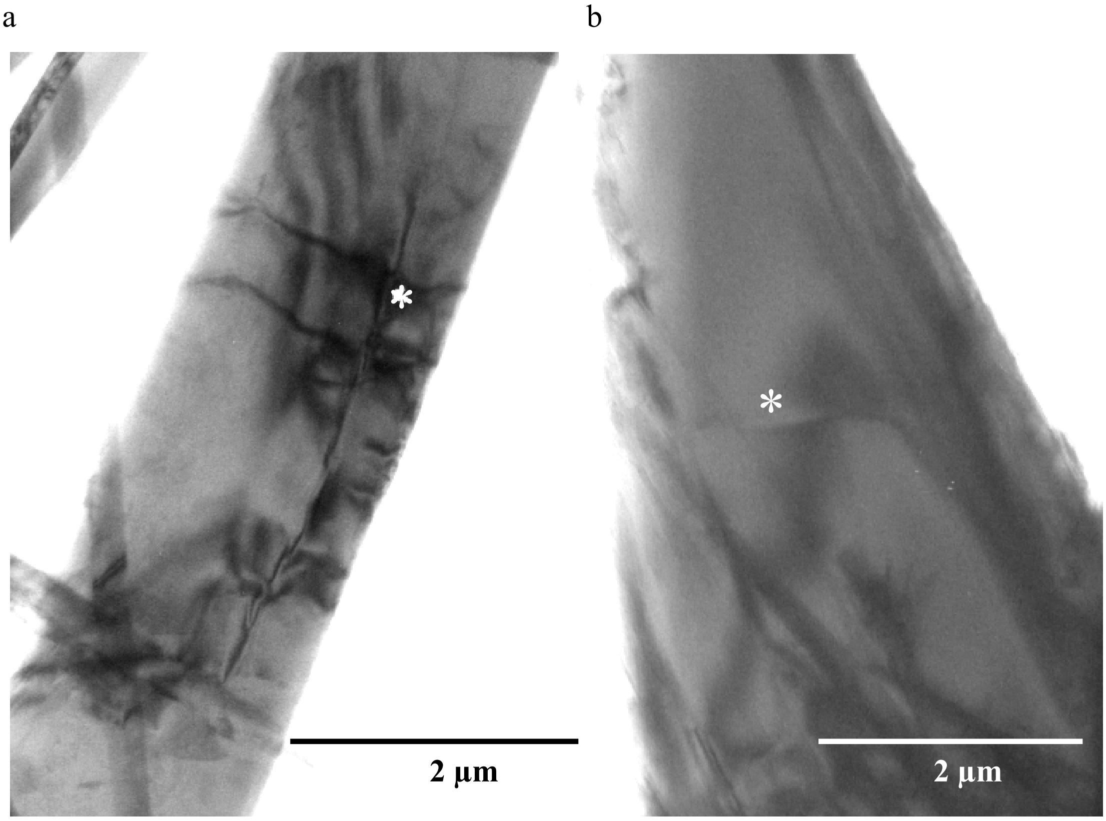

Figure 9.3 TEM images showing defects in a sample of Form III of a caffeine: theophylline cocrystal. (a) TEM image showing a lath shaped crystal. The asterisk marks a defect which runs along the length of the crystal. The defect does not run in a straight line and has a characteristic appearance of a linear (pure edge or pure screw) dislocation. (b) The asterisk in this image indicates a region where a bend contour is disrupted by the presence of a defect.

A screw / edge dislocation can be seen running for approximately 3 µm along the length of the crystal shown in Figure 9.3a. The presence of a defect in Figure 9.3b is revealed by disruption to a bend contour.

9.2.2 Defects in Crystals of Form I of Aspirin

Large, plate-like crystals of aspirin were prepared by evaporation of an acetonitrile solution on a TEM sample grid, and were found to be suitably thin for TEM imaging (Figure 9.4a). Despite the large numbers of bend contours in the TEM images of this sample, there were few clear signs of disruption due to the presence of defects. The asterisks in Figure 9.4b show the location of one of the few defects that have been observed in an aspirin crystal.

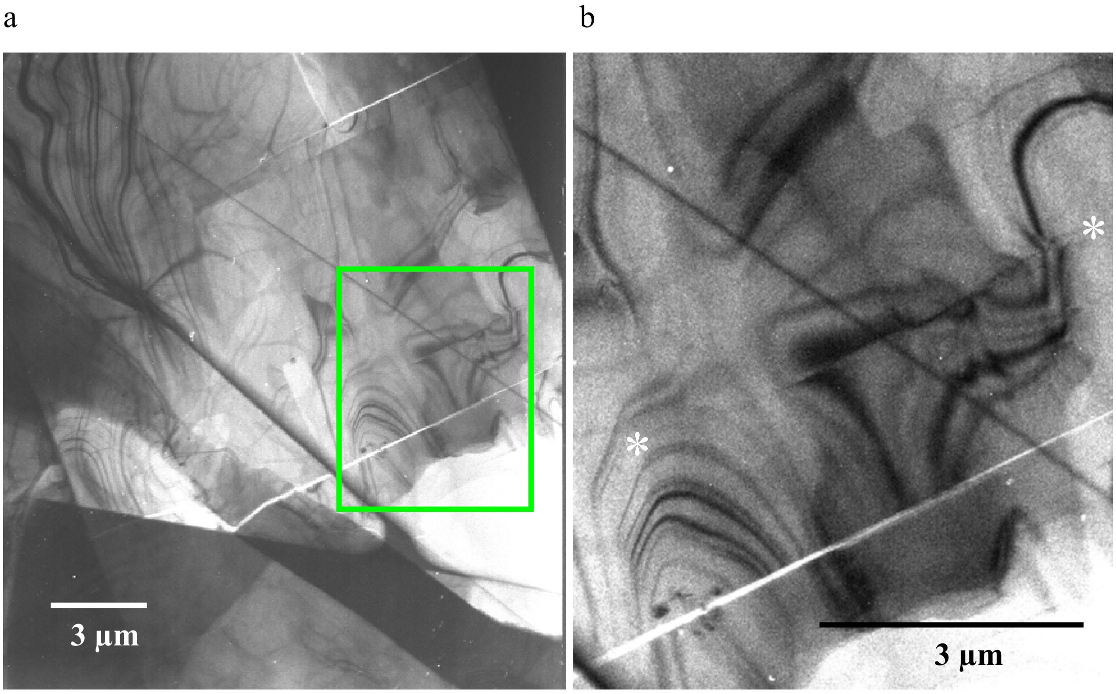

Figure 9.4 TEM images showing a defect in a sample of Form I of aspirin (measured at -178 °C). (a) TEM image showing a thin-plate crystal. The white lines on the image are cracks in the crystal. The two dark lines running from top left to bottom right on the image are artefacts from the holey carbon sample support grid. (b) A magnification of the region highlighted in image (a). The asterisks are at the ends of a defect running from left to right across the crystal. The defect does not run in a straight line and has a characteristic appearance of a linear (edge or screw) dislocation.

9.2.3 Defects in Crystals of Form II of the 5-Flourouracil:Phenazine Cocrystal

Small crystallites of the 5-fluorouracil:phenazine cocrystal were prepared by rapid evaporation of a methanol solution directly onto a TEM grid (see Section 4.3.8 for further details of the preparation method). TEM images showed that these crystals had a rectangular plate morphology, and bend contours on the crystals were heavily disrupted by series of closely spaced defects which ran in a direction perpendicular to the long edge of the crystals (Figure 9.5). The density of defects was far greater than that seen for the caffeine:theophylline cocrystal and aspirin, probably because the 5-fluorouracil:phenazine cocrystal is a layered structure with weak interactions between the layers, which could lead to the formation of stacking faults.

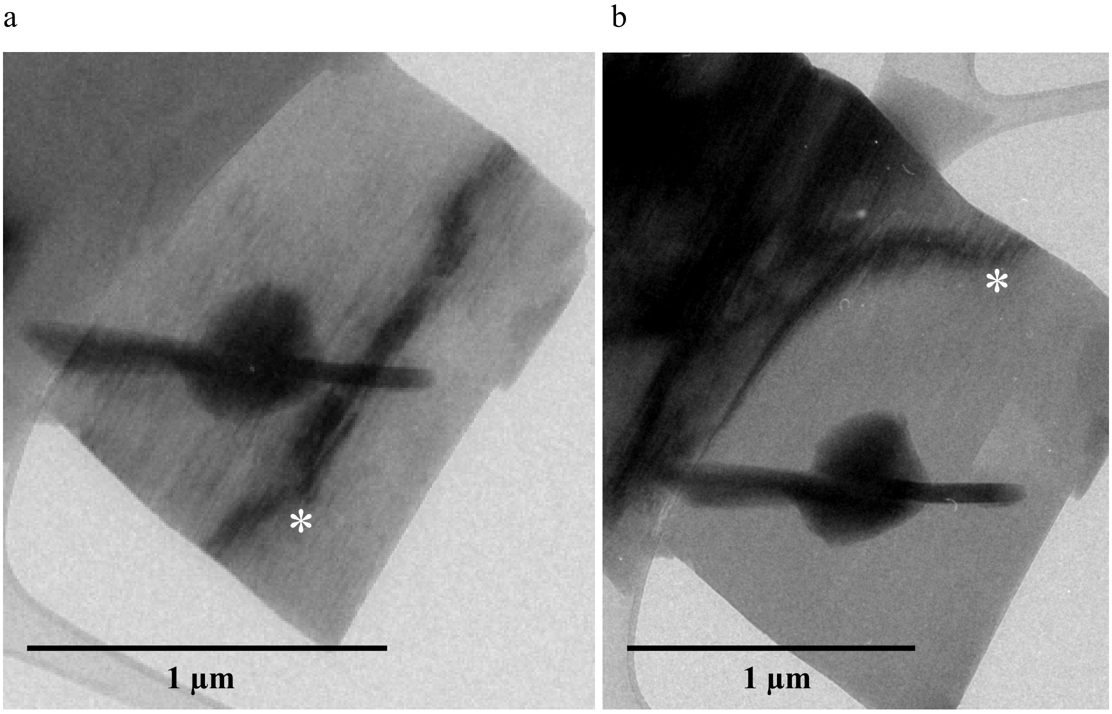

Figure 9.5 (a and b) Two TEM images showing defects in a crystal of Form II of a 5-fluorouracil:phenazine cocrystal prepared by rapid evaporation from methanol. Bend contours on the two images are marked with asterisks. Both of the bend contours are disrupted by defects running across the width of the crystal.

Additional information about the nature of these defects was obtained from electron diffraction analysis of the sample. A majority of the diffraction patterns that were recorded showed heavy streaking, or a combination of streaking and reflections (Figure 9.6). This kind of streaking is often observed in structures containing stacking faults and results from diffuse scattering from the strained regions around these defects.

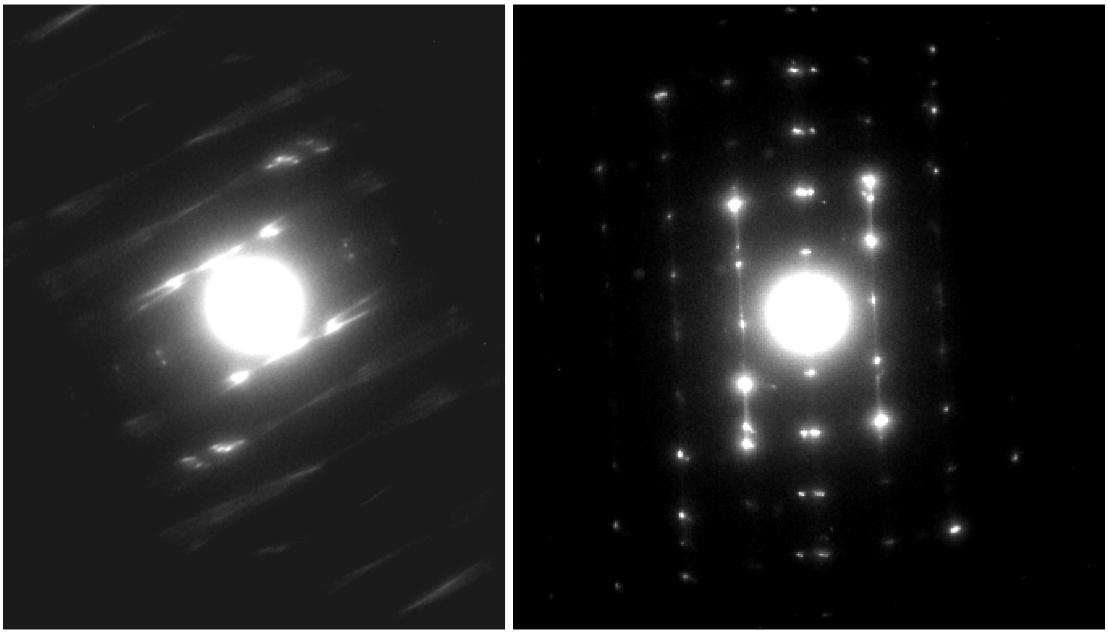

Figure 9.6 Electron diffraction patterns from a sample of Form II of the 5-fluorouracil:phenazine cocrystal prepared by rapid evaporation from methanol. Both diffraction patterns show streaking, which is indicative of stacking faults (it is not known in which crystallographic direction the streaking occurs as no crystal structure of this form has been determined to date). The second pattern has contributions from more than one crystal domain as evidenced by the double row of reflections above and below the central spot.

The XRPD trace of the sample was highly unusual, with just a single reflection evident at 28.2 °2θ (Figure 9.7). This value corresponds to a d-spacing of 3.13 Å. Though the crystal structure of Form II of the phenazine:mesaconic acid cocrystal is unknown, it was possible to derive useful information from the Form I structure. 5-fluorouracil molecules form hydrogen bonded chains which are bridged by phenazine molecules through weak interactions to give a 2-dimensional sheet (Figure 9.8a). The sheets are parallel to the (120) crystal plane (Figure 9.8b) and the corresponding interplanar spacing, $d_{(120)}$, was calculated to be 3.122 Å. This value is very close to the d-spacing corresponding to the reflection seen in the XRPD trace of Form II of the cocrystal, indicating that Form II may have a similar sheet structure to that seen in Form I. The two Forms would then differ in the 3-dimensional packing arrangement of the sheets (polytypism).

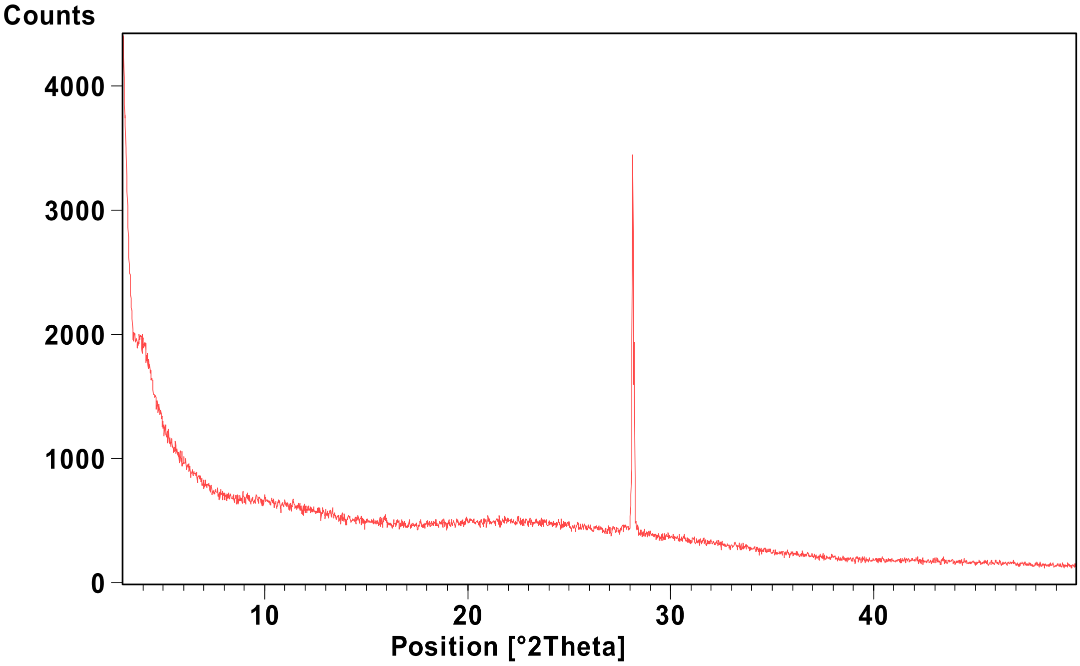

Figure 9.7 XRPD trace of a sample of Form II of the 5-fluorouracil:phenazine cocrystal prepared by rapid evaporation from methanol.

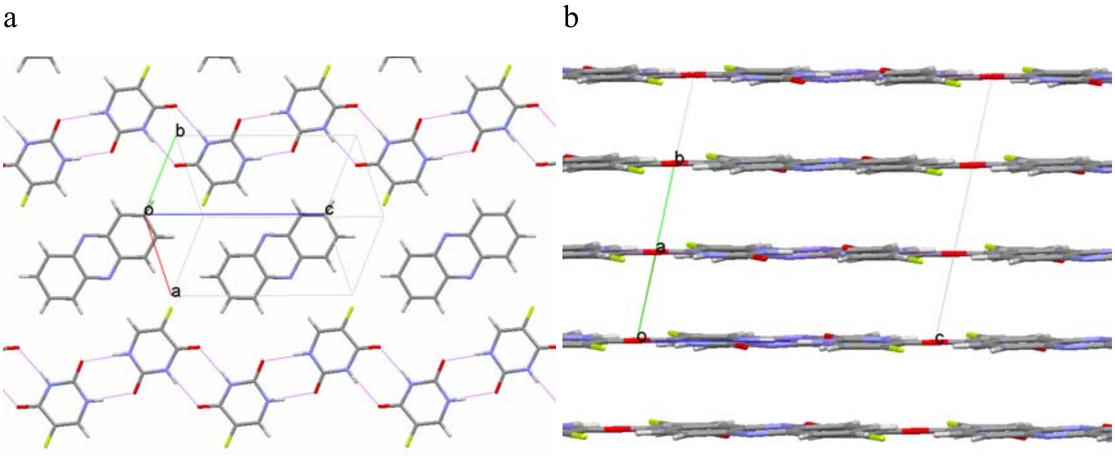

Figure 9.8 (a) The molecular packing arrangement in Form I of the 2:1 5-fluorouracil:phenazine cocrystal. (b) 5-fluorouracil and phenazine molecules form sheets which are aligned with the (120) crystal plane.

It is likely that the observation that there is only one peak in the XRPD trace of Form II of the 5-fluorouracil:phenazine cocrystal (and that this peak corresponds to the interlayer spacing of the crystal form) is related to the presence of stacking faults in the crystals. As stated above, Form II is expected to contain sheets of 5-fluorouracil and phenazine molecules that are parallel to each other, as in Form I of the cocrystal. As there would only be weak interactions between sheets, it is possible that the registry between adjacent sheets would not be perfect throughout the crystal, resulting in stacking faults (as observed with layered materials such as graphite).[10] If the density of stacking faults were great enough, the only coherent set of crystal planes would be the (120) planes, and only one reflection would be observed by XRPD.

As reflections were observed in the electron diffraction patterns of Form II of the cocrystal (Figure 9.6), and not just streaking, there must be domains within the crystals where the registry of layers is perfect. These domains are too small to coherently scatter X-rays, however, which interact with the sample less strongly than electrons.

9.2.4 Defects in Crystals of Form I of Paracetamol

Paracetamol crystals grown directly onto a TEM grid, either by crystallisation from the melt or by crystallisation from acetic acid, were found to be comprised of multiple smaller crystalline domains (Figure 9.9). In Figure 9.9a there is a domain boundary which can be identified by the way bend contours abruptly end where they meet the boundary. A second domain boundary can be seen in the image of a paracetamol crystal grown from acetic acid in Figure 9.9b.

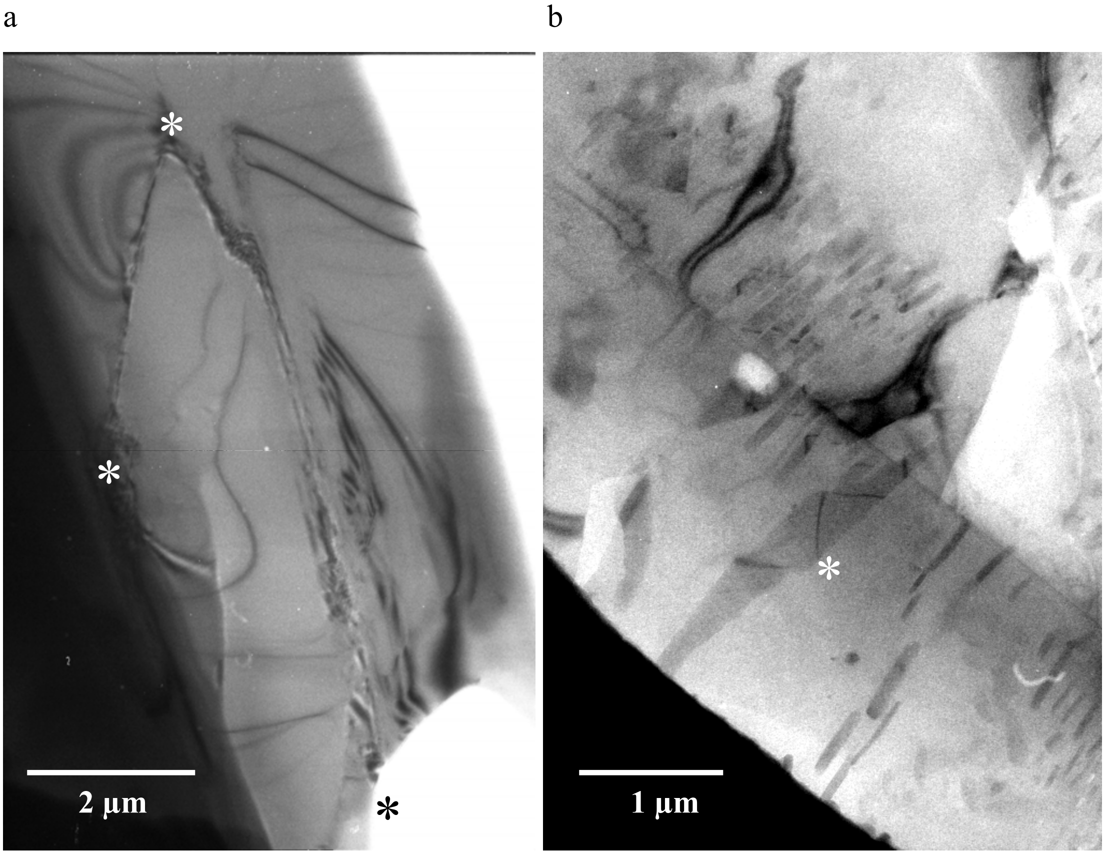

Figure 9.9 TEM images showing domain boundaries in crystals of Form I of paracetamol. (a) TEM image showing a plate-like crystal obtained by cooling paracetamol from a melt. There is a domain boundary that runs in a curved path marked with three asterisks. (b) TEM image showing a plate-like particle of paracetamol crystallised from acetic acid. There is a linear domain boundary running from upper left to lower right on the image. There are also several small, discrete crystalline domains such as the one marked with an asterisk. It is hard to say conclusively whether these are domains within the larger crystal, or whether they are crystallites on the surface.

9.2.5 Defects in Crystals of Form I of Nifedipine

Defects were not observed in large numbers in crystals of nifedipine by TEM. This was in part because nifedipine crystals lost crystallinity in the electron beam within two or three minutes, so bend contours were quickly lost. One example of defects disrupting a bend contour in a nifedipine crystal is shown in Figure 9.10a. Defects at the surface of nifedipine crystals were studied by AFM, and features characteristic of emergent screw dislocations at the surfaces of the crystals were observed (Figure 9.10b). It is unlikely that the defects observed by TEM are related to those seen by AFM as the Burgers' vector of the screw dislocation in the AFM image is probably in the [100] direction (perpendicular to the (100) plate face of crystals of nifedipine), whereas the defects seen to be disrupting bend contours are likely to be running approximately parallel to the plate face of the crystals. Emergent screw dislocations have been observed by TEM in theophylline crystals, as small circular distortions in bend contours (see Figure 9.11b), but have not been seen to date in nifedipine crystals.

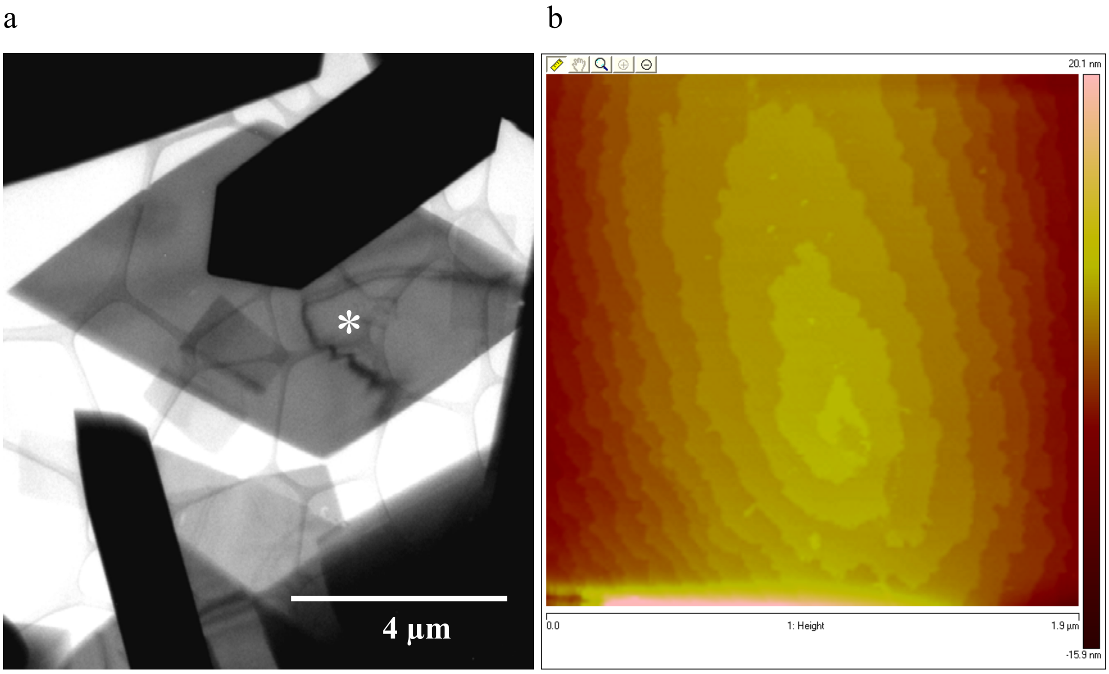

Figure 9.10 Analysis of defects in crystals of Form I of nifedipine prepared by evaporation from ethanol. (a) TEM image showing a rectangular plate crystal with disruption to a bend contour in the region marked with an asterisk indicating the presence of defects. (b) AFM height image of the (100) surface showing a screw dislocation hillock at the surface of a nifedipine crystal. Each step was measured to be approximately 12 Å in height, corresponding to one layer of molecules. The screw dislocation emerges from the crystal surface at the centre of the hillock.

9.2.6 Defects in Crystals of Form II of Theophylline

9.2.6.1 Observation of Crystal Defects in Form II of Theophylline by TEM

The number of defects that were observed in crystals of Form II of theophylline was found to be dependant on the preparation method. For example, crystallisation rate was found to be an important factor. Two solutions of theophylline in nitromethane at 2.5 mg.ml^{-1} and 5.0 mg.ml^{-1} were prepared with heating to aid dissolution, and then stored at -30 °C to induce precipitation. Precipitation from the 5 mg.ml^{-1} solution was rapid, whereas it took several minutes before precipitate formed in the 2.5 mg.ml^{-1} solution. Crystals from both samples were pipetted onto TEM grids for analysis, and it was observed that crystals that formed more slowly had fewer defects (Figure 9.11).

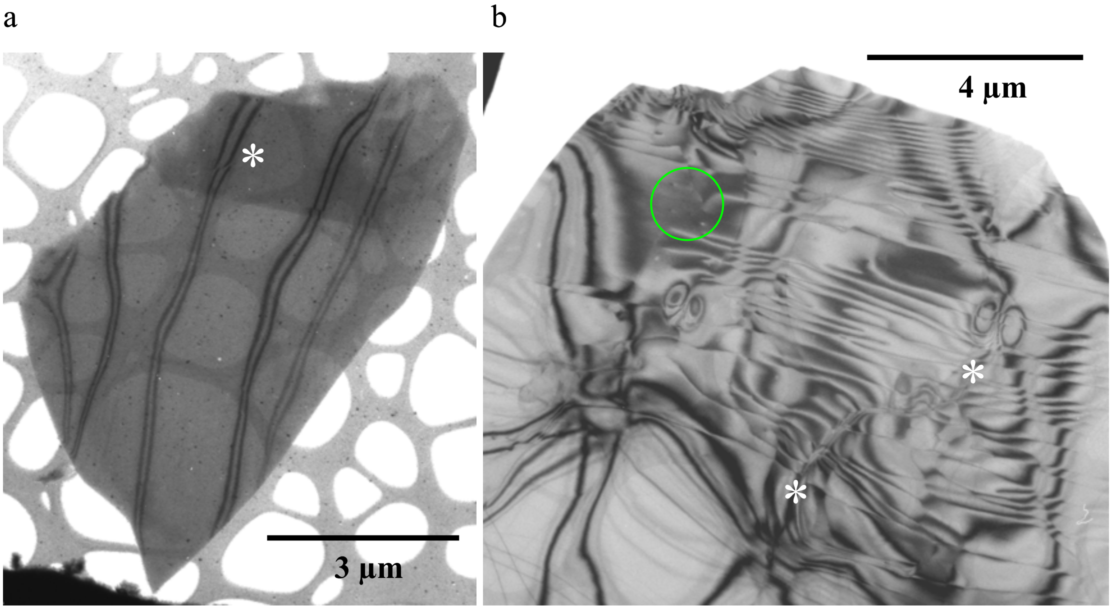

Figure 9.11 TEM images of plate-like crystals of Form II of theophylline crystallised at different rates. (a) A crystal prepared by cooling a 2.5 mg.ml^{-1} solution of theophylline in nitromethane. There is only one region where a bend contour is disrupted by the presence of a defect (highlighted with an asterisk). (b) A crystal grown more rapidly by cooling a 5.0 mg.ml^{-1} solution of theophylline in nitromethane. Bend contours are heavily disrupted showing the presence of many defects. The four small dots in the circled region are points where linear (edge or screw) dislocations emerge from the crystal surface. The defect running between the two asterisks on the image is also characteristic of a linear dislocation.

9.2.6.2 Characterisation of Crystal Defects in Form II of Theophylline

Crystals of Form II of theophylline were studied in more detail by TEM in order to gain more information about the defects that were observed in these crystals, such as which direction they run in and whether they are edge dislocations, screw dislocations or stacking faults. One particular type of defect was observed frequently. This defect was relatively linear, running for several microns across crystals indicating that it was in the same plane as the plate surface. By comparing TEM images and diffraction patterns from the same region of sample it was determined that the defects run in the [010] crystallographic direction (Figure 9.12).

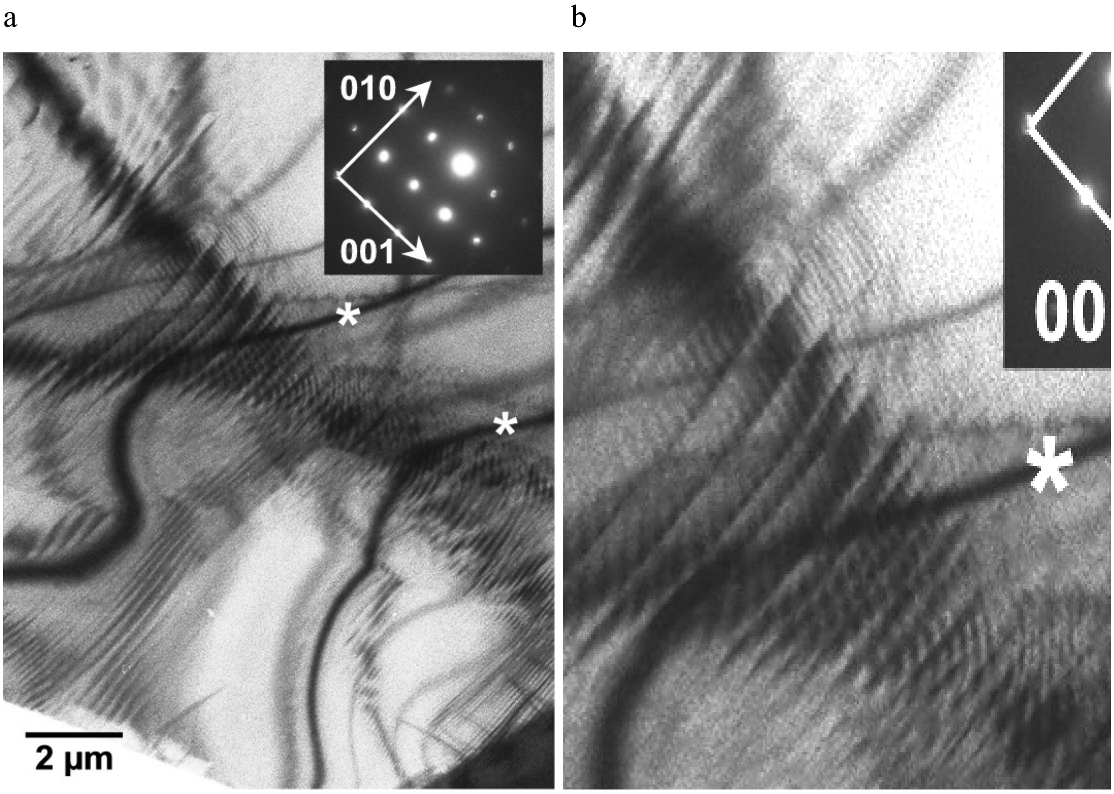

Figure 9.12 (a) TEM image showing defects in a crystal of Form II of theophylline. The defects are revealed by disruption to bend contours. It is evident that the defects are running in the [010] crystallographic direction. The two bend contours marked with asterisks are not disturbed in the vicinity of the defects. This indicates that the defects do not cause bending of the crystals planes which give rise to these bend contours. (b) A magnified region of the image showing these features in greater detail.

It was also evident that some bend contours were not disrupted in the presence of these defects, demonstrating that the crystal planes giving rise to these bend contours were not bent by the defects. Dark field images were recorded to determine which crystal planes these bend contours corresponded to (Figure 9.13).

The TEM image in Figure 9.13a again shows defects running in the [010] direction. There is one pair of bend contours that were not disturbed by these defects (Figure 9.13d). Dark field imaging revealed that one of these bend contours corresponded to the (002) crystal planes (the other is likely to correspond to the (00-2) planes). Reflections from the (001) and (00-1) planes are not observed as they are systematic absences.

This result demonstrated that the (002) planes were not distorted by the defects running in the [010] direction in theophylline crystals, and enabled a calculation of the nature of the defects to be performed. The observation was not consistent with the defects being edge dislocations, as an edge dislocation running in the [010] crystallographic direction would be expected to cause bending of the (002) crystal planes. The defects are most likely to be screw dislocations with a Burger's vector in the [010] direction. Screw dislocations in metallic or inorganic solids do not tend to be as straight as the defects observed in the theophylline crystals, but this may just be an effect related to the crystal structure of Form II of theophylline where there are hydrogen bonding interactions instead of coulombic interactions, and very weak interactions between layers of molecules (in the [100] crystallographic direction). The slip plane associated with the screw dislocation is the (100) plane. Again, this is related to the weak nature of interactions between layers of theophylline molecules, which lie in the (100) plane. The slip direction for the screw dislocation is the [001] direction (the direction in the slip plane that is perpendicular to the direction of the Burger's vector). A second possibility is that the defects are stacking faults.

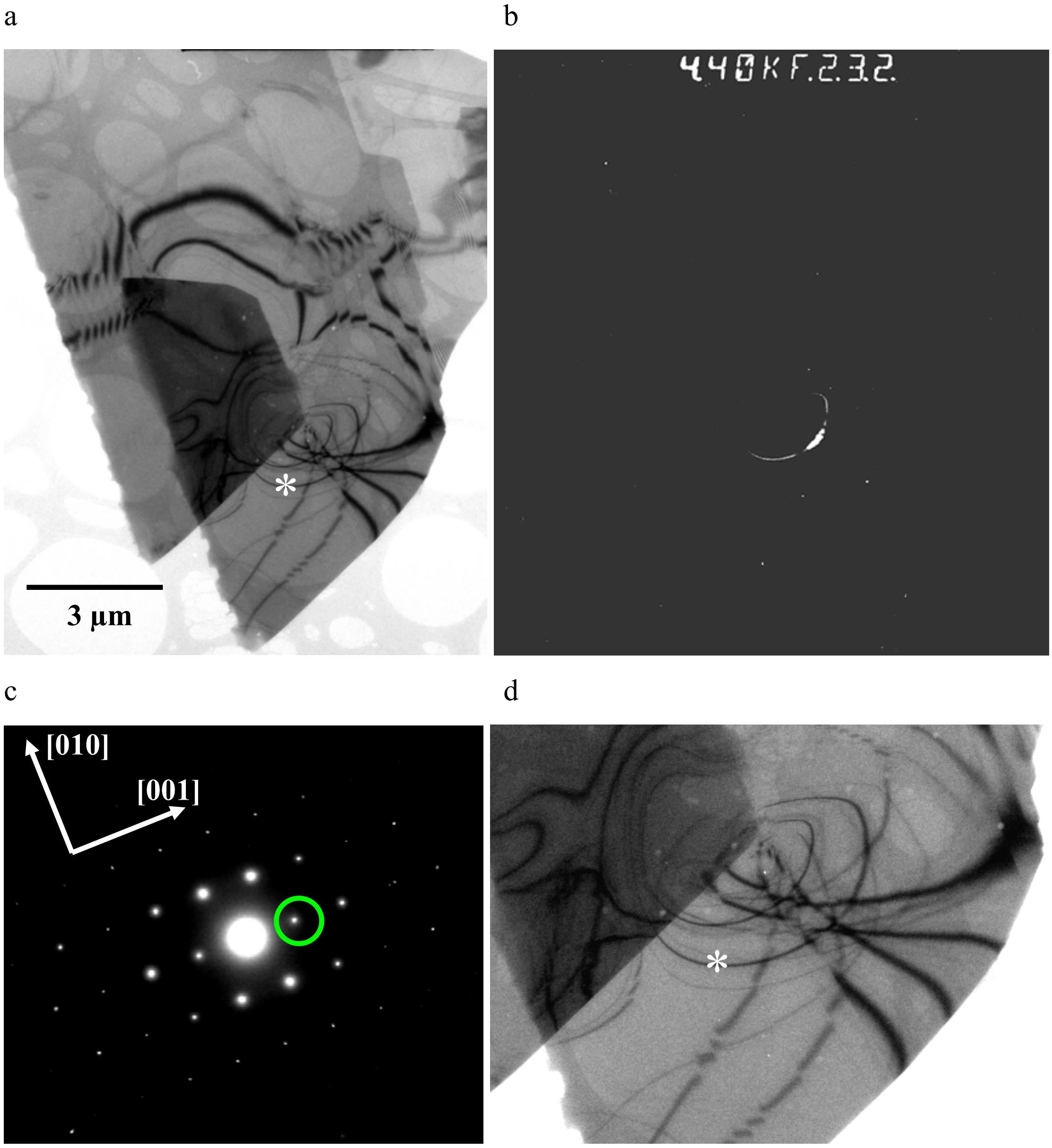

Figure 9.13 (a) TEM image showing defects in a crystal of Form II of theophylline. The defects are revealed by disruption to bend contours. Two oval shaped bend contours, one running through the asterisk, and one just above the asterisk, are not disrupted by the defects. (b) A dark field image showing one of the oval shaped bend contours. This image was recorded using the (002) reflection (which is circled in the corresponding diffraction pattern), demonstrating that this bend contour resulted from Bragg diffraction from the (002) planes. (c) Electron diffraction pattern taken from a region just above and to the right of the asterisk in image (a). This pattern was indexed to the <100> zone axis of Form II of theophylline. (d) A magnified region of the TEM image showing features in more detail.

9.2.6.3 Observation of Crystal Defects in Form II of Theophylline by AFM

AFM analysis was performed to look for evidence of either screw dislocations or stacking faults at the surface of theophylline crystals to aid characterisation of the defects that were observed by TEM. The surfaces of the large (100) faces of theophylline crystals were analysed. Screw dislocations, edge dislocations and possible stacking faults were observed. The two AFM amplitude images in Figure 9.14 each show a small region of the surface of a crystal of theophylline where screw dislocations are evident. Steps showing the edges of several crystal layers can be seen at the left hand side of Figure 9.14a, but they abruptly end in the region of the crystal at the centre of the image. This is indicative of a series of screw dislocations. A similar observation was made for the crystal in Figure 9.14b where a series of steps marking the edge of crystal layers run from the side of the crystal (at the top of the image) and end at screw dislocations.

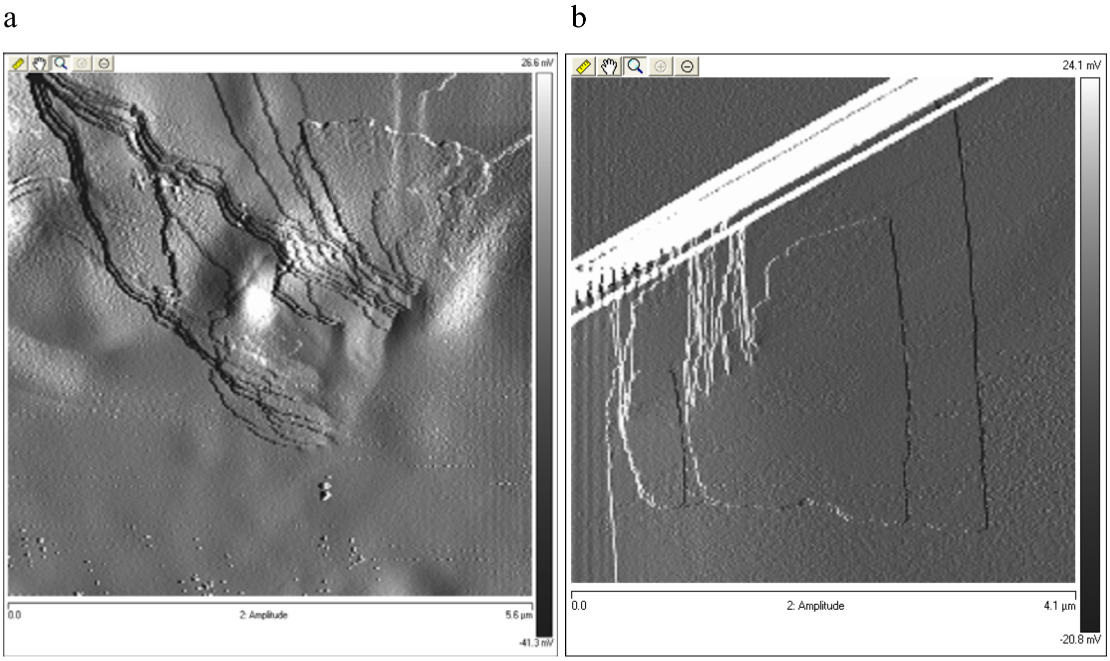

Figure 9.14 AFM amplitude images showing screw dislocations emergent at the (100) surface of crystals of Form II of theophylline.

The AFM analysis also generated several examples of edge dislocations at the surface of theophylline crystals. The AFM amplitude image in Figure 9.15a shows the edge of crystal layer, marked by asterisks, which is on the crystal surface at the left hand asterisk, and below the crystal surface at the right hand asterisk. The height of this crystal layer edge was measured to be approximately 12 Å, corresponding to a single layer of theophylline molecules. In the region where this incomplete crystal plane is below the crystal surface it is an edge dislocation. The Burger's vector of this dislocation is in the [100] direction with a magnitude of approximately 12 Å. The image in Figure 9.15b also shows crystal layers which are on the crystal surface in one region of the crystal (at the uppermost asterisk of each pair) and below the surface in another region. The main difference is that in this image, the edges of these features correspond to more than one layer of theophylline molecules (the steps heights correspond to approximately 32 layers, or 16 unit cells, for both edges).

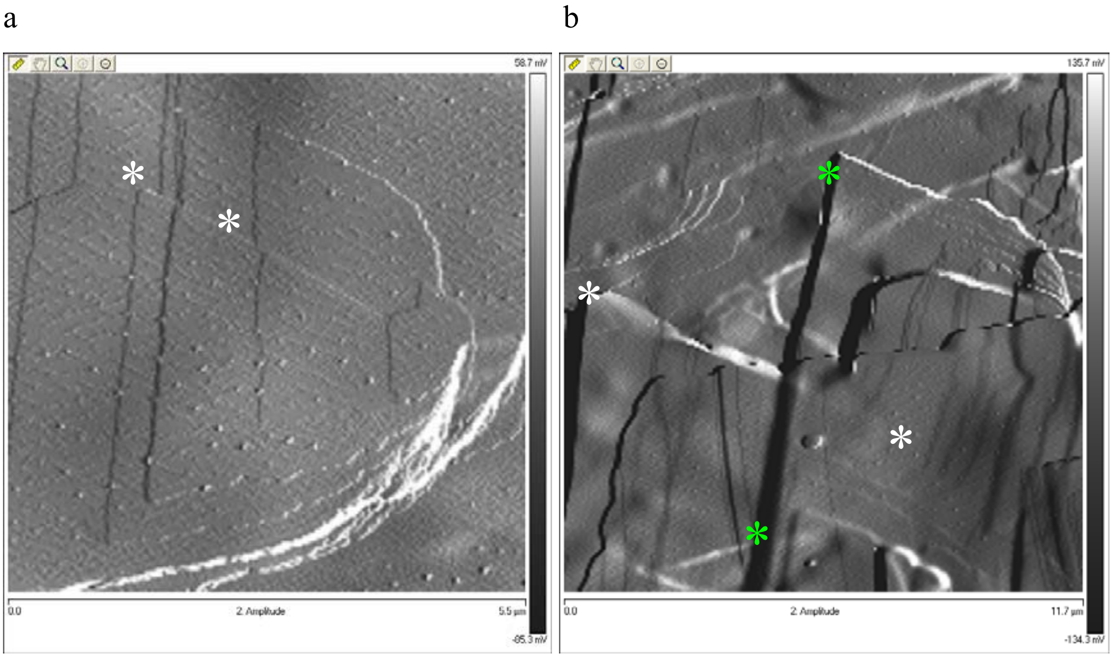

Figure 9.15 AFM amplitude images showing edge dislocations and a possible stacking fault at the (100) surface of crystals of Form II of theophylline. The pairs of asterisks show edges of layers of molecules that are on the crystal surface in one region of the crystal, and below the crystal surface in another region.

The image in Figure 9.15a may also show a stacking fault. Form II of theophylline has a layered structure and adjacent layers are rotated with respect to each other giving an ABAB type arrangement (Figure 9.16). The height difference at the edge dislocation marked by the right hand asterisk corresponds to one layer of theophylline molecules. This suggests that the crystal layers at the surface in this region are lying on an A layer on one side of the edge and on a B layer on the other side. This would result in a stacking fault as there will be an AA or BB arrangement of layers on one side of the edge dislocation.

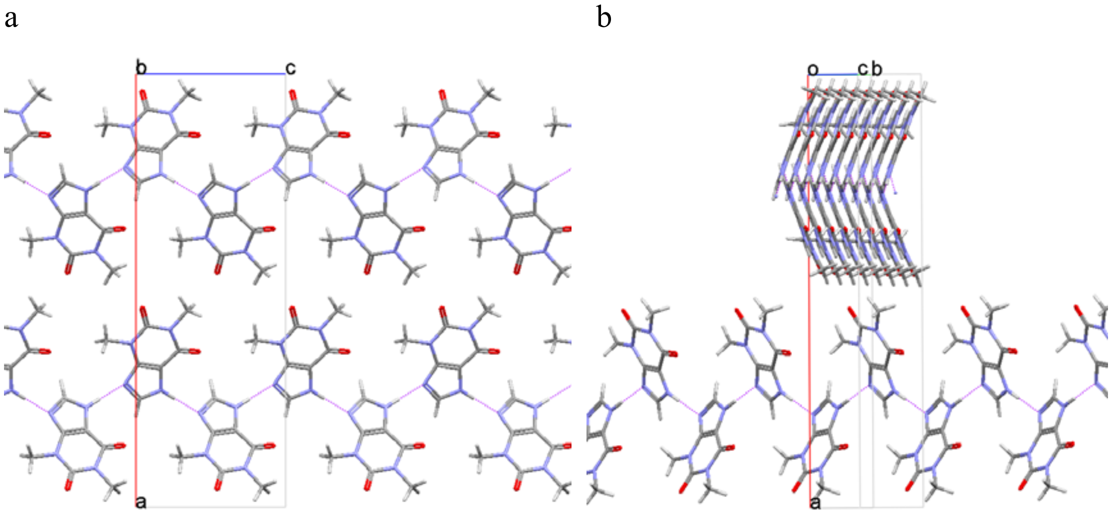

Figure 9.16 The molecular packing arrangement in Form II of theophylline. (a) View down the b-axis showing two sheets of theophylline molecules edge-on. (b) View approximately parallel to the (110) crystal plane showing that there is a rotation between adjacent sheets. For clarity, only one hydrogen bonded chain of theophylline molecules is shown in each layer.

9.2.6.4 Electron Diffraction Evidence for Crystal Defects in Form II of Theophylline

Further evidence of the presence of stacking faults in crystals of Form II of theophylline was obtained from electron diffraction analysis. The electron diffraction pattern from the <100> zone axis of a crystal of theophylline that is shown in Figure 9.17 contains reflections that are not seen in the simulated trace of the same zone axis (Figure 9.17b). Three additional reflections are found evenly spaced between each of the expected reflections and correspond to diffraction from crystal planes that do not exist in Form II of theophylline, or to planes that give systematic absences, indicating a quadrupling of the unit cell in the c-direction. Further work is required to determine if these extra reflections relate to the defects that are frequently observed running in the [010] crystallographic direction in TEM images.

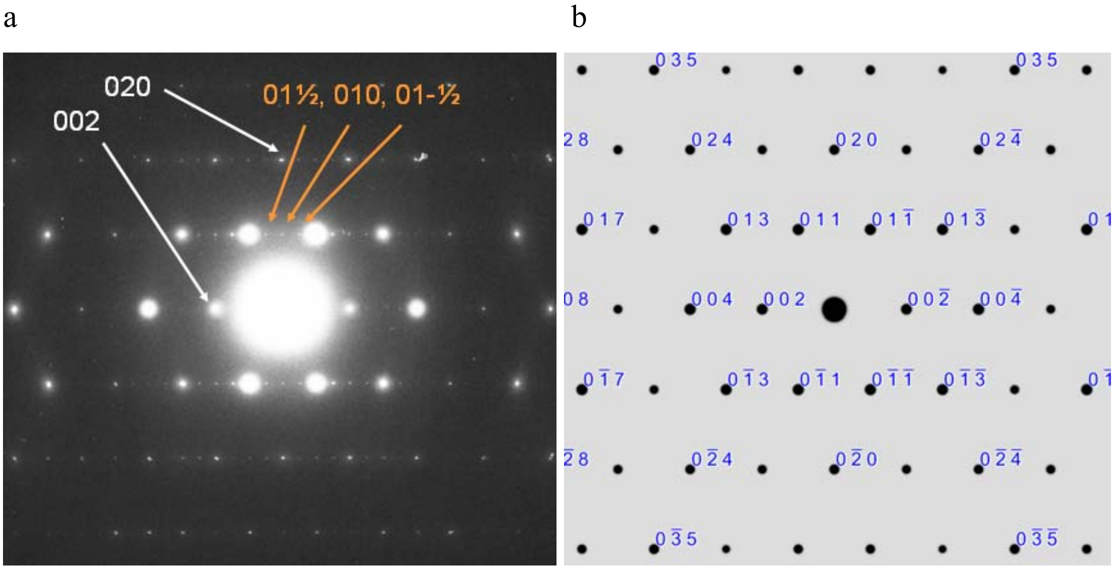

Figure 9.17 (a) TEM electron diffraction pattern from the <100> zone axis of a crystal of theophylline which contains additional reflections to those expected. Examples of the extra reflections are highlighted with orange arrows. (b) Simulated electron diffraction pattern of the <100> zone axis of form II of theophylline.

9.2.6.5 The Influence of Defects on the Solid-State Behaviour of Form II of Theophylline

Crystallising Form II of theophylline by cooling saturated solutions of theophylline in solvents such as nitromethane, ethyl acetate and dioxane yielded crystals with a triangular morphology (Figure 9.18a). It was observed that if a slurry of these triangular crystals was stored for a period of several weeks under ambient conditions, large changes in crystal morphology occurred (Figure 9.18b). The resulting crystals were trapezoidal in shape, and appeared to be fragments of larger triangular crystals that had undergone fracturing (Figure 9.18c and d). It was subsequently found that this fracturing could be induced by applying gentle pressure with tweezers to triangular crystals of theophylline.

This solid state behaviour appears to be linked to the defects which are frequently observed in crystals of Form II of theophylline running in the [010] crystallographic direction. An experiment that linked crystal habit and crystal morphology for Form II of theophylline that was described in Section 5.3.6 (Figure 5.18) showed that the [010] crystallographic direction runs parallel to the base of the triangular crystals. The position of the defects on the triangular crystals of theophylline is shown schematically for a TEM image and a PLM image in Figure 9.18e and f. It is evident that the theophylline crystals fracture in the same direction as the defects, suggesting that the defects are involved in the fracturing process.

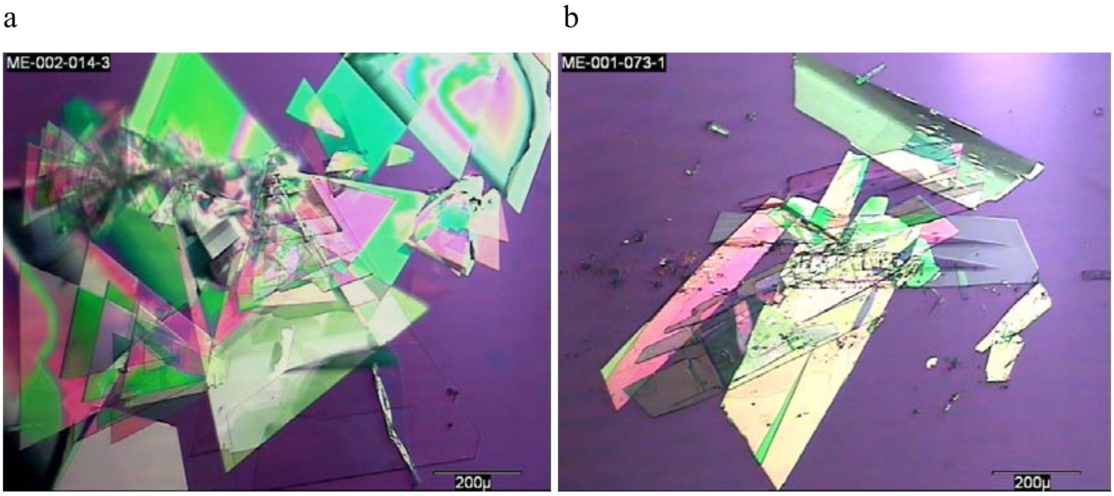

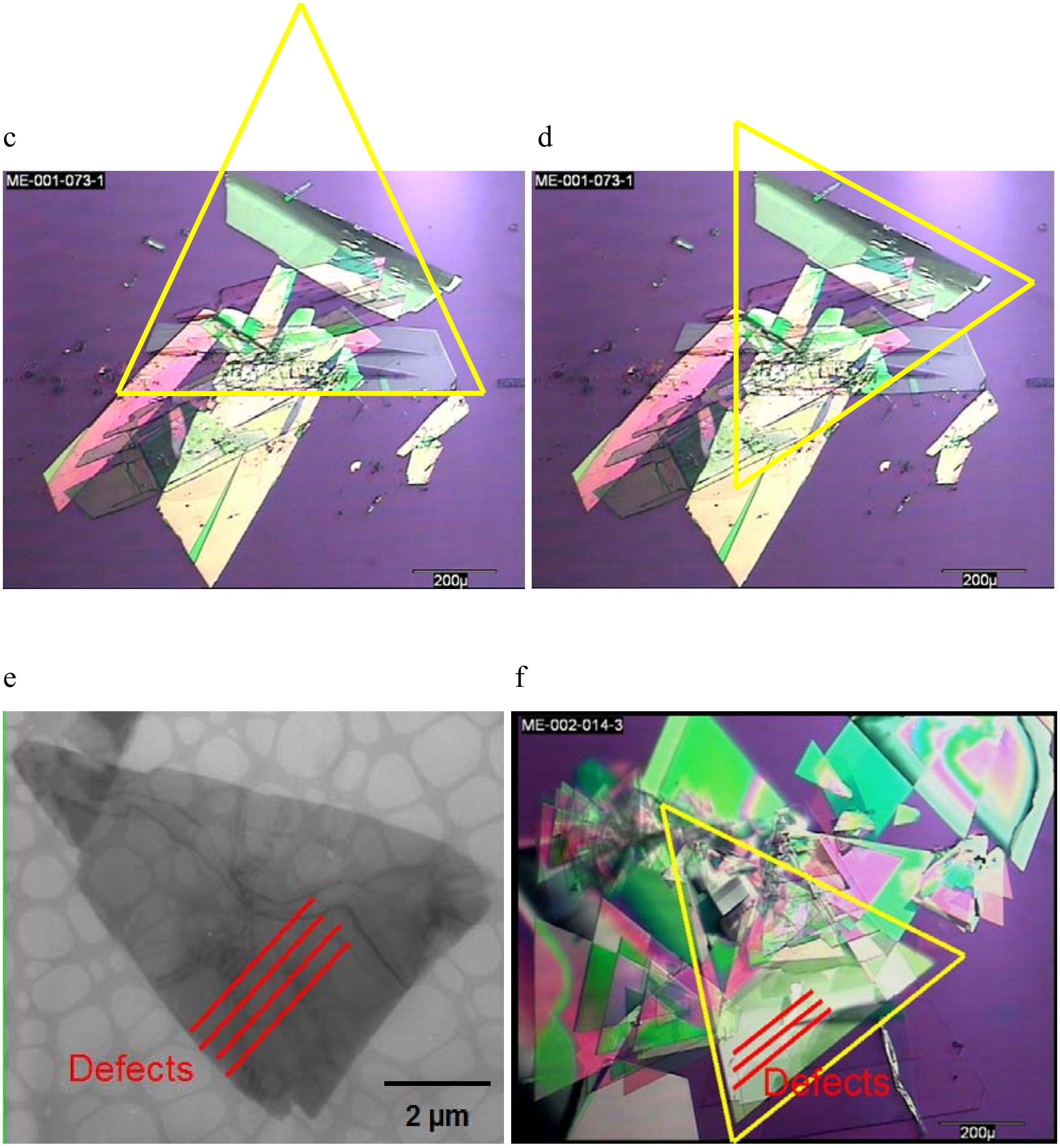

Figure 9.18 Images showing evidence that defects are involved in the fracturing of crystals of Form II of theophylline. (a) A PLM image of triangular crystals of theophylline shortly after preparation by crystallisation from dioxane. (b) A sample of triangular crystals that was re-analysed after several weeks of storage as a slurry under ambient conditions. The crystals now have a trapezoidal appearance. (c & d) The trapezoidal crystals are fragments of triangular crystals that have undergone fracturing. (e) A TEM image showing the direction of frequently observed defects ([010] direction) in relation to the triangular crystal morphology. (f) A PLM image showing that the crystal defects run parallel to the direction in which crystals fracture.

The triangular morphology that was observed for crystals of Form II of theophylline is not only highly unusual for a molecular species, it is also significantly different to the rectangular plate habit that is that predicted for this crystal form by the BFDH model (Figure 9.19a).[11]

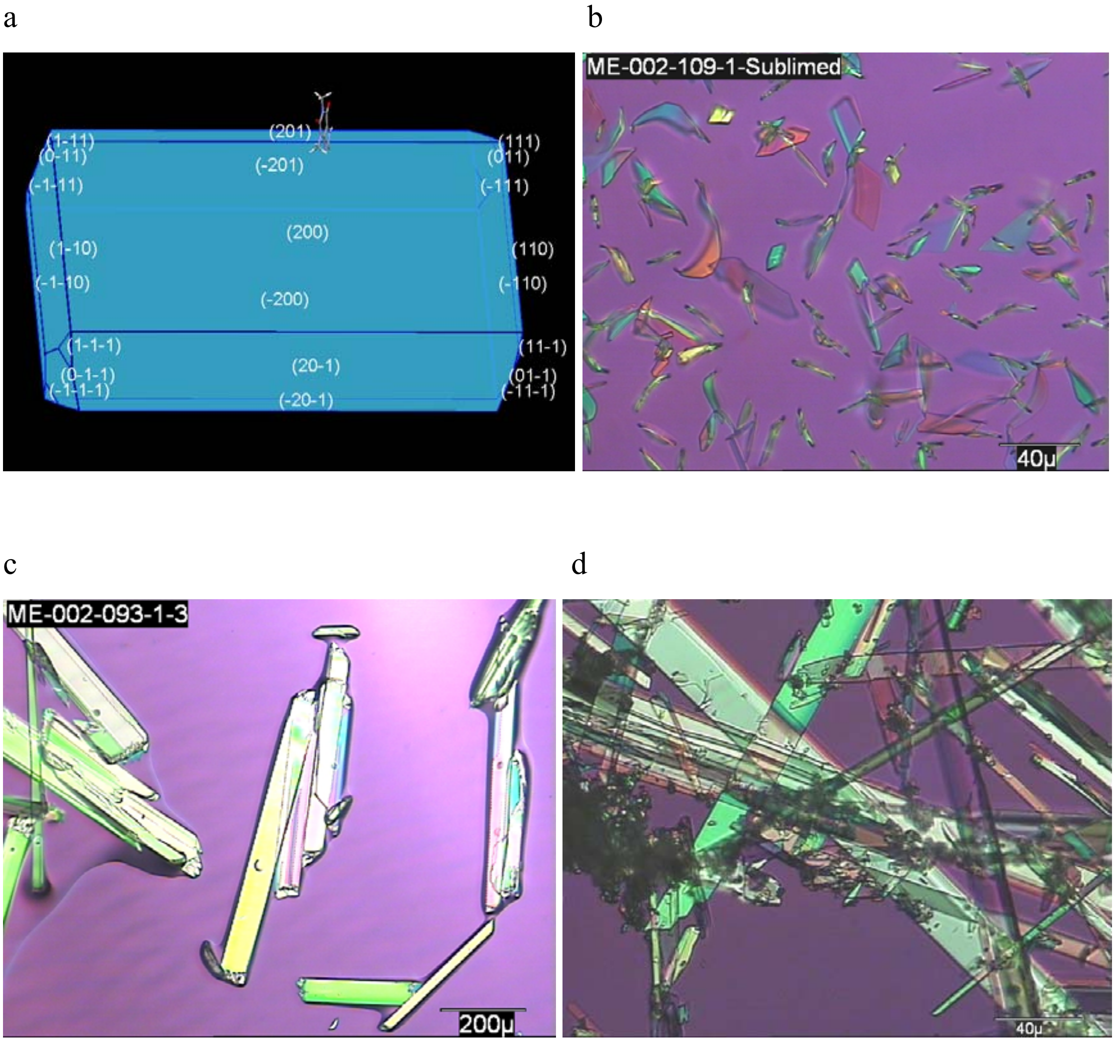

Figure 9.19 (a) Predicted crystal morphology of Form II of theophylline (using a BFDH model and CSD structure BAPLOT01).[12] (b) PLM image of crystals of Form II of theophylline prepared by sublimation. (c) PLM image of crystals of Form II of theophylline prepared by crystallisation from methanol. (d) PLM image of crystals of Form II of theophylline prepared by slow crystallisation from dioxane.

Theophylline crystals with a rectangular plate morphology, or a related lath morphology, were prepared experimentally under certain conditions. Crystals grown by sublimation (generated by heating a sample of theophylline to 250 °C and condensing the resulting vapour on a cooler glass surface situated above the sample) had a variety of habits including rectangular plates, laths and triangles (Figure 9.19b). Lath shaped crystals of Form II of theophylline were prepared by solution crystallisation from methanol and dioxane (Figure 9.19c and d). Both laths and triangles could be prepared from dioxane depending on the exact crystallisation conditions (see Figure 9.18a), with triangular crystals forming preferentially under high supersaturation conditions, where precipitation was rapid.

Further insights into the formation of triangular crystals of theophylline were gained by recording videos of the crystal growth from a nitromethane solution using a polarised light microscope. Stills from one of these videos are shown in Figure 9.20. It was evident that several crystals grow from each crystal nucleus, and that they expand outwards from the tip of the triangle in a direction perpendicular to the base of the triangle. They grow in the [001] crystallographic direction, with the long edges of the triangles parallel to the [011] and [0-11] directions. It is worth noting that the hydrogen bonded chains of theophylline molecules in the A and B layers of Form II of theophylline run in the [011] and [0-11] directions respectively. The growth is not uniform across the crystal surface, as can be seen by differences in colour across the crystals in the images, and there appear to be sub-surface inclusions in the crystal on the left of the images (black regions). It is evident that new layers growing from the tip of the triangular crystals have not spread across the crystal surface at an even rate, leading to the formation of macrosteps, which give the appearance of small triangles growing on top of the larger ones. In Figure 9.20c it can be seen that a new nucleation site has formed on the edge of one of the other crystals (marked by an asterisk).

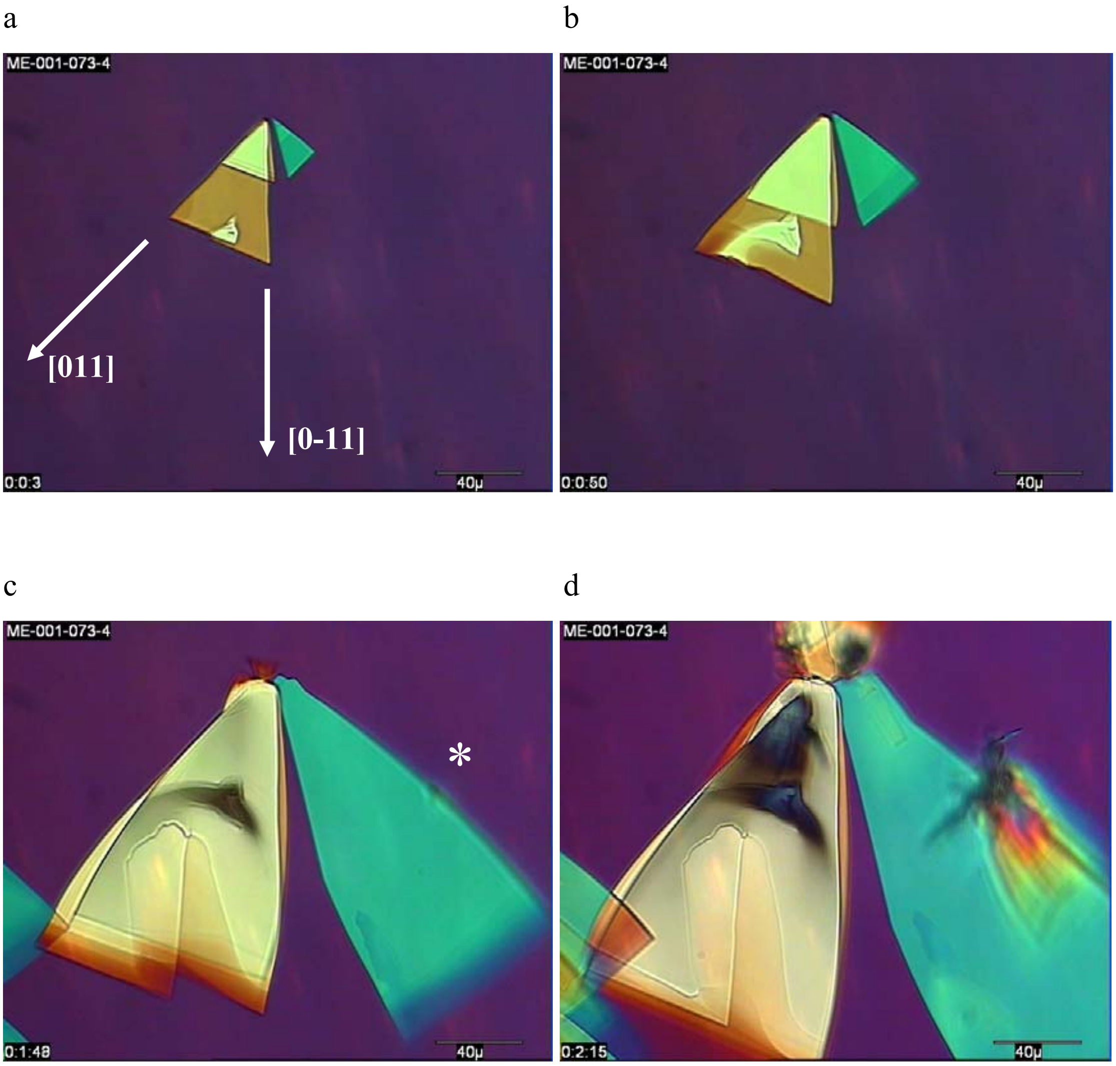

Figure 9.20 Stills recorded from a video of the growth of triangular crystals of Form II of theophylline from nitromethane. The crystallisation occurs over a period of 2 minutes and 15 seconds.

A further observation relating to the formation of triangular crystals of theophylline, made during AFM analysis, was that triangular shaped screw dislocation hillocks were present on the surface of crystals of Form II of theophylline (Figure 9.21a). The triangular shapes of these surface features are aligned with the triangular shape of the crystals (Figure 9.21b). New crystal layers forming at these screw dislocations grow in the [001] direction with edges approximately parallel to [011] and [0-11]. The Burger's vectors of the screw dislocations are in the [100] direction, so they are not the defects that are frequently observed by TEM.

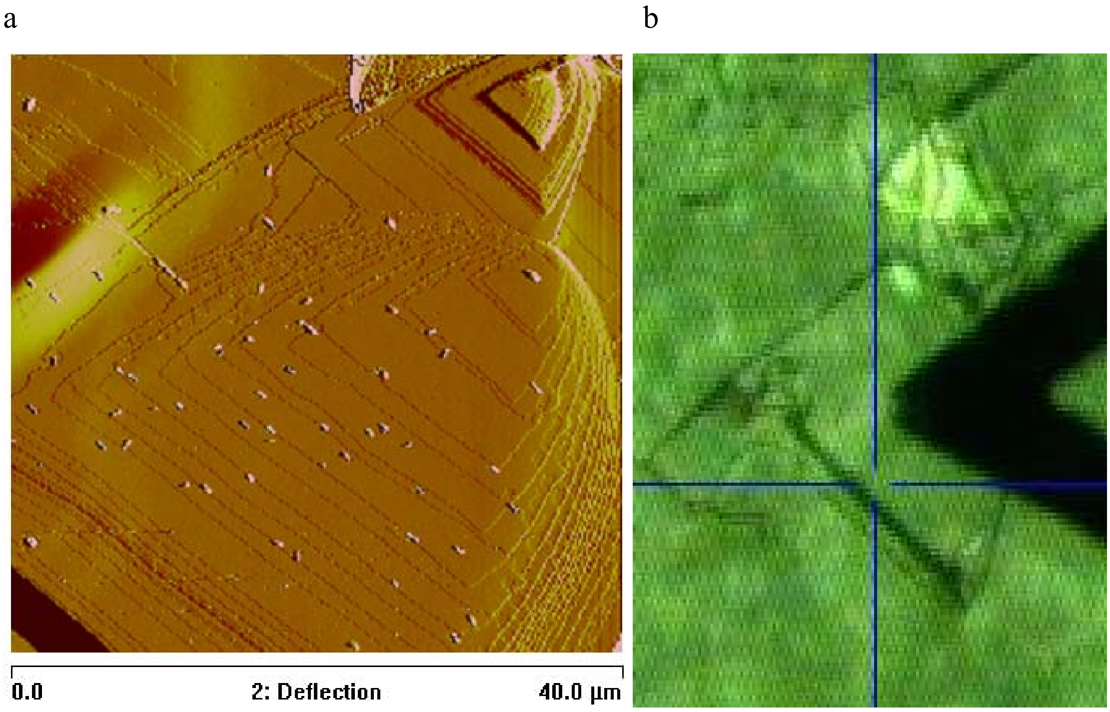

Figure 9.21 (a) AFM deflection image of the surface of a crystal of Form II of theophylline (recorded in contact mode). The image shows a region where two screw dislocations are emergent at the crystal surface. Several crystal planes have grown from the screw dislocations resulting in triangular shaped screw dislocation hillocks. (b) A corresponding optical image showing the whole of the crystal. It is evident that the triangular shaped screw dislocation hillocks are aligned with bulk triangular morphology of the crystal being analysed. These images were recorded with Andrew Cassidy of the Department of Chemistry, University of Cambridge.

The similarity between the shape of the triangular crystals of theophylline and the shape of the screw dislocations with Burger's vectors in [100] is striking. It is postulated that these screw dislocations are present in the nucleii from which triangular crystals of theophylline form, and are actually the reason that the crystals grow with a triangular shape. Rectangular plates and laths of theophylline, such as those obtained by sublimation or crystallisation from methanol, would therefore have grown from nucleii which did not contain these screw dislocations.

9.2.6.6 Comparison of Defects in Crystals of Form II of Theophylline Prepared by Different Methods

The theophylline defects described above were all observed in samples prepared by crystallisation from solution. It is also possible to obtain Form II of theophylline by dehydration of theophylline monohydrate.[13] A sample of Form II of theophylline was prepared in this manner in order to determine if the crystal defects were consistent with those observed in crystals prepared by solution crystallisation.

A sample of theophylline monohydrate was prepared by cooling a saturated solution of theophylline in water. The resulting crystals were needle shaped and up to 5 mm in length (Figure 9.22a). This sample was converted to Form II of theophylline by heating at 90 °C for 24 hours. The crystals retained their external morphology, but their opaque appearance by PLM indicated that they were no longer single crystals (Figure 9.22b). AFM images of the samples are shown in Figure 9.23a and b.

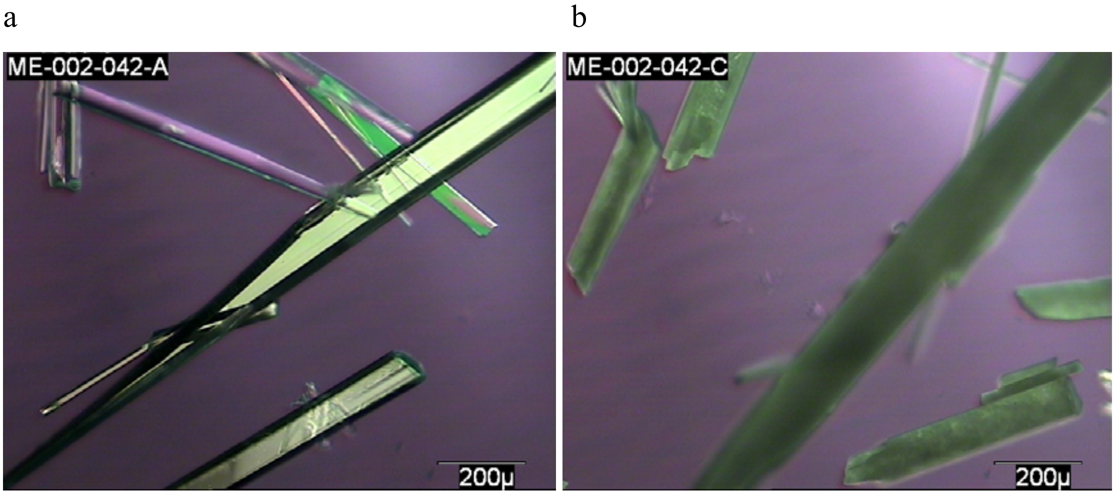

Figure 9.22 PLM images of crystals of theophylline monohydrate before and after dehydration. (a) Crystals of theophylline monohydrate prepared by cooling a saturated aqueous solution. (b) The same sample after heating at 90 °C for 24 hours. Conversion to Form II of theophylline has occurred.

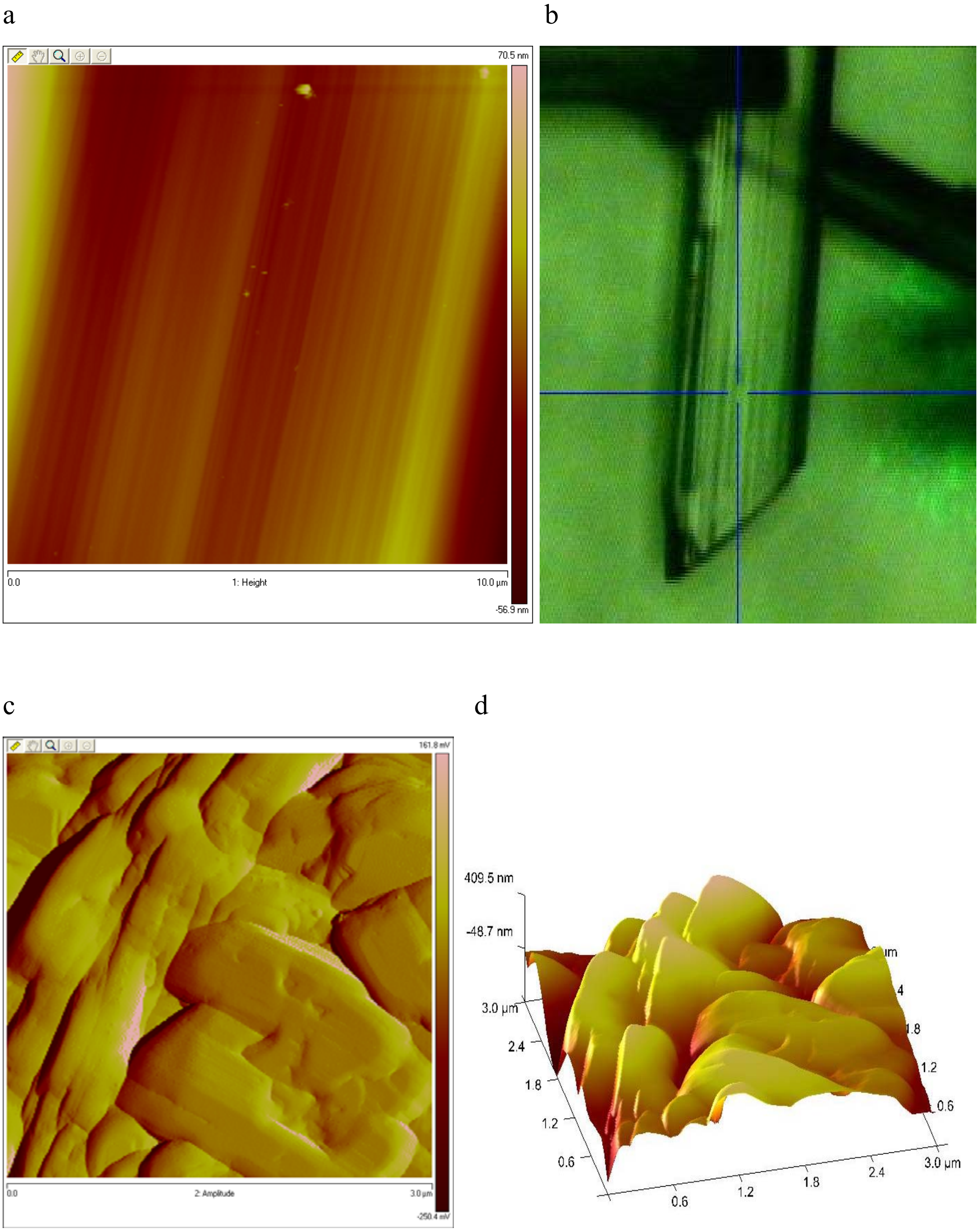

Figure 9.23 AFM images of the surface of crystals of theophylline monohydrate Form I before and after dehydration. (a) AFM height image of the surface of a crystal of theophylline monohydrate showing small ridges running in a direction parallel to the needle axis of the crystal. (b) Corresponding optical image. (c) AFM amplitude image of the surface a crystal from the same sample after heating at 90 °C for 24 hours. There are several small, discrete crystal domains. These domains are separated by defect surfaces. (d) AFM height image of the same area.

The surface of monohydrate crystals was uniform with small ridges running parallel to the long edge. After dehydration to Form II of theophylline, the surface morphology was very different. It was evident that the surface was comprised of many small domains up to 2 μm in length. The domains were tightly intergrown as shown in Figure 9.23c and d, and more closely packed than would be expected for a simple agglomeration of particles. It is therefore believed that there are defect surfaces between the domains. Fewer layers of molecules could be discerned at the crystal surfaces in this sample than with crystals of Form II of theophylline prepared from solution, and there was no evidence of edge dislocations, screw dislocations or stacking faults.

Suzuki et al used SEM to image crystals of theophylline monohydrate before and after dehydration. They noted that the crystals retained their external shape after dehydration, but also stated that the surface of the crystals “consists of agglomerates of smaller particles”.[13] It is apparent that the greater resolution of the AFM images shown here has potentially given a more detailed insight into the nature of the de-solvated material.

The dehydrated sample was also analysed by TEM to try to determine if the domains that were observed by AFM were crystalline, and whether the boundaries between the domains were crystallographically coherent.

The TEM image in Figure 9.24a shows several crystallites of Form II of theophylline. The bend contours in the image appear wide and heavily disrupted indicating a high defect content in the crystals. There are three dark lines in the area marked by the asterisk which are straighter than would be expected for bend contours. These lines could mark crystal domain boundaries. These defects appear to be different to those observed in crystals of Form II of theophylline grown from solution.

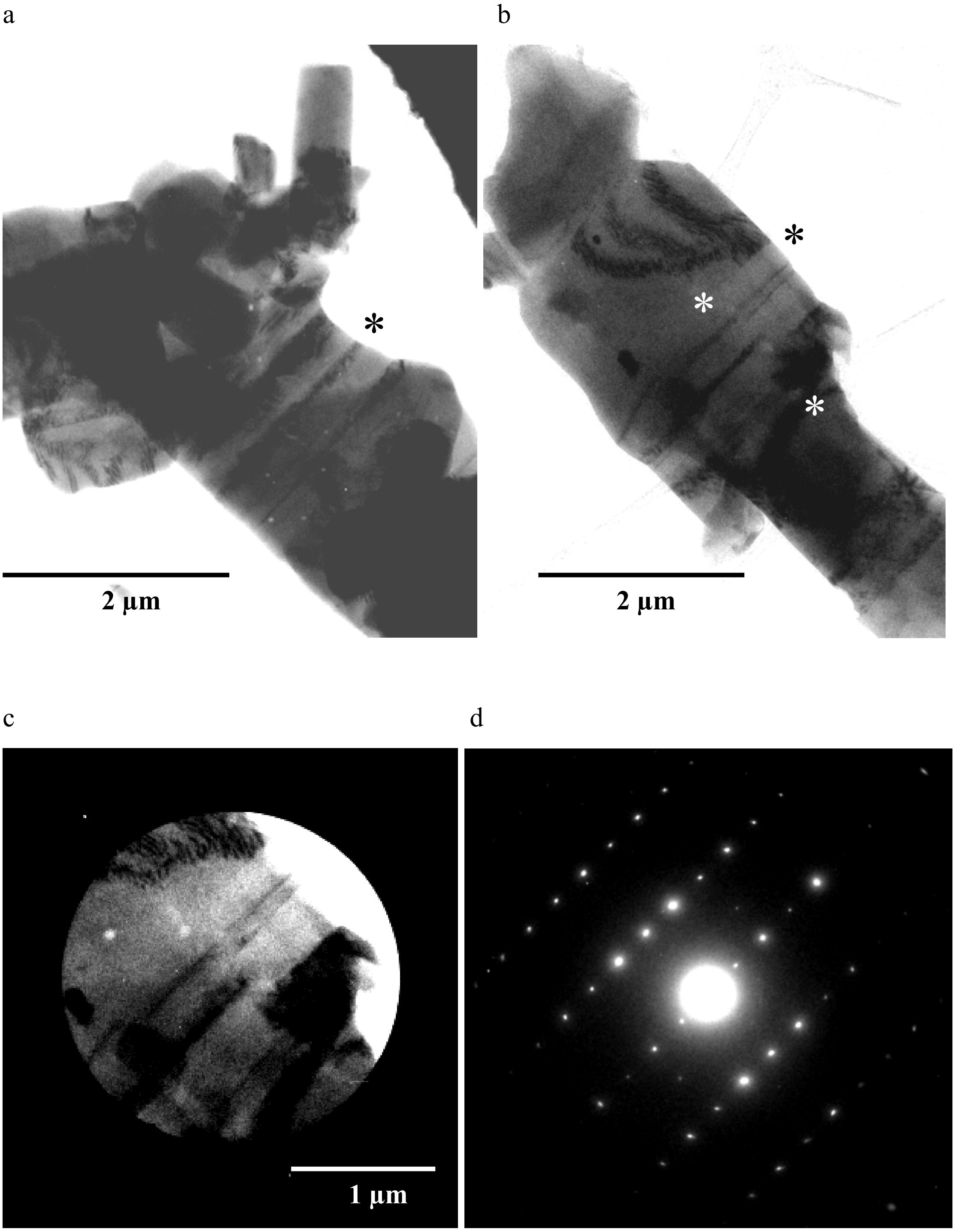

Figure 9.24 TEM images showing evidence of defect planes in Form II of theophylline prepared by dehydrating theophylline monohydrate. (a and b) TEM images of theophylline crystallites. Crystal domain boundaries are highlighted with asterisks. (c) A selected area aperture was used to highlight a small region of the particle in image b. (d) Corresponding electron diffraction pattern of the <110> zone axis of Form II of theophylline.

The asterisks in Figure 9.24b mark out a domain boundary in a different theophylline particle. The presence of the boundary is indicated by the bend contours on the image which abruptly stop when they reach the boundary. The area of sample around this domain boundary, shown in Figure 9.24c, was used to generate an electron diffraction pattern (Figure 9.24d). Even though this area of sample contained two distinct domains only one set of reflections was observed. This result implied that the two domains must be oriented in the same direction. The possibility that one of the domains was amorphous could be discounted as both contained bend contours. It has not yet been determined why there is a domain boundary between these two crystallographically aligned regions of crystal.

A similar result was obtained from the theophylline particle shown in the TEM image in Figure 9.25a. Again, there is a domain boundary between two crystalline regions (highlighted with an asterisk) as evidenced by bend contours ending at this interface.

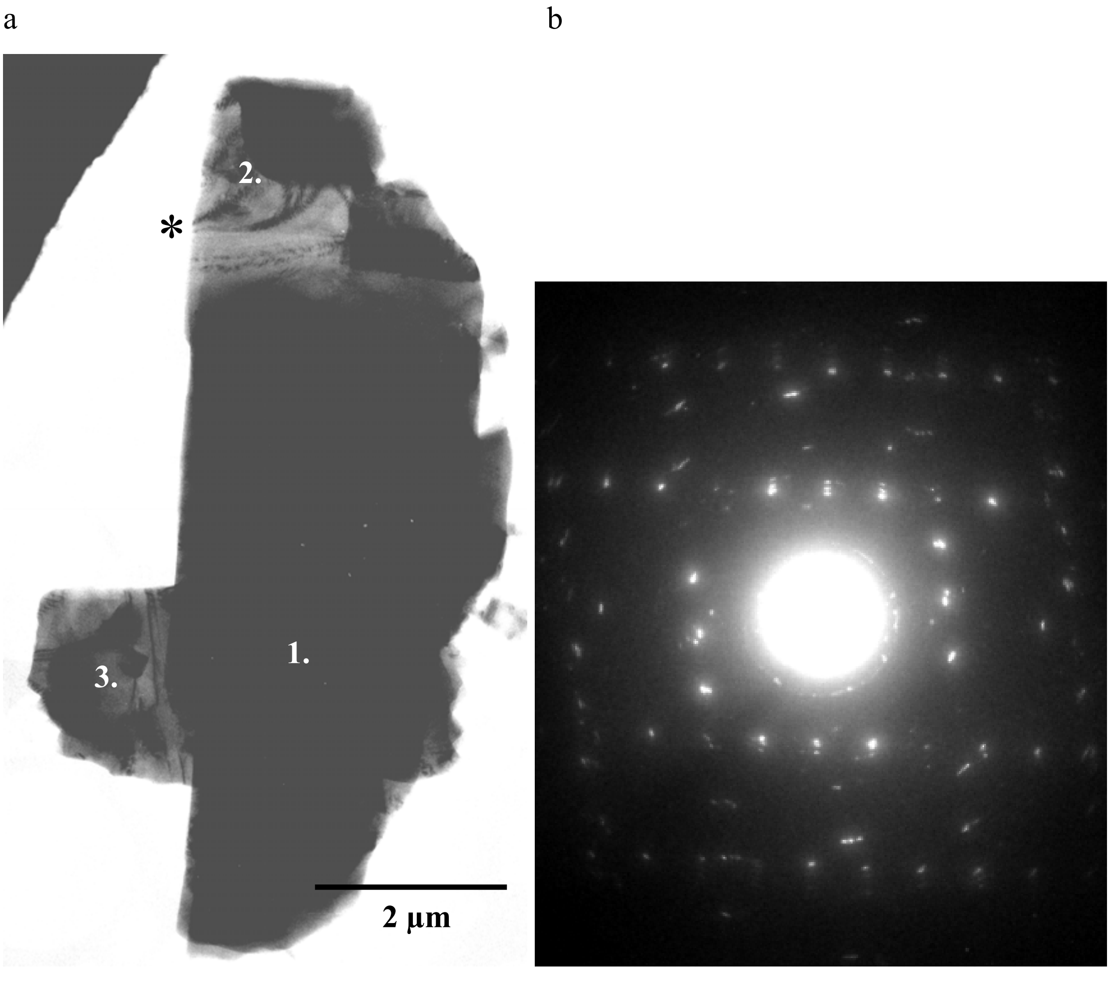

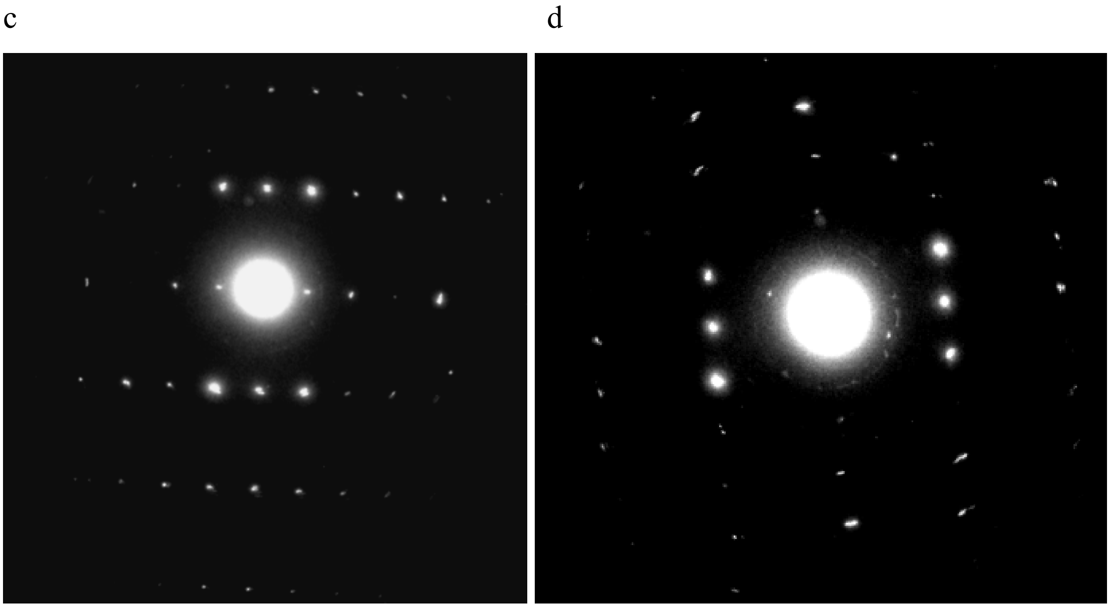

Figure 9.25 TEM images showing evidence of defect planes in Form II of theophylline. (a) TEM image of a theophylline particle. There is a crystal domain boundary to the right of the asterisk. (b) Electron diffraction pattern recorded from the region of crystal marked 1. on the image. This diffraction pattern contains contributions from two different crystalline domains. Both sets of reflections were indexed to the <110> zone axis of Form II of theophylline (c) Electron diffraction pattern recorded from the region of crystal marked 2. on the image. This diffraction pattern was indexed to the <110> zone axis of Form II of theophylline. (d) Electron diffraction pattern recorded from the region of crystal marked 3. on the image. This diffraction pattern was also indexed to the <110> zone axis of Form II of theophylline.

The diffraction patterns in Figure 9.25 indicate that the crystalline regions above and below the domain boundary are aligned. The diffraction pattern from the area marked with a 1 on Figure 9.25a contains two sets of reflections, from two overlapping crystals. One of these sets of reflections matches the diffraction pattern from region 3. The other set of reflections match the pattern from region 2 above the domain boundary.

9.3 Conclusions

Defects were observed in several pharmaceutical crystals using both TEM and AFM.

Characterising defects as edge dislocations, screw dislocations or stacking faults was found to be possible in some cases with TEM, but was not straightforward. Because direct observation of defects with diffraction contrast was not possible, observation of defects was limited to samples that could be crystallised with large, thin regions of sample where bend contours could be obtained. In addition, defects were rarely observed while the TEM analysis was being performed. The low electron beam flux conditions necessary for reducing beam damage limited the possibility of seeing disruptions to bend contours on the viewing screen in the instrument. In most cases, defects were only identified from inspection of the images that resulted from the TEM analysis.

AFM was used to obtain complementary information about defects at the surface of crystals, but it was not necessarily possible to relate these defects to those seen in the bulk by TEM.

Defects were found to cause the fracturing of crystals of Form II of theophylline. Also, screw dislocations in the crystal nucleus may be responsible for the triangular morphology of these crystals. This possible insight into the structure of the crystal nucleus is interesting as the crystal nucleus is too small to characterise by standard analytical methods. The crystallisation method used to prepare crystals of Form II of theophylline was found to influence the types of defects that were present in the crystals.

Defects in molecular crystals are not as well understood as those in ionic or metallic specimens, and a combined TEM and AFM approach to studying molecular defects could aid this understanding.

9.4 Further Work

An important extension to this work would be to use TEM to link crystal defects to changes in crystal form such as polymorphic transitions. An ideal compound for this investigation would crystallise with a thin plate morphology and also undergo a form change between room temperature and -178 °C. The form change could then be monitored *in situ* by TEM using a liquid nitrogen sample holder.

9.5 References

1. Schwarz U. T. Wesite of Dr. Ulrich T. Schwarz, Universität Regensburg. http://www.physik.uni-regensburg.de/forschung/schwarz/.

2. Gliko O., Reviakine I., Vekilov P. G. Stable equidistant step trains during crystallization of insulin. *Phys. Rev. Lett.*, 2003, 90(22), 1-4.

3. Williams D. B., Carter C. B. Transmission electron microscopy. A textbook for materials science. New York: Plenum Press, 1996, p.

4. Reimer L., Kohl H. Transmission Electron Microscopy: Physics of Image Formation, (5th ed.). New York: Springer, 2008, p.

5. Jones W., Thomas J. M. Applications of electron microscopy to organic solid-state chemistry. *Prog. Solid State Chem.*, 1979, 12(2), 101-124.

6. Armigliato A. Analysis of crystal defects by transmission electron microscopy. *Mater. Chem.*, 1979, 4(3), 453-471.

7. Hirsch P., Cockayne D., Spence J., Whelan M. 50 years of TEM of dislocations. Past, present and future. *Philos. Mag.*, 2006, 86(29-31), 4519-4528.

8. Putnis A. Introduction to Mineral Sciences. Cambridge: Cambridge University Press, 1992, p 199-218.

9. McPherson A. Atomic force microscopy applications in macromolecular crystallography. *Acta Crystallogr., Sect. D: Biol. Crystallogr.*, 2001, D57(8), 1053-1060.

10. Dittrich H., Wohlfahrt-Mehrens M. Stacking fault analysis in layered materials. *Int. J. Inorg. Mater.*, 2001, 3(8), 1137-1142.

11. Docherty R., Clydesdale G., Roberts K. J., Bennema P. Application of Bravais-Friedel-Donnay-Harker, attachment energy and Ising models to predicting and understanding the morphology of molecular crystals. *J. Phys. D: Appl. Phys.*, 1991, 24(2), 89-99.

12. Ebisuzaki Y., Boyle P. D., Smith J. A. Methylxanthines. I. Anhydrous theophylline. *Acta Crystallogr., Sect. C: Cryst. Struct. Commun.*, 1997, C53(6), 777-779.

13. Suzuki E., Shimomura K., Sekiguchi K. Thermochemical study of theophylline and its hydrate. *Chem. and Pharm. Bull.*, 1989, 37(2), 493-497.

10 Tubular Crystals of Pharmaceutical Compounds

10.1 Introduction

While attempting to prepare small crystallites of caffeine for analysis by transmission electron microscopy, it was observed that tubular crystals with a hexagonal cross-section were obtained (See Figure 10.1). This is a highly unusual crystal morphology, and so further work was conducted to investigate reproducibility from different solvents, the mechanism of formation and to determine if tubular crystals of other pharmaceutical compounds could be obtained.

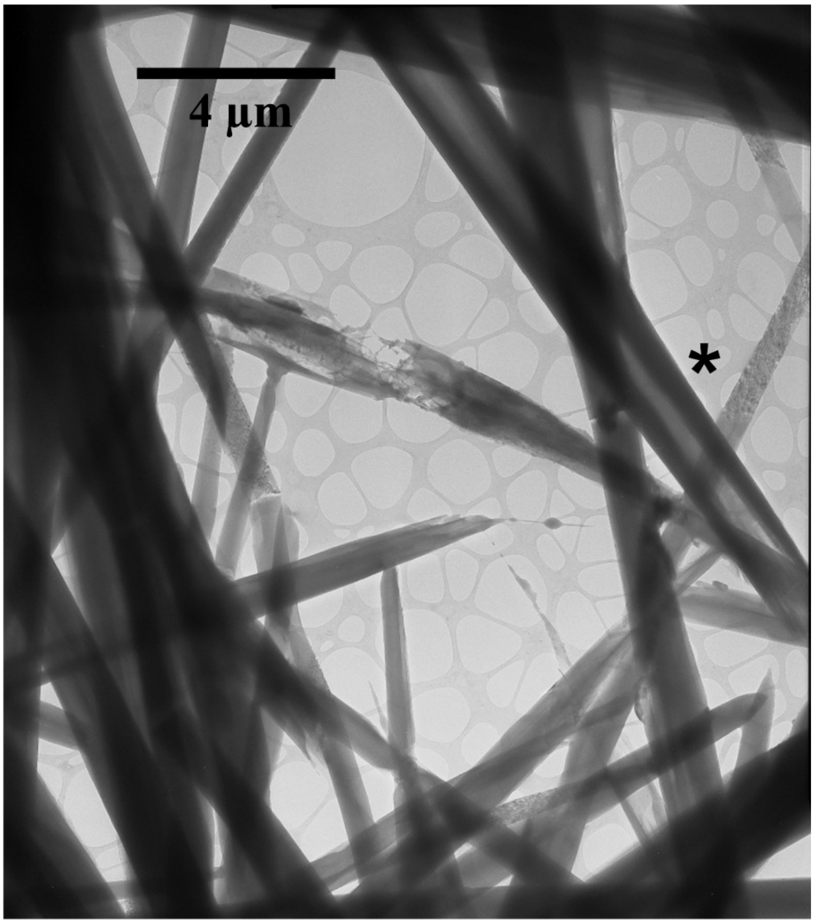

Figure 10.1 Transmission electron microscopy image showing a tubular crystal of caffeine (marked with an asterisk).[1]

Various mechanisms for the growth of tubular crystals have been proposed including rolling up of sheet type crystals,[2-5] templating with rod-shaped crystals of a different compound, or a metastable phase of the same compound,[6-8] preferential dissolution of the centre of rod shaped crystals,[9,10,11] and microwave assisted crystal growth.[12] For each of these mechanisms, it is through the unique chemical properties of the species in question that the formation of the observed tubular structures occurs.[13] As a result, there has been no development of a general strategy for preparing tubular materials, and it has been extremely difficult to predict in advance which compounds will form tubules and under what conditions they might do so.

Previously reported tubular structures can be split into two broad groups. The first group is made up of species which are porous, forming nano-sized tubes through either their molecular conformation, such as chrysotile asbestos,[14] helical oligophenylacetylene,[15] carbon nanotubes,[16] and molybdenum and tungsten disulphides[17,18], through hydrogen bonding networks in solution[19] or through their packing arrangement within a crystal lattice, such as urea,[20] cyclic peptides, carbohydrates and cyclodextrins.[15] Tubule pore diameters for this group of materials tend to be of fixed size, and small, of the order of a few nanometres. The second group of tubular structures are obtained when crystals of an otherwise non-porous material grow with a hollow morphology. Here the tubules can be much larger, with pore diameters of 10 μm having been reported.[21] It is this second type of tubular material that is the focus of this chapter.

Tubular crystals could be of interest to the pharmaceutical industry. The crystal morphology of an API affects properties that are critical to the performance of a pharmaceutical product such as dissolution rate,[22,23] physical stability and hygroscopicity, and will have an impact on many of the processes that are involved in its manufacture such as filtration, drying, handling, storage and compaction.[23-25] The larger surface area and lower density of tubular crystals of an API would be expected to give enhanced properties over solid rods of the same size e.g. increased dissolution rates, smaller aerodynamic diameters (important for drug delivery to the lung)[26,27] and they may also have improved compression properties during tableting. Tubular crystals of a pharmaceutically acceptable compound could also be used as a drug delivery tool if an API could be crystallised within the tubules. A review of the literature has identified only one API that had previously been reported to form tubular crystals, dexamethasone acetate sesquihydrate (1.5 moles of water per mole of dexamethasone acetate).[28]

In a wider context, there has been increasing interest in tubular crystals due to their unique properties. Nano- and microtubes have been shown to have interesting optical[9,29,30] and electronic[15,31-33] properties combined with low densities and high surface areas. These materials have found potential applications in areas such as sensors,[15,12] fluidic transport systems,[34,35] hydrogen storage materials,[36] optical waveguides[9] and drug delivery devices.[37] A major limitation, however, is that only a small percentage of known compounds have been found to form hollow structures, thereby placing a restriction on the range of potential chemical properties of tubular devices.

The pharmaceutical compounds selected for investigating tubular crystal formation were theophylline, as it has a similar molecular structure to caffeine, and carbamazepine, a compound widely used in pharmaceutical research.

10.2 Experimental

The following method used to prepare tubular crystals of caffeine from chloroform is given as an example. Similar procedures were used to obtain tubules of carbamazepine, carbamazepine dihydrate, theophylline monohydrate and aspirin.

A solution of caffeine in chloroform at a concentration of 100 $\mathrm{mg.ml^{-1}}$ was prepared. Approximately 2 µl of this solution was removed and allowed to evaporate at room temperature (on a glass slide or on a sticky carbon SEM sample mount) yielding tubular crystals.

10.3 Results

Evaporative crystallisation studies yielded tubular crystals of caffeine, carbamazepine, carbamazepine dihydrate and theophylline monohydrate. SEM images are shown in Figure 10.2. Tubules of caffeine, crystallised from dichloromethane, have a hollow rod morphology with hexagonal cross-section and pore diameters ranging between 0.2 and 2 μm (Figure 10.2a). XRPD analysis showed these crystals to be to be Form I of caffeine, the metastable trigonal polymorph.[38] Figure 10.2b shows a hollow hexagonal rod of carbamazepine Form II crystallised from toluene. It is evident that there is a significant difference in the pore diameter of the tubule along its length, ranging from 2 to 10 μm. The crystals of carbamazepine dihydrate in Figure 10.2c, prepared from methanol, have a rectangular cross-section and pore diameters ranging between 5 and 25 μm. The small cracks seen in the surfaces of these crystals indicate that some de-solvation is likely to have occurred while the sample was held under vacuum during SEM analysis. Tubular crystals of theophylline monohydrate, crystallised from water, have a poorly defined, rectangular cross-section and pore diameters ranging from 2 to 10 μm (Figure 10.2d).

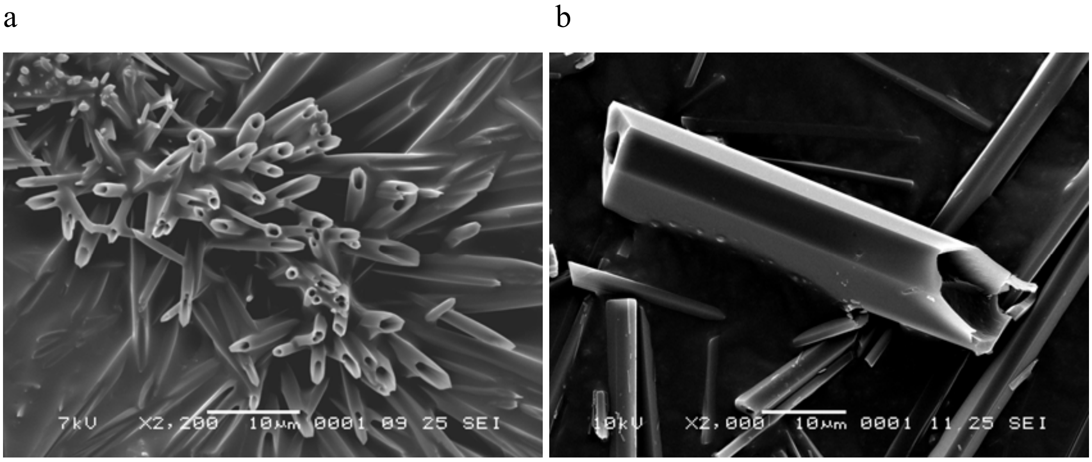

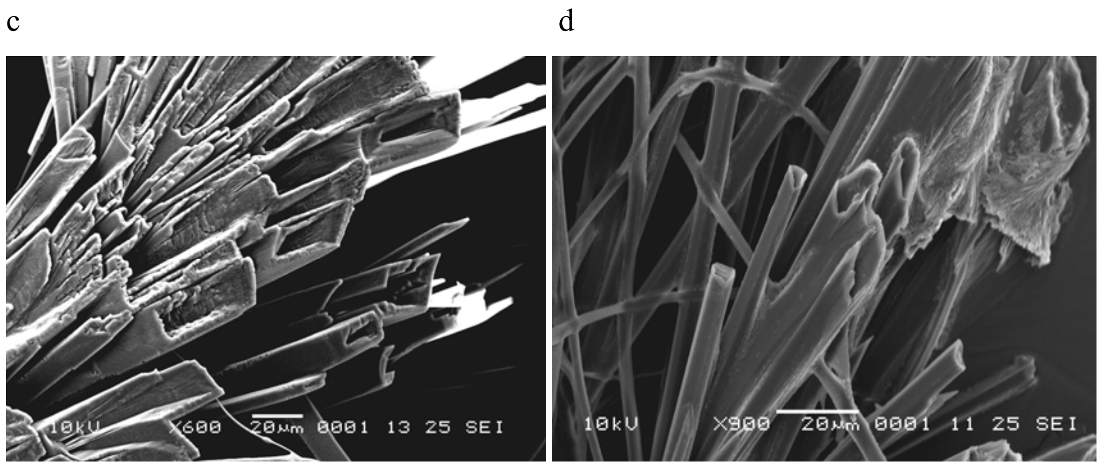

Figure 10.2 Scanning electron microscopy images of tubular crystals of various APIs prepared by solution evaporation at room temperature. (a) Caffeine crystallised from dichloromethane. (b) Carbamazepine crystallised from toluene. (c) Carbamazepine dihydrate crystallised from methanol. (d) Theophylline monohydrate crystallised from water.

In contrast, it was not possible to prepare tubular crystals of (anhydrous) theophylline. Evaporative crystallisations gave solid plate-like crystals of Form II of theophylline as shown in Figure 10.3.

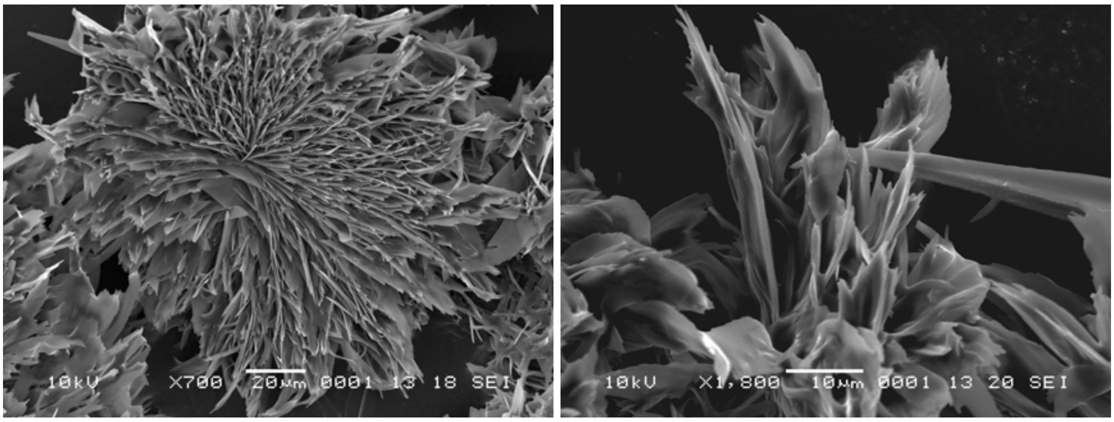

Figure 10.3 Scanning electron microscopy images of theophylline crystallised by evaporation from a 1:1 mixture of DCM and ethanol. Spherullitic growth of plate-like crystals. (a) 700x magnification. (b) 1,800x magnification.

The tubules of caffeine Form I were studied in more detail to investigate reproducibility, the effect of solvent on the crystal morphology and the mechanism of tubule formation. Tubular crystals were obtained reproducibly from chloroform and dichloromethane. The SEM images in Figures 10.4a and 10.4b show crystals of caffeine prepared by evaporation from chloroform viewed side-on and end-on respectively. The crystals are needle-shaped with aspect ratios ranging from 10 to 30 and there is frequent intergrowth of these needles. Such a self-assembled array of interlinked crystals could provide a material of very low density with interesting structural properties. Some crystals display growth defects as is seen for the crystal highlighted with a circle in Figure 10.4a, which has a discontinuity running in the direction of the rod axis. When viewed end-on (Figure 10.4b), it is evident that the needles have a hexagonal cross-section and are hollow, with pore diameters ranging between 0.5 and 5 µm. These crystals are longer and broader than those prepared from dichloromethane (Figure 10.2a), showing that choice of crystallisation solvent has an influence on the morphology of the resulting tubules. On crystallising caffeine from tetrahydrofuran, needle-shaped particles with poorly defined, hexagonal cross-sections and diameters of between 0.2 and 2 µm are obtained. These crystals are highly inter-grown with regions where solid bridges exist between the needles (Figure 10.4c). Crystals of caffeine grown by evaporation from DMSO are not tubular and have a solid needle morphology with signs of uneven growth at the ends of the crystals (Figure 10.4d).

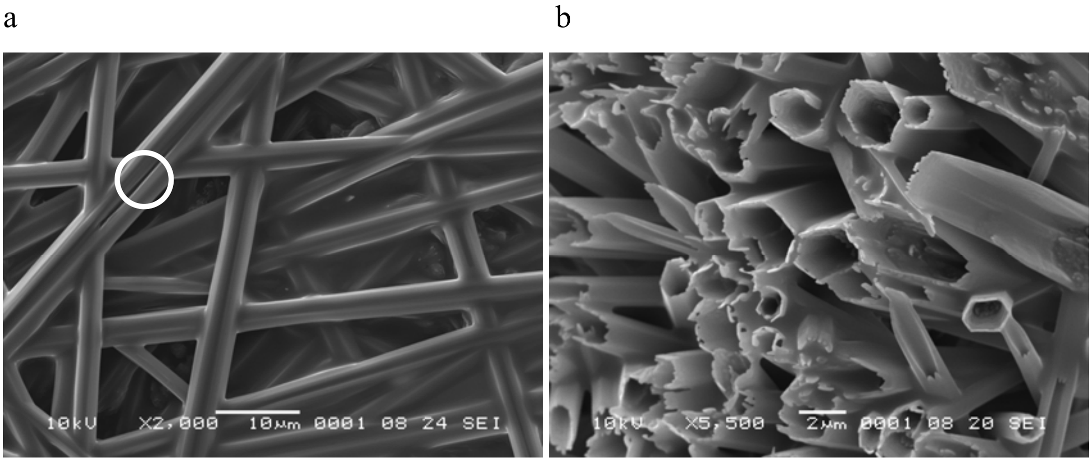

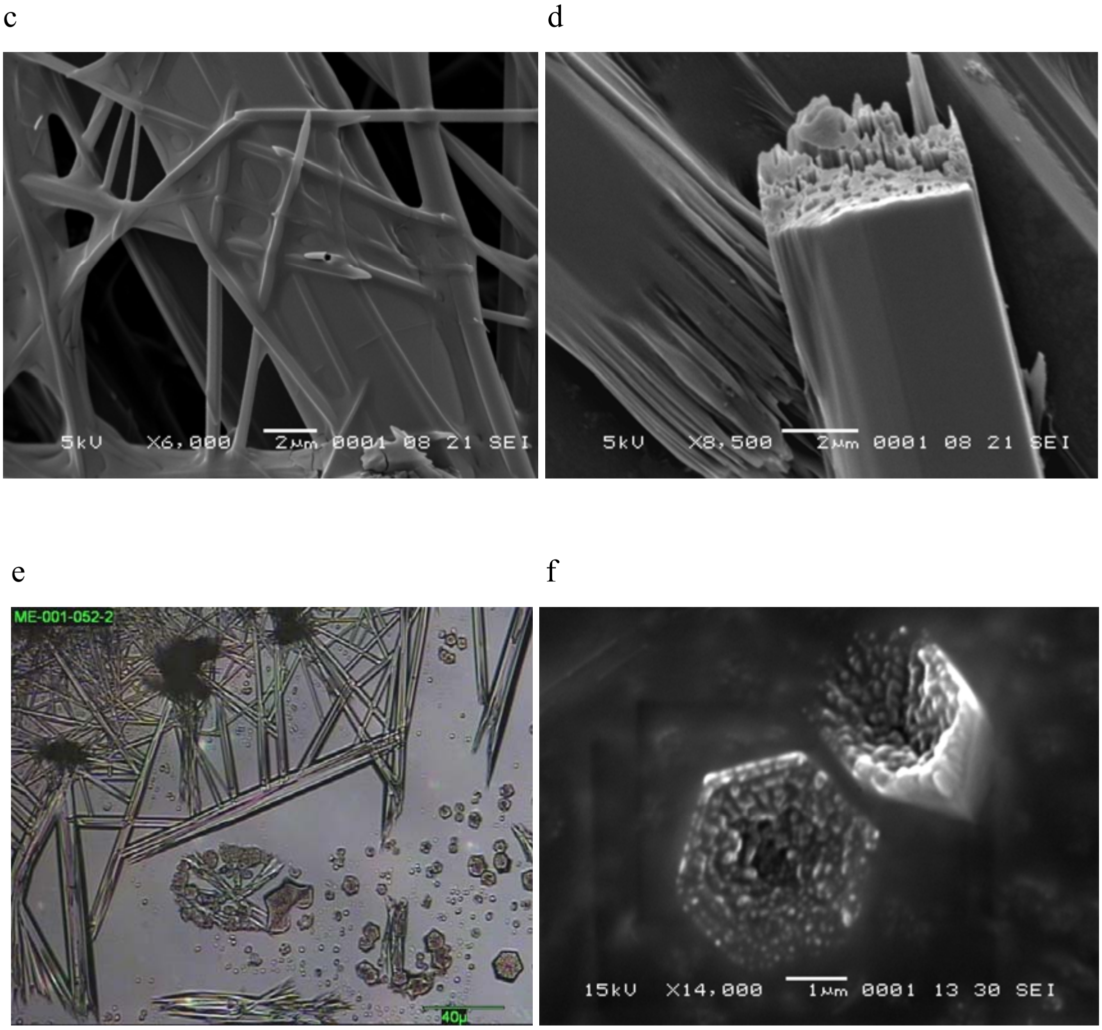

Figure 10.4 Caffeine crystallised by evaporation at room temperature from a range of solvents. (a and b) Scanning electron microscopy images of tubular crystals prepared from chloroform viewed side-on and end-on respectively. The crystal highlighted with a circle in 10.4a has a growth defect running in the direction of the rod axis. (c) Caffeine crystallised from tetrahydrofuran. (d) Rods of caffeine prepared from DMSO. (e) Polarised light microscopy image of tubular rods and hexagonal blocks crystallised from nitromethane. (f) Scanning electron microscopy image of hexagonal blocks crystallised from methanol.

10.4 Discussion

Caffeine, carbamazepine and theophylline are well known, extensively studied compounds, and the evaporative crystallisation conditions utilised here in preparing tubular crystals have been used routinely, so it is surprising that these morphologies have not been reported previously. It is possible that tubular crystals have been prepared, but not recognised due to the difficulty of distinguishing tubules from solid rods. The low resolution and depth of field associated with routine optical microscopy studies makes it extremely difficult to distinguish solid and hollow particles with cross sections of a few microns by this technique. The tubular crystals would not have been identified using this technique alone, as evidenced by the polarised light microscopy image of tubules of caffeine crystallised from nitromethane in Figure 10.4e. In addition, during sample preparation for SEM analysis, it is likely that tubular crystals will lie perpendicular to the intended direction of view, making it hard to observe that they are indeed hollow (Figure 10.4a).

The crystallisation of caffeine Form I was studied further to identify the mechanism by which tubular crystals form. Crystals were found to initially nucleate as hexagonal blocks (as shown in Figures 10.4e and 10.4f) and grow anisotropically, with the growth rate of the top (hexagonal) face several times greater than that of the other surfaces, leading to the formation of hexagonal rods.[39] In the crystal structure of caffeine form I,[40-42] the flat, disordered caffeine molecules associate through π-stacking interactions which propagate in the direction of the c-axis, the growth direction perpendicular to the hexagonal crystal face (Figures 10.5a, 10.5b and 10.5c). Interactions between caffeine molecules in the directions perpendicular to the crystal rod axis are weak, accounting for the slow growth in these directions. This weak interaction may also be the reason that the growth of the hexagonal crystal face becomes uneven, with the face splitting into whiskers. Over time, further crystallisation fills the gaps between these whiskers (Figures 10.4d and 10.5d).

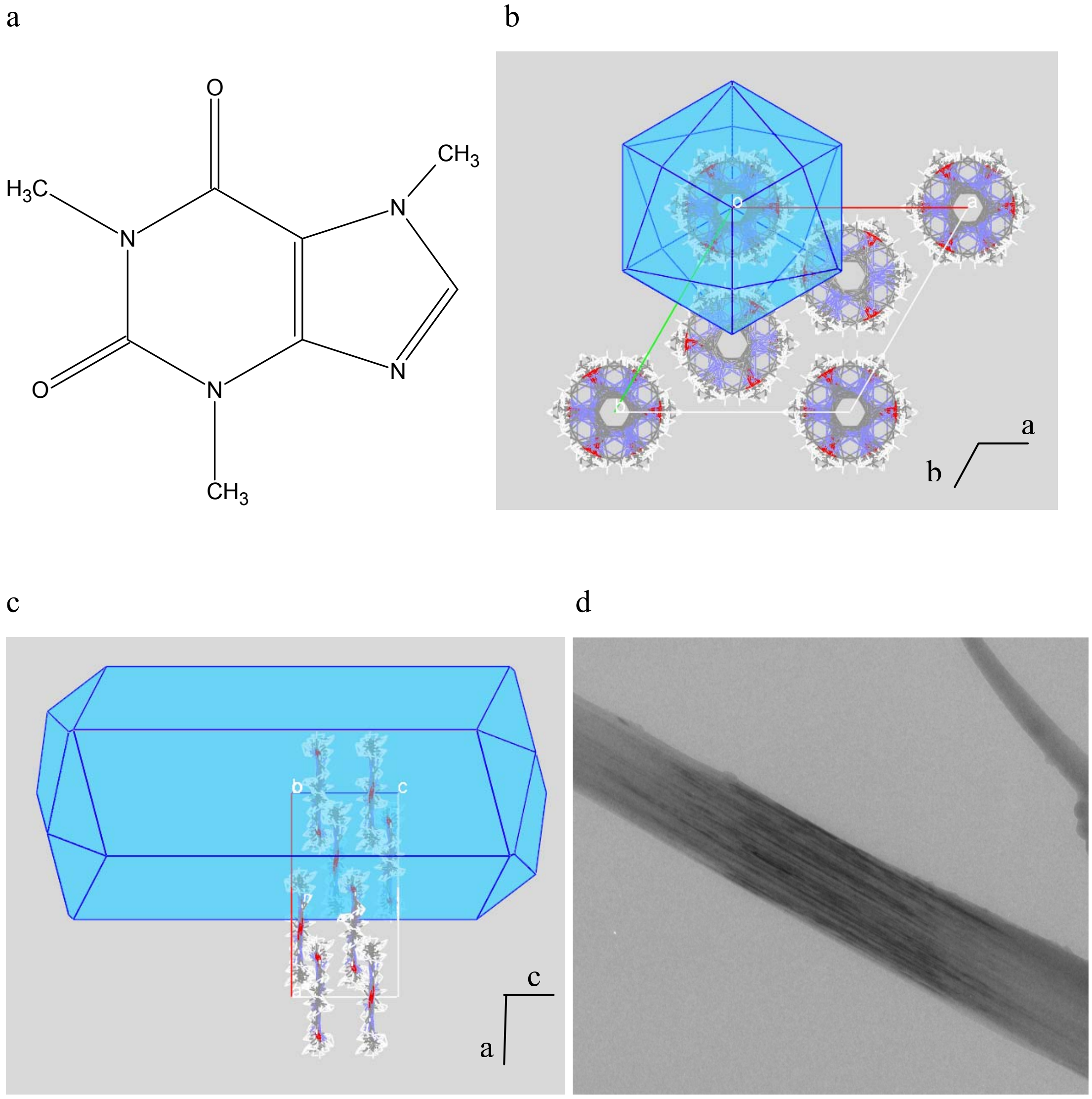

Figure 10.5 (a) The molecular structure of caffeine (flat and disc-like). (b and c) The predicted crystal morphology of caffeine Form I (CSD ref. NIWFEE04),[40] viewed down the c-axis and b-axis respectively. (d) TEM image of a crystal of caffeine. The discontinuous nature of the bend contour (dark region) across the crystal is evidence that it has formed from several smaller whiskers. This image was recorded with Dr. Erica Bithell of the Department of Materials Science and Metallurgy, University of Cambridge.

It is believed that diffusion limited crystallisation conditions, where crystal growth is more rapid than diffusion of molecules to the growing crystal faces, give rise to the formation of the cavity in tubular crystals of caffeine. As it is easier for caffeine molecules to diffuse to the edges of the rapidly growing hexagonal crystal face than it is to diffuse to the centre, a concentration gradient is set up. Crystal growth at the edge of the face is more rapid than at the middle, leading to a doming of the surface which further inhibits diffusion of caffeine molecules to the centre. The concentration of the solution at the centre of the crystal growth face decreases until it is no longer supersaturated and crystal growth stops altogether. The edges of the face continue to grow, forming a cavity within the caffeine crystal.

Diffusion limited crystallisations, and the deviations from perfect, flat crystal faces (loss of polyhedral stability) that result, have been described previously in the literature. Loss of polyhedral stability has been reported for a wide range of compounds[43,44] and for several crystallisation methods including solution growth, crystallisation from the melt, vapour growth, gel growth, and electro-crystallisation,[43,45] but work has focused on crystals with block morphologies where growth is relatively isotropic.[43,46] It has been demonstrated that, under diffusion limited crystallisation conditions, the supersaturation and crystal growth rate influence the amount of disruption that occurs during the growth of crystal faces.[46,47] Below a critical supersaturation level, crystal faces continue to grow uniformly. Any starvation flaws that form in the growing faces have high energy sites and so are preferentially filled by the molecules that are constantly diffusing across the crystal surface.[47,48] Above the critical supersaturation level, crystal growth is more rapid than the rate of diffusion of molecules to the growing crystal faces, and starvation flaws become apparent.[49] On increasing supersaturation and crystal growth rates further, crystal faces become visibly domed inwards. This is shown schematically in Figure 10.6. Increasingly, the crystal grows outwards from its apices. This is termed skeletal (or hopper) crystal growth. At still higher supersaturation levels crystal splitting and dendritic growth occur.[43,48,50]

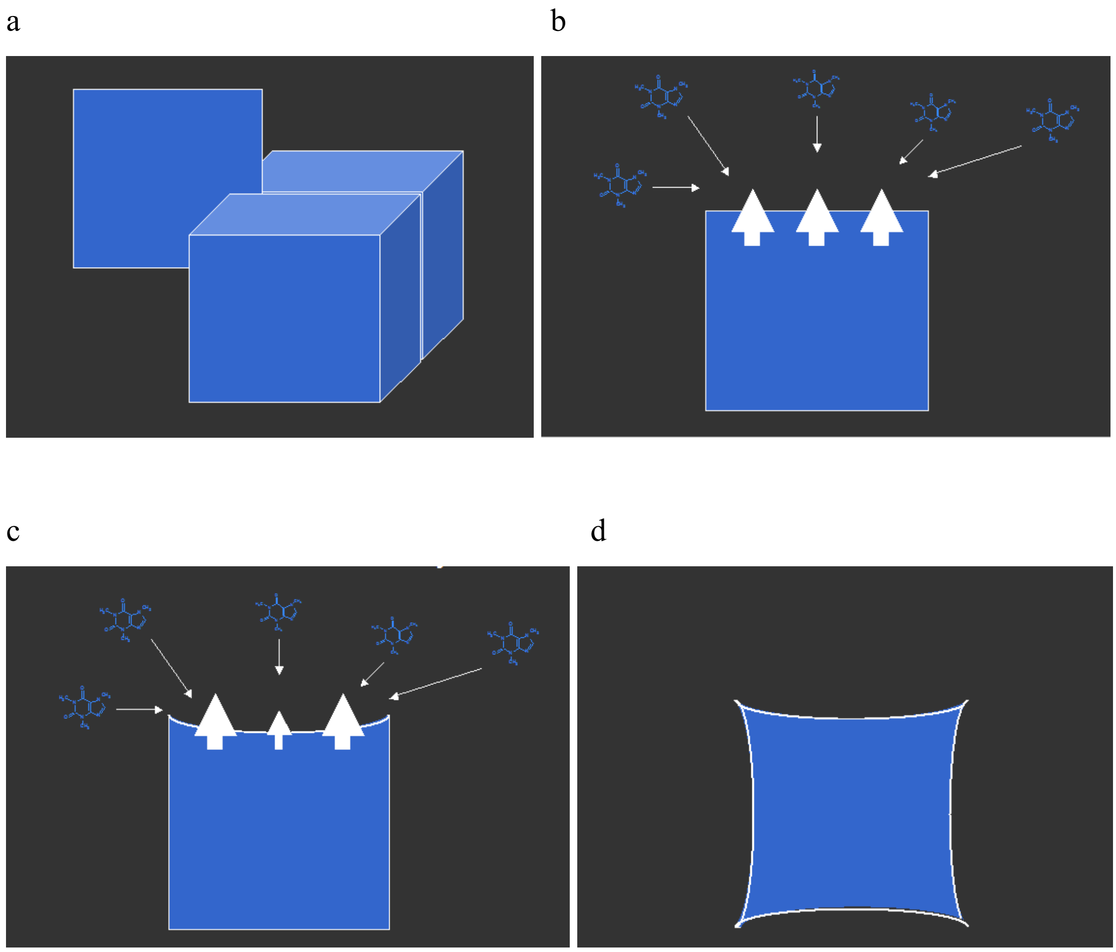

Figure 10.6 Schematic of crystal growth under diffusion limited conditions. (a) The schematic uses a two-dimensional slice from the middle of a crystal. (b) During crystal growth, molecules diffuse to the edges of a crystal face more frequently than to the centre. (c) Under diffusion limited conditions and high supersaturation levels, this will result in doming of a crystal face. (d) Each of the faces of the crystal will become domed inwardly in this manner.

These stages of disruption to growing crystal faces have been observed with caffeine, giving strong evidence that diffusion limited crystallisation is the mechanism by which caffeine tubules are formed. For example, the hexagonal faces of crystals prepared from DMSO (Figure 10.4d) were rough, but there is no indication that the growth rate was greater at the edges than the centre of the face. This suggests that they grew slowly, under low supersaturation conditions, which is likely given the slow evaporation rate of DMSO. With caffeine crystals prepared from methanol, the growth rate of the hexagonal face was greater at the edges than the centre, resulting in the domed appearance (Figure 10.4f). A similar observation, in caffeine crystals grown by sublimation, has been reported by Vaughan.[39] Figure 10.7a is a schematic of skeletal growth from a tubular crystal (high supersaturation conditions).[51] A tubular crystal of caffeine exhibiting this type of skeletal growth is shown in Figure 10.7b.

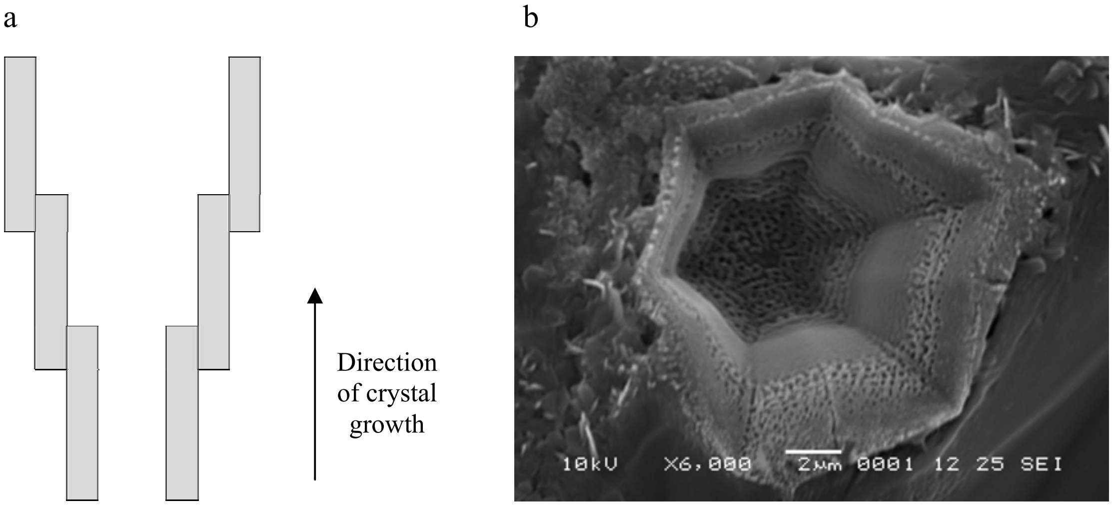

Figure 10.7 Skeletal (or hopper) growth from tubular crystals. (a) Schematic of skeletal crystal growth (reproduced from Iwanaga, 1974)[51]. (b) SEM image of a crystal of caffeine exhibiting skeletal growth. This crystal was prepared by evaporation from chloroform at room temperature.

The influence of supersaturation levels on crystal growth was also observed during crystallisation of caffeine from a drop of DMF solution on a glass slide, monitored by polarised light microscopy (Figure 10.8). The crystal displayed at the bottom middle of Figure 10.8a has nucleated as a hexagonal block. Whiskers start growing from one of the hexagonal faces of the crystal in a direction perpendicular to this face (Figure 10.8b), and cause the crystal to fall onto its side (Figure 10.8c). Crystallisation occurs between the whiskers to give a solid rod. As the drop of solution evaporates, and supersaturation levels increase, crystal growth is limited to the apices of the crystal (Figure 10.8d). Crystal splitting and dendritic growth occur at the end of the crystallisation. The dendrites appear to grow from the vertices of the hexagonal faces, mostly in a direction perpendicular to these faces, but one dendrite grew at 90 ° to the rest (Figures 10.8e and 10.8f).

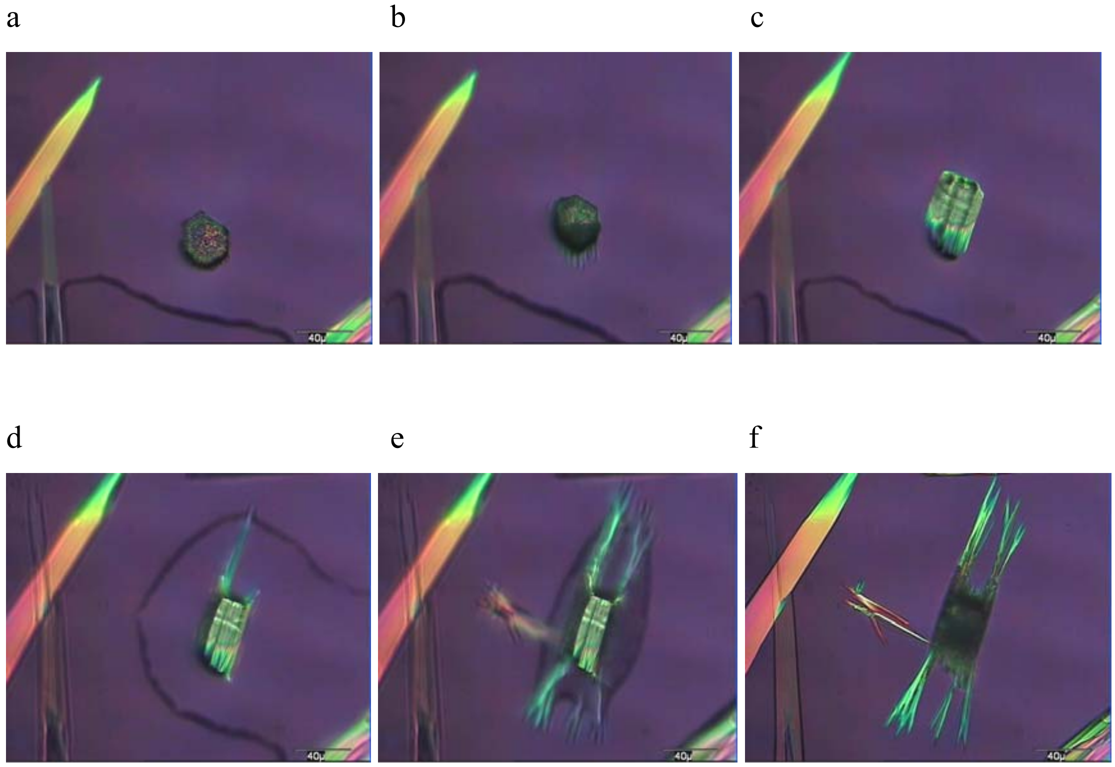

Figure 10.8 Stills taken from a polarised light microscopy video of caffeine crystallising from DMF by evaporation at room temperature. The time lapse between image a and image f is approximately 50 seconds. Note that the crystal fell over between the recording of stills b and c.

While for block shaped crystals growing under diffusion limited conditions there is a slight inward doming of crystal faces,[47] the effect becomes more pronounced at the rapidly growing hexagonal face of caffeine, giving rise to the observed tubular morphology. This combination of diffusion limited crystallisation conditions and highly anisotropic crystal growth appears to be critical in the formation of tubular crystals. This is shown schematically in Figure 10.9.

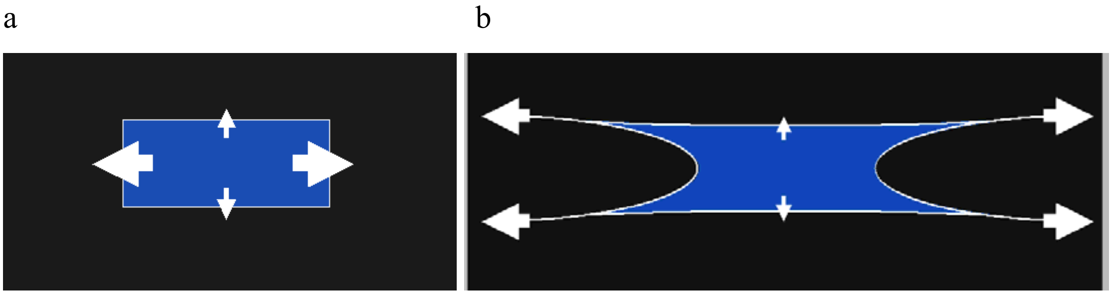

Figure 10.9 Schematic of tubular crystal growth under diffusion limited conditions. (a) Anisotropic crystal growth. Different crystal faces grow at different rates (b) Under diffusion limited conditions there is extensive doming of the most rapidly growing crystal faces, leading to tubular crystal formation.

It is worth noting that this crystallisation mechanism does not rely on any special chemical property of caffeine. Any material would be expected to crystallise with a tubular morphology under conditions where crystal growth at one crystal face is significantly more rapid than at the others (giving rod or needle shaped crystals) and where supersaturation levels and crystal growth rates are high, giving diffusion limited crystallisation (but not high enough to give crystal splitting or dendrite formation). A link between diffusion limited crystallisation and tubular crystal morphologies has been suggested before, for an impurity controlled crystallisation,[52] but is not well established in the literature.

The tubular crystals of carbamazepine Form II, carbamazepine dihydrate and theophylline monohydrate shown in Figure 10.2 were grown under the same evaporative conditions as were used to prepare caffeine tubules, and so crystallisation was also very likely to be diffusion limited in these experiments. These compounds also display anisotropic rod and needle morphologies[53-55] and so it is postulated that the tubules formed by the same mechanism as with caffeine. In contrast, crystals of (anhydrous) theophylline Form II grow with a plate-like morphology, which explains why it was not possible to prepare tubular crystals of this form.

The diffusion-limited tubule crystallisation process postulated for the formation of the tubular crystals of caffeine, carbamazepine, carbamazepine dihydrate and theophylline monohydrate gives another explanation as to why they have not been reported previously. Solutions are usually stirred during crystallisation processes as this promotes crystallite homogeneity. Stirring will reduce or eliminate the concentration gradients across growing crystal faces that were found to be necessary for tubular crystal formation, promoting the formation of solid, non-tubular crystals.

10.5 Application of Diffusion Limited Tubular Crystal Growth to Aspirin

As detailed above, the two key factors in the growth of tubular crystals by the described diffusion-limited mechanism are highly anisotropic crystal growth and high supersaturation levels / crystal growth rates. Both of these factors can be achieved for any given compound through selection of appropriate crystallisation conditions. Highly anisotropic crystal growth can be obtained through choice of crystallisation solvent,[24,56] or addition of small levels of an impurity to inhibit growth of one or more faces.[57,58] Use of other crystallisation methods or variation of the crystallisation temperature can also have an influence on crystal morphology.[59,60] The solvent, crystallisation temperature, evaporation rate and stirring rate (if any) can all be varied to modify the crystallisation kinetics and give high supersaturation levels.

On the basis of these observations, an attempt was made to selectively target conditions suitable for the preparation of tubular crystals of aspirin. Firstly, crystallisation solvents were chosen to give growth of anisotropically shaped (lath, rod or needle) crystals of aspirin. It has been shown that aspirin crystallises as hexagonal plates from very polar solvents such as water (Figure 10.10a) and as needles from more hydrophobic solvents.[61] Ethanol was chosen for initial crystallisation studies. Evaporative crystallisations from this solvent yielded crystals with a lath-shaped morphology (Figure 10.10b). However, there was significant crystal splitting or dendrite formation. This suggested that the crystallisation had occurred under diffusion limited conditions, but that supersaturation levels were too high, and the crystallisation rate too great, for the formation of tubular crystals. It was therefore necessary to alter the kinetics of the crystallisation. Changing the crystallisation solvent to chloroform gave lower supersaturation levels during evaporation, and tubular crystals with rectangular cross sections and pore diameters ranging between 1 and 10 µm were obtained (Figure 10.10c). This result demonstrates for the first time that tubular crystal morphologies can be achieved through a systematic approach rather than just obtained by chance in isolated cases.

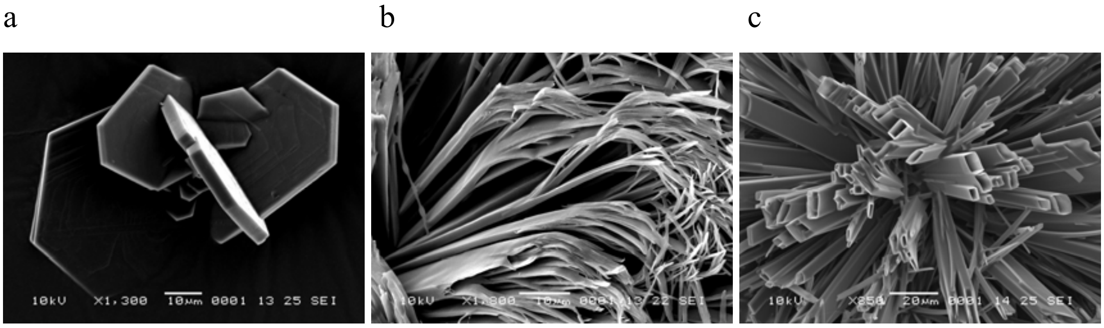

Figure 10.10 SEM images of aspirin crystallised by evaporation at room temperature. (a) Hexagonal plates were obtained by crystallisation from water. (b) The crystals obtained by crystallisation from ethanol had a lath shaped morphology and underwent crystal splitting or dendrite formation. (c) Tubular crystals with a rectangular cross-section were obtained by crystallisation from chloroform.

10.6 Conclusions and Further Work

Tubular crystals of the pharmaceutical compounds caffeine, carbamazepine, carbamazepine dihydrate, theophylline monohydrate and aspirin have been prepared by evaporative crystallisation. The mechanism of tubule formation was elucidated and involves a combination of diffusion limited crystallisation conditions and anisotropic crystal growth. This method of growing tubular crystals is likely to be applicable to a wide range of materials as both of these factors can be achieved for a given compound through selection of appropriate crystallisation conditions, as demonstrated with aspirin.

An investigation into ways of accurately measuring the yield of tubular crystals with respect to solid crystals should be conducted.

10.7 References

1. Eddleston M. D., Bithell E. G., Jones W. Transmission electron microscopy of pharmaceutical materials. *J. Pharm. Sci.*, 2010, 99(9), 4072-4083.

2. Zhao Y. S., Yang W., Xiao D., Sheng X., Yang X., Shuai Z., Luo Y., Yao J. Single Crystalline Submicrotubes from Small Organic Molecules. *Chem. Mater.*, 2005, 17(25), 6430-6435.

3. Chen Y., Zhu B., Zhang F., Han Y., Bo Z. Hierarchical supramolecular self-assembly of nanotubes and layered sheets. *Angew. Chem., Int. Ed.*, 2008, 47(32), 6015-6018, S6015/6011-S6015/6018.

4. Lv H.-M., Chen G.-D., Yan G.-J., Ye H.-G. Synthesis of hexagonal monocrystal AlN microtubes and nanowires at low temperature. *Chin. Phys.*, 2007, 16(9), 2814-2817.

5. Zheng X., Xie Y., Zhu L., Jiang X., Jia Y., Song W., Sun Y. Growth of Sb2E3 (E = S, Se) Polygonal Tubular Crystals via a Novel Solvent-Relief-Self-Seeding Process. *Inorg. Chem.*, 2002, 41(3), 455-461.

6. Liu D., Yates M. Z. Fabrication of Size-Tunable TiO2 Tubes Using Rod-Shaped Calcite Templates. *Langmuir*, 2007, 23(20), 10333-10341.

7. Yu S. H., Coelfen H., Antonietti M. Polymer-Controlled Morphosynthesis and Mineralization of Metal Carbonate Superstructures. *J. Phys. Chem. B*, 2003, 107(30), 7396-7405.

8. Ma Y., Boerner H. G., Hartmann J., Coelfen H. Synthesis of DL-alanine hollow tubes and core-shell mesostructures. *Chem.--Eur. J.*, 2006, 12(30), 7882-7888.

9. Zhao Y. S., Xu J., Peng A., Fu H., Ma Y., Jiang L., Yao J. Optical waveguide based on crystalline organic microtubes and microrods. *Angew. Chem., Int. Ed.*, 2008, 47(38), 7301-7305.

10. Wei A., Sun X. W., Xu C. X., Dong Z. L., Yang Y., Tan S. T., Huang W. Growth mechanism of tubular ZnO formed in aqueous solution. *Nanotechnology*, 2006, 17(6), 1740-1744.

11. Zhang X., Zhang X., Shi W., Meng X., Lee C., Lee S. Single-crystal organic microtubes with a rectangular cross section. *Angew. Chem., Int. Ed.*, 2007, 46(9), 1525-1528.

12. Cheng J., Zhang Y., Guo R. ZnO microtube ultraviolet detectors. *J. Cryst. Growth*, 2008, 310(1), 57-61.

13. Wu Z., Liu Z., Tian P., Yang Y., Xu L., Song H., Bao X., Liu X., Liu X. Syntheses and structures of sodium aluminodiphosphonates with different morphologies (diphosphonate = 1-hydroxyethylidenediphosphonate). *J. Cryst. Growth*, 2004, 264(1-3), 400-408.

14. Bates T. F., Sand L. B., Mink J. F. Tubular crystals of chrysotile asbestos. *Science*, 1950, 111, 512-513.

15. Bong D. T., Clark T. D., Granja J. R., Ghadiri M. R. Self-assembling organic nanotubes. *Angew. Chem., Int. Ed.*, 2001, 40(6), 988-1011.

16. Iijima S. Helical microtubules of graphitic carbon. *Nature*, 1991, 354(6348), 56-58.

17. Tenne R., Margulis L., Genut M., Hodes G. Polyhedral and cylindrical structures of tungsten disulfide. *Nature*, 1992, 360(6403), 444-446.

18. Rao C. N. R., Govindaraj A., Gundiah G., Vivekchand S. R. C. Synthetic methods and strategies for synthesis of carbon nanotubes, nanowires, and nanorods. *Chem. Eng. Sci.*, 2004, 59(22-23), 4665-4671.

19. Pantos G. D., Pengo P., Sanders J. K. M. Hydrogen-bonded helical organic nanotubes. *Angew. Chem., Int. Ed.*, 2007, 46(1+2), 194-197.

20. Harris K. D. M. Meldola lecture: understanding the properties of urea and thiourea inclusion compounds. *Chem. Soc. Rev.*, 1997, 26(4), 279-290.

21. Medina D. D., Mastai Y. Synthesis of DL-Alanine Mesocrystals with a Hollow Morphology. *Cryst. Growth Des.*, 2008, 8(10), 3646-3651.

22. Blagden N., de Matas M., Gavan P. T., York P. Crystal engineering of active pharmaceutical ingredients to improve solubility and dissolution rates. *Adv. Drug Delivery Rev.*, 2007, 59(7), 617-630.

23. Tiwary A. K. Modification of crystal habit and its role in dosage form performance. *Drug Dev. Ind. Pharm.*, 2001, 27(7), 699-709.

24. Lee A. Y., Myerson A. S. Particle engineering: fundamentals of particle formation and crystal growth. *MRS Bull.*, 2006, 31(11), 881-886.

25. Rasenack N., Muller B. W. Crystal habit and tableting behavior. *Int. J. Pharm.*, 2002, 244(1-2), 45-57.

26. Gonda I. The ascent of pulmonary drug delivery. *J. Pharm. Sci.*, 2000, 89(7), 940-945.

27. Chow A. H. L., Tong H. H. Y., Chattopadhyay P., Shekunov B. Y. Particle Engineering for Pulmonary Drug Delivery. *Pharm. Res.*, 2007, 24(3), 411-437.

28. Mallet F., Petit S., Lafont S., Billot P., Lemarchand D., Coquerel G. Crystal Growth Mechanism in a Solution of Hollow Whiskers of Molecular Compounds. *Cryst. Growth Des.*, 2004, 4(5), 965-969.

29. Zhou L., Wang W., Zhang L., Xu H., Zhu W. Single-crystalline BiVO4 microtubes with square cross-sections: microstructure, growth mechanism, and photocatalytic property. *J. Phys. Chem. C*, 2007, 111(37), 13659-13664.

30. Geng J., Zhu J.-J., Lu D.-J., Chen H.-Y. Hollow PbWO4 Nanospindles via a Facile Sonochemical Route. *Inorg. Chem.*, 2006, 45(20), 8403-8407.

31. Sgobba V., Guldi D. M. Carbon nanotubes-electronic/electrochemical properties and application for nanoelectronics and photonics. *Chem. Soc. Rev.*, 2008, 38(1), 165-184.

32. Hu J., Bando Y., Zhan J., Xu F., Sekiguchi T., Golberg D. Growth of single-crystalline cubic GaN nanotubes with rectangular cross-sections. *Adv. Mater.*, 2004, 16(16), 1465-1468.

33. Rao A. M., Richter E., Bandow S., Chase B., Eklund P. C., Williams K. A., Fang S., Subbaswamy K. R., Menon M., Thess A., Smalley R. E., Dresselhaus G., Dresselhaus M. S. Diameter-selective Raman scattering from vibrational modes in carbon nanotubes. *Science*, 1997, 275(5297), 187-191.

34. Marti-Rujas J., Desmedt A., Harris K. D. M., Guillaume F. Kinetics of Molecular Transport in a Nanoporous Crystal Studied by Confocal Raman Microspectrometry: Single-File Diffusion in a Densely Filled Tunnel. *J. Phys. Chem. B*, 2007, 111(43), 12339-12344.

35. Lee S. B., Martin C. R. Electromodulated Molecular Transport in Gold-Nanotube Membranes. *J. Am. Chem. Soc.*, 2002, 124(40), 11850-11851.

36. Liu C., Fan Y. Y., Liu M., Cong H. T., Cheng H. M., Dresselhaus M. S. Hydrogen storage in single-walled carbon nanotubes at room temperature. *Science*, 1999, 286(5442), 1127-1129.

37. Liu Z., Chen K., Davis C., Sherlock S., Cao Q., Chen X., Dai H. Drug Delivery with Carbon Nanotubes for In vivo Cancer Treatment. *Cancer Res.*, 2008, 68(16), 6652-6660.

38. Cesaro A., Starec G. Thermodynamic properties of caffeine crystal forms. *J. Phys. Chem.*, 1980, 84(11), 1345-1346.

39. Vaughan N. P. The generation of monodisperse fibers of caffeine. *J. Aerosol Sci.*, 1990, 21(3), 453-462.

40. Enright G. D., Terskikh V. V., Brouwer D. H., Ripmeester J. A. The Structure of Two Anhydrous Polymorphs of Caffeine from Single-Crystal Diffraction and Ultrahigh-Field Solid-State 13C NMR Spectroscopy. *Cryst. Growth Des.*, 2007, 7(8), 1406-1410.

41. Descamps M., Correia N. T., Derollez P., Danede F., Capet F. Plastic and Glassy Crystal States of Caffeine. *J. Phys. Chem. B*, 2005, 109(33), 16092-16098.

42. Derollez P., Correia N. T., Danede F., Capet F., Affouard F., Lefebvre J., Descamps M. Ab initio structure determination of the high-temperature phase of anhydrous caffeine by X-ray powder diffraction. *Acta Crystallogr., Sect. B: Struct. Sci.*, 2005, B61(3), 329-334.

43. Nanev C. N. Instability of faceted crystal shapes and their transformation into skeletons during growth under diffusion control. *Crystallogr. Rev.*, 1994, 4(1), 3-71.

44. Nanev C. N., Penkova A. N. Polyhedral (in-)stability of protein crystals. *J. Cryst. Growth*, 2002, 237-239(Pt. 1), 283-288.

45. Nanev C. N. Critical size of crystals growing under diffusion conditions for loss of polyhedral stability. *J. Cryst. Growth*, 1994, 140(3-4), 381-387.

46. Wilcox W. R. Morphological stability of a cube growing from solution without convection. *J. Cryst. Growth*, 1977, 38(1), 73-81.

47. Nanev C. N. Polyhedral (in-)stability by increasing supersaturation - maximum rate of stable growth. *J. Cryst. Growth*, 2000, 212(3/4), 516-521.

48. Mason B. J., Bryant G. W., Van den Heuvel A. P. The growth habits and surface structure of ice crystals. *Philos. Mag.*, 1963, 8, 505-526.

49. Nanev C. N., Rashkov R. S. Polyhedral instability and transition to skeletal growth during electrocrystallization of cadmium. *J. Cryst. Growth*, 1996, 158(1/2), 136-143.

50. Vivares D., Kaler E. W., Lenhoff A. M. Polyhedral Instability of Glucose Isomerase Crystals as Revealed by Confocal Scanning Fluorescence Microscopy. *Cryst. Growth Des.*, 2007, 7(8), 1411-1415.

51. Iwanaga H., Shibata N. Grown mechanism of hollow zinc oxide crystals from zinc selenide. *J. Cryst. Growth*, 1974, 24-25, 357-361.

52. Kumar K. Growth of zinc oxide hollow crystals from flux methods. *J. Cryst. Growth*, 1974, 26(2), 200-202.

53. Rustichelli C., Gamberini G., Ferioli V., Gamberini M. C., Ficarra R., Tommasini S. Solid-state study of polymorphic drugs: carbamazepine. *J. Pharm. Biomed. Anal.*, 2000, 23(1), 41-54.

54. Tian F., Sandler N., Aaltonen J., Lang C., Saville D. J., Gordon K. C., Strachan C. J., Rantanen J., Rades T. Influence of polymorphic form, morphology, and excipient interactions on the dissolution of carbamazepine compacts. *J. Pharm. Sci.*, 2007, 96(3), 584-594.

55. Sun C., Zhou D., Grant D. J. W., Young V. G., Jr. Theophylline monohydrate. *Acta Crystallogr., Sect. E: Struct. Rep. Online*, 2002, E58(4), o368-o370.

56. Lee T., Kuo C. S., Chen Y. H. Solubility, polymorphism, crystallinity, and crystal habit of acetaminophen and ibuprofen: by initial solvent screening. *Pharm. Technol.*, 2006, 30(10), 72-92.

57. Berkovitch-Yellin Z., Addadi L., Idelson M., Lahav M., Leiserowitz L. Controlled modification of crystal habit via "tailor-made" impurities: application to benzamide. *Angew. Chem., Int. Ed.*, 1982, 21(S8), 1336-1345.

58. Veintemillas-Verdaguer S. Chemical aspects of the effect of impurities in crystal growth. *Prog. Cryst. Growth Charact. Mater.*, 1996, 32(1-3), 75-109.

59. van Hoof P. J. C. M., Grimbergen R. F. P., Meekes H., van Enckevort W. J. P., Bennema P. Morphology of orthorhombic n-paraffin crystals: a comparison between theory and experiments. *J. Cryst. Growth*, 1998, 191(4), 861-872.

60. Shaw D., Mason B. J. The growth of ice crystals from the vapor. *Philos. Mag.*, 1955, 46, 249-262.

61. Watanabe A., Yamaoka Y., Takada K. Crystal habits and dissolution behavior of aspirin. *Chem. Pharm. Bull.*, 1982, 30(8), 2958-2963.

11 Concluding Remarks

This section contains a summary of the findings that were described in the experimental chapters of the thesis.

11.1 Preparation and Polymorphism of Pharmaceutical Cocrystals

While much of the focus of research into pharmaceutical cocrystals has been directed towards determining the types of cocrystals that can be isolated, developing suitable methods of screening for cocrystals and investigating the enhancement in solid-state properties that can be achieved by cocrystallisation, the work in this thesis has concentrated on the equally important, but less studied, areas of cocrystal polymorphism and development of methods that can be used to prepare cocrystals on an industrial scale.

Freeze-drying was used to prepare a variety of different cocrystal forms. Crystallisation at the interface between two immiscible solvent layers was used to generate caffeine:1-hydroxy-2-naphthoic acid and phenazine:mesaconic acid cocrystals, and an RS-ibuprofen:4,4-bipyridyl cocrystal was prepared by mixing salts of the two cocrystal formers. All three of these cocrystallisation methods are suitable for use on a large scale.

New polymorphic forms of both the caffeine:1-hydroxy-2-naphthoic acid cocrystal and the phenazine:mesaconic acid cocrystal were obtained from cocrystallisation at the interface between solvent layers, and freeze-drying yielded a novel solid-solution of caffeine and theophylline, showing the potential of these techniques as cocrystal polymorph screening tools. In all, 11 polymorphic cocrystal systems were identified during this study, and a key finding was that several cocrystallisation methods (solution crystallisation, liquid assisted grinding, thermal methods, crystallisation between solvent layers and freeze-drying) were required in order to isolate all of these forms. This result suggests that when screening for polymorphs of cocrystals as many different crystallisation methods as possible should be employed. While polymorph screening with single component systems is usually focussed around solution crystallisations, similar approaches will not be suitable for cocrystals as the range of solvents that can be used in solution crystallisations is limited to those in which the two crystal formers have similar solubilities.

11.2 Application of Transmission Electron Microscopy to the Characterisation of Pharmaceutical Materials

TEM is a technique which is widely used for the analysis of inorganic samples. Its use for the characterisation of pharmaceutical samples prior to this study has, however, been very limited, largely due to the difficulties associated with the preparation of appropriately thin samples, and issues with sample damage caused by the electron beam. Strategies for overcoming these issues have been described in this thesis which have enabled characterisation a variety of pharmaceutical compounds, including theophylline, paracetamol and aspirin, and also pharmaceutical salts and cocrystals. A range of relevant materials information about these compounds was derived including morphology, polymorph identification, mapping of crystal habit to crystal structure and characterisation of pharmaceutical nanomaterials, demonstrating that various issues associated with pharmaceutical form development might usefully be addressed using TEM, with advantages over more commonly used analytical methods. For example, crystals of 'impurity' polymorphic phases were identified in samples of theophylline that appeared to be monophasic by XRPD. Polymorph identification with TEM requires just a single micro-crystal, and in favourable cases can be successful on the nanometre scale making it a significantly more sensitive technique than XRPD, and potentially advantageous in the pharmaceutically important areas of solid-form screening and patent infringement.

TEM analysis also revealed the existence of small crystallites of a new polymorph of theophylline in a sample dominated by Form II, conditions under which it could not have been identified using conventional analytical techniques. Solving the crystal structure of this new form of theophylline required the development of an entirely new approach to crystal structure determination. A set of possible crystal structures for theophylline was generated by crystal structure prediction, and electron diffraction patterns from one of the crystallites of the new polymorph were used to establish which (if any) of these structures was consistent with the new form. There was a clear match between the electron diffraction patterns and an orthorhombic Pbca structure that had the third lowest calculated lattice energy of the set generated by crystal structure prediction.

The combined TEM/CSP method could prove to be an important tool for crystal structure determination in the pharmaceutical industry, and also in many other areas of chemistry. The enhanced ability to observe and identify new polymorphic forms of pharmaceuticals, as afforded by this approach, could reduce the risk that unexpected solid-state behaviour will occur in future pharmaceutical products.

11.3 Analysis of Defects in Pharmaceutical Crystals

For the first time, TEM has been used to observe and characterise defects in crystals of pharmaceutical compounds. In addition, defects emergent at crystal surfaces were analysed by AFM, enabling edge dislocations, screw dislocations and stacking faults to be identified. With samples of Form II of theophylline, the crystal preparation method was found to have an influence on the types of defects that were present. One specific type of defect, an edge dislocation with a Burger's vector in the [010] direction, was commonly observed in theophylline samples and was linked to fracturing of crystals. The identification of defects in these crystals of theophylline could not have been achieved with any other analytical technique currently used for pharmaceutical analysis.

The ability to observe and characterize crystal defects, as afforded by TEM and AFM, could significantly improve the understanding and control of the solid-state behaviour of pharmaceutical compounds.

11.4 Preparation of Tubular Crystals

Tubular crystals of the pharmaceutical compounds aspirin, caffeine, carbamazepine, carbamazepine dihydrate and theophylline monohydrate were prepared by evaporative crystallisation. These novel, rod-shaped, hollow crystals have hexagonal or rectangular cross-sections, and pore diameters ranging from 0.1 to 25 μm. The crystallisations are believed to occur under conditions where crystal growth was more rapid than diffusion of molecules to the most rapidly growing face of the crystal, leading to formation of a central cavity within the crystals. The two key factors in this mechanism of tubule formation are highly anisotropic crystal growth, where the growth rate of one of the crystal faces is several times greater than that of the others, and high supersaturation levels, giving high crystallisation rates and diffusion limited growth. Through selection of appropriate crystallisation conditions, both of these factors can be achieved for a given compound, and so this mechanism of tubular crystal formation is likely to be applicable to a wide range of chemical species. For example, conditions suitable for the growth of tubular crystals of aspirin were identified systematically through selection of solvent and control of crystallisation rate. This is the first time that a systematic approach for the preparation of tubular crystals has been developed, and is therefore a significant advance in the field.

Though it is not certain that tubular pharmaceutical crystals will have any practical importance, the more general observation that diffusion limited crystallisation conditions lead to uneven and domed crystal faces is relevant to the pharmaceutical industry as surface related properties such as surface energy, hygroscopicity, particle adhesion and flowability could be affected.